# Centro de Investigación Científica y de Educación Superior de Ensenada, Baja California



---

## Programa de Posgrado en Ciencias de la Tierra con orientación en Geofísica Aplicada

---

# Interpretation of marine electromagnetic data of the Wagner Basin

Tesis

para cubrir parcialmente los requisitos necesarios para obtener el grado de Maestro en Ciencias

Presenta:


**Valeria Reyes Ortega**


Ensenada, Baja California, México

2016

Tesis defendida por

**Valeria Reyes Ortega**

y aprobada por el siguiente Comité

Dr. Enrique Gómez Treviño
Codirector de tesis

Dr. Steven Constable
Codirector de tesis

Dr. Carlos Francisco Flores Luna

Dr. José Gómez Valdés

**Dr. Juan García Abdeslem**
Coordinador del Posgrado en Ciencias de la Tierra

**Dra. Rufina Hernández Martínez**
Directora de Estudios de Posgrado

Resumen de la tesis que presenta **Valeria Reyes Ortega** como requisito parcial para la obtención del grado de Maestro en Ciencias en Ciencias de la Tierra con orientación en Geofísica Aplicada.

**Interpretación de datos electromagnéticos marinos de la Cuenca Wagner**

Resumen aprobado por:

| | |
|---|---|
| Dr. Enrique Gómez Treviño<br>Codirector de tesis | Dr. Steven Constable<br>Codirector de tesis |

Durante Mayo de 2015 se llevó a cabo un proyecto de colaboración entre el Centro de Investigación Científica y de Educación Superior de Ensenada (CICESE) y Scripps Institution of Oceanography, University of California, San Diego (SIO / UCSD), para estudiar el potencial geotérmico del Norte del Golfo de California utilizando métodos electromagnéticos marinos sobre las cuencas Wagner y Consag. La presente tesis comprende la adquisición, procesamiento, modelado directo e inversión de datos obtenidos a bordo del "Buque Oceanográfico Alpha Helix", utilizando la reciente desarrollada versión del método electromagnético de fuente controlada (CSEM), que puede ser remolcada sobre la superficie marina para medir las amplitudes de campos electromagnéticos mientras el buque mapea la zona de interés. Este método permite mapear los contrastes de resistividad eléctrica del fondo del mar proporcionando información única dado que la resistividad eléctrica es un indicador de la porosidad y tipo de roca, así como también de la temperatura. Los datos fueron registrados a lo largo de transectos cubriendo una longitud aproximada de 600 km, que comprende una superficie de alrededor de 7.400 kilómetros cuadrados. El sistema consistió en 4 receptores conformados de un dipolo eléctrico que registraron la señal transmitida de cuatro frecuencias 0.5, 1.5, 3.5 y 6.5 Hz, existiendo múltiples separaciones entre el transmisor y los receptores de 250, 500, 750 y 1000 m. Un total de aproximadamente 16,200 mediciones individuales fueron analizadas para obtener imágenes de la distribución de la resistividad a lo largo de los diferentes transectos. Se invirtieron el conjunto de datos teniendo en cuenta modelos isotrópicos y anisotrópicos, con el fin de mejorar el ajuste entre los datos y la respuesta del modelo. Los resultados muestran una correlación positiva entre la baja resistividad eléctrica y los altos valores de flujo de calor, que ya han sido relacionados con zonas hidrotermales; e incluso los resultados expanden las áreas en donde pudiera haber altos valores de flujo de calor. Además, el método ayudó a identificar posibles zonas de flujo de salida hidrotermal que coinciden con la presencia de fallas identificadas anteriormente por estudios de reflexión sísmica.

**Palabras clave: Energía geotérmica, resistividad eléctrica, CSEM, Inversión**

Abstract of the thesis presented **by Valeria Reyes Ortega** as a partial requirement to obtain the Master of Science degree in Earth's Sciences with orientation in Applied Geophysics.

**Interpretation of marine electromagnetic data of the Wagner Basin**

Abstract approved by:

| | |
|---|---|
| Dr. Enrique Gómez Treviño<br>Thesis codirector | Dr. Steven Constable<br>Thesis codirector |

A collaborative project between the Centro de Investigación Científica y de Educación Superior de Ensenada (CICESE) and Scripps Institution of Oceanography, University of California San Diego (SIO/UCSD), to better understand the geothermic potential of the Northern Gulf of California, was carried out applying marine geophysical electromagnetic methods over the Wagner and Consag basins. The present thesis comprises the acquisition, processing, forward and inverse modelling of the data collected on board the Alpha Helix Cruise during May of 2015, using the recently developed surface towing version of the Controlled Source Electromagnetic Method (CSEM), which measures the amplitudes of electromagnetic fields while the ship maps the area of interest. This method allows to map the electrical resistivity contrasts of the seabed providing unique information given that the electrical resistivity is proxy for porosity and rock type, and also for temperature. Data were recorded along several lines with a total length of 600 km, comprising an area of about 7400 square km. The apparatus consisted of 4 receivers made with one electric dipole which recorded the transmitted signal of four frequencies of 0.5, 1.5, 3.5 and 6.5 Hz, and multiple separations between transmitter and receivers of 250, 500, 750 and 1000 m. A total of 16200 individual measurements were analyzed to obtain images of the resistivity distribution along the different lines. We inverted data sets considering isotropic and anisotropic models, in order to improve the misfit between the data and the model response. The results show positive correlation between low resistivity and high heat flow values which have been already related to hydrothermal zones; the results even expand the areas where there may be high heat flow values. Furthermore, the method helped to identify areas where there is possible outflow that match the presence of faults identified by previous seismic reflection surveys.

**Keywords: Geothermal energy, electrical resistivity, CSEM, Inversion modeling**

# Dedication

*To my mother, who's courage against the difficulties will always motivate me to overcome my fears and doubts. To my father, who's passion for life inspired me to follow my dreams with love and happiness.*

# Agradecimientos

Al ir desarrollando el proyecto de tesis, el apoyo de amigos, familiares, compañeros y de gente nueva que fue llegando a mi vida se volvió algo indispensable para que este trabajo fuera culminado con una sonrisa en mi rostro.

Primeramente quiero agradecer a mis directores de tesis Dr. Enrique Gómez Treviño y Dr. Steven Constable. En particular al Dr. Enrique Gómez Treviño, doy gracias por su apoyo, positivismo y excelentes enseñanzas tanto profesionales como personales que me dieron el valor para iniciar y terminar este proyecto. Gracias infinitas al Dr. Steven Constable por su paciencia, gran apoyo para aprender una metodología nueva, así como el apoyo económico que me brindó durante mi estancia en SIO/UCSD, además le estaré siempre agradecida por motivarme a continuar con mi preparación profesional durante estos próximos años en UCSD.

A mi padre, Dr. Sergio Reyes Coca, quien desde pequeña siempre ha sido mi más grande inspiración para lograr mis sueños, cumplir todo lo que me propongo y vivir la vida al máximo a cada momento, gracias por siempre darme una nueva lección que aprender, Te Amo.

A mi madre, Hortencia Ortega Gutiérrez, a quien doy gracias a Dios por permitir tenerte a mi lado cada día, gracias a tu fortaleza me has enseñado que siempre se pueden vencer las adversidades, y que siempre se puede disfrutar de la vida como si el tiempo nunca pasara, Te Amo.

A mis hermanos, porque aunque somos tan diferentes, esas diferencias han logrado que seamos muy unidos y que nos divirtamos siempre en grande al estar juntos. Doy gracias también que me han permitido ser tía de los niños más maravillosos que hay.

Al Dr. Antonio González, muchísimas gracias por permitirme ser partícipe en el proyecto desde el principio y darme las facilidades en desarrollar el trabajo de tesis con los datos colectados a bordo del Buque Oceanográfico Alpha Helix, sin su apoyo este proyecto nunca hubiera sido posible de realizar.

Al equipo de trabajo del Marine EM Lab que me recibió con los brazos abiertos y ayudó de una manera increíble para aprender al máximo durante la estancia que realicé en SIO/UCSD, gracias Dr. Kerry Key, Jacques Lemire, John Souders, Jake Perez y Chris Armerding. Muchísimas gracias Peter Kannberg y Dallas Sherman, porque gracias a su ayuda aprendí tantos detalles del método que me llevaron a obtener exitosamente resultados.

A los miembros de comité, Dr. José Gómez Valdés y Dr. Carlos Francisco Flores Luna por su colaboración, apoyo, correcciones, y enseñanzas brindadas durante la realización de este proyecto.

Al Dr. Antonio González, Dr. Guillermo Díaz Méndez, Doris Piñero Lajas por proporcionarme los datos de batimetría que fueron indispensables para la obtención de resultados, muchísimas gracias.

Al Dr. Martín Barajas, Dr. Mario González y M.Cs. Martín Pacheco, por brindarme su ayuda para entender mejor la zona de estudio y correlacionar los datos con perfiles sísmicos adquiridos en la zona.

Al Dr. José Manuel Romo Jones por sus recomendaciones y por tomarse un minuto de su tiempo para ayudarme a resolver dudas.

A UC Mexus - CICESE por el apoyo económico para realizar la estancia en UCSD, asi como al personal administrativo que me orientó en todo momento, gracias a Veronica Jasmin Sandoval y Dora A. Baltazar.

A Iris Mccrary, por la gran ayuda brindada durante las estancias realizadas.

Al personal administrativo que hacen un valioso trabajo y facilitan en gran manera el trabajo de investigación en CICESE, en especial muchas gracias a Bárbara Uribe, Célica Cuevas y Ana Rosa Soto.

A mi mejor amiga y hermana de toda la vida, Lizette Flores Romero, gracias por siempre estar a mi lado, ya sabes que te amo y gracias por todas las aventuras y locuras que hemos compartido juntas en estos años de amistad.

A todos mis amigos, Jennefer García, Iván Ritchie, Jorge López, Rubi De los Santos, Marysol Escobar, Assha Alonso, Darinka Rudametkin, Karen Hamilton, Paola Jáuregui, Karina López, Lily Ledesma, Fernando Bello, Rafa Ramirez y Octavio López, gracias por todo lo que hemos compartido juntos, ya saben que los quiero con todo mi corazón y que siempre estaré ahí para ustedes.

A Cristal Zuñiga, Maria Proettoy Shaday Michan porque al conocerlas mi estancia en San Diego se volvió única y aprendí muchísimo de ustedes, gracias por todo amigas.

A Thalia Aviles con quien compartí tantas vivencias en San Diego, juntas afrontamos un nuevo reto y aprendimos tanto de una de la otra durante esos meses, muchas gracias por todo, te quiero.

A todos mis compañeros y a las personas que he conocido en CICESE, en especial a Gerardo Vallejo, Valdemar Belmonte, Hugo Villaverde, Leandro Pérez, Yessica Contreras, Leidy Leyva, Jonathan Carrillo, Gabriel Mejía, Javier Avendaño, Mayra Cuellas y Ruben Rioyos, muchas gracias por todo.

A Rebeca Perez De Alva Blanco y Nurkia Rudametkin, que hayan llegado a mi vida ha sido una gran bendición, muchísimas gracias.

Al capitán y tripulación del Buque Oceanográfico Alpha Helix.

Al Centro de Investigación Científica y de Educación Superior de Ensenada (CICESE).

Al Consejo Nacional de Ciencia y Tecnología (CONACYT), por el apoyo económico a lo largo de estos dos años.

Al Centro Mexicano de Innovacion en Energia Geotermica (CeMIE-Geo).

Son innumerables las personas y situaciones a las cuales agradezco por permitirme vivir esta grandiosa experiencia, a todos ustedes, con quienes me encontré en algún momento de nuestras vidas gracias, porque siempre lo hacemos posible.

Finalmente quiero agradecer a Dios y a mis angelitos por llegar a mi vida para quedarse, brindándome su amor cuando más lo he necesitado.

## Acknowledgements

As I developed the thesis project, the support of friends, family, colleagues and new people who were coming into my life became indispensable so I could complete this work with a smile on my face.

First I want to thank my thesis directors Dr. Enrique Gómez Treviño and Dr. Steven Constable. In particular Dr. Enrique Gómez Treviño, thank you for your support, positivism and excellent professional and personal teachings that gave me the courage to start and finish this project. Infinite thanks to Dr. Steven Constable for his patience, great support to learn a new methodology, as well as for the economic support given during the internships at SIO / UCSD, moreover I will always be grateful for motivating me to continue my professional preparation over the next few years at UCSD.

To my father, Dr. Sergio Reyes Coca, who since my childhood has always been my greatest inspiration to achieve my dreams, fulfill all my purposes and taught me to live life to the fullest every moment, thank you for always giving me a new lesson to learn, I love you.

To my mother, Hortencia Ortega Gutiérrez, whom I thank God every day for allowing us to have you by our side, your strength taught me we can always overcome adversity, and we can always enjoy life as if the time never goes by, I love you.

To my brothers, because even though we are so different, these differences have made us become closer and we always enjoy the time we spend together. Also thank you all, for allowing me to be the aunt of the most wonderful children.

To Dr. Antonio González, thank you so much for letting me be involved in the project from the beginning and for giving me the facilities to develop the thesis with data collected on board the “Buque Oceanográfico Alpha Helix”, without your support this project would’ve never been possible to perform.

To the team of the Marine EM Lab who welcomed me with open arms and helped incredibly to learn the most during my stay at SIO / UCSD, thanks Dr. Kerry Key, Jacques Lemire, John Souders, Jake Perez and Chris Armerding. Thank you so much Peter Kannberg and Dallas Sherman, because thanks to your help I learned many details of the method that led me to successfully achieve results.

To my Committee members, Dr. Jose Gómez Valdés and Dr. Carlos Francisco Flores Luna for their cooperation, support, corrections, and teachings provided during the realization of this project.

To Dr. Antonio González, Dr. Guillermo Díaz Méndez, Doris Piñero Lajas for providing me the bathymetry data which were essential to achieve results, thank you very much.

To Dr. Martín Barajas, Dr. Mario González and M.Cs. Martin Pacheco, for your help to better understand the study area and correlate the data with seismic profiles acquired in the area.

To Dr. José Manuel Romo Jones for your recommendations and for taking a minute of your time to help me answer some questions.

To UC Mexus - CICESE for the financial support during my stay at UCSD, as well as the administrative staff who guided me at all time, thanks to Veronica Jasmin Sandoval and Dora A. Baltazar.

To Iris Mccrary, for the great help given during my stay at SIO/UCSD.

To the administrative staff who do a valuable work and greatly facilitate the research work in CICESE, especially thank you very much Barbara Uribe, Célica Cuevas and Ana Rosa Soto.

To my best friend and sister of life, Lizette Flores Romero, thanks for always being by my side, you know that I love you and thank you for all the adventures we have shared together in these years of friendship.

To all my friends, Jennefer Garcia, Ivan Ritchie, Jorge Lopez, Rubi De los Santos, Marysol Escobar, Assha Alonso, Darinka Rudametkin, Karen Hamilton, Paola Jauregui, Karina López, Lily Ledesma, Fernando Bello, Rafael Ramirez and Octavio López, thanks for all that we shared together, you know that I love with all my heart and I'll always be there for you.

To Crystal Zúñiga, Maria Proetto and Shaday Michan because after meeting you my stay in San Diego became unique and I learned a lot from you, thanks for everything.

To Thalia Aviles with whom I shared many experiences in San Diego, together we faced a new challenge and learned so much from one another during those months, thank you very much for everything.

To all my colleagues and people I've met in CICESE, especially Gerardo Vallejo, Valdemar Belmonte, Hugo Villaverde, Leandro Pérez, Yessica Contreras, Leidy Leyva, Jonathan Carrillo, Gabriel Mejia, Javier Avendaño and Ruben Rioyos, thank you so much for everything.

To Rebeca Perez and Nurkia Rudametkin, it’s been a great blessing that you both came into my life, thank you for everything.

To the captain and crew from the “Buque Oceanográfico Alpha Helix”

To the Centro de Investigación Científica y de Educación Superior de Ensenada (CICESE).

To the Consejo Nacional de Ciencia y Tecnología (CONACYT), for the financial support throughout these two years.

To the Centro Mexicano de Innovación en Energía Geotérmica (CeMIE-Geo).

I thank countless people and situations that allowed me to live this great experience, all of you, with whom I met at some point in our lives thank you, because we always make it happen.

Finally I want to thank God and my angels for coming into my life, and for giving me your love when I needed it the most.

# Table of contents

# List of figures

# List of tables

# Chapter 1. Introduction

Over the last few decades interest in exploiting geothermal energy has been under the scope since thermal energy generated and stored in the Earth is considered a clean renewable resource. Suitable areas for its exploitation are found over the world, and despite that at present days its use is restricted to land, heat generation lies along the limit between plate tectonics or hot stops. The geothermal potential zones worldwide are shown in Figure 1.

## 1.1 Geothermal energy

**Figure 1.Geothermal potential zones worldwide.**

Given the location of the country, Mexico has great potential on developing this renewable source of energy. It is positioned in the 4$^{th}$ place worldwide of installed capacity, however this energy only represents about 2-3% of electricity production nationwide (Carrasco-Núñez, *et al.,* 2015). The geothermal energy production is generated from four geothermal fields located throughout the country (Figure 2). Cerro Prieto is the oldest and largest geothermal field in operation. It is located in the northwestern part of Mexico and it has the second and third biggest geothermal plants in the world, with an installed capacity of 720 MW.

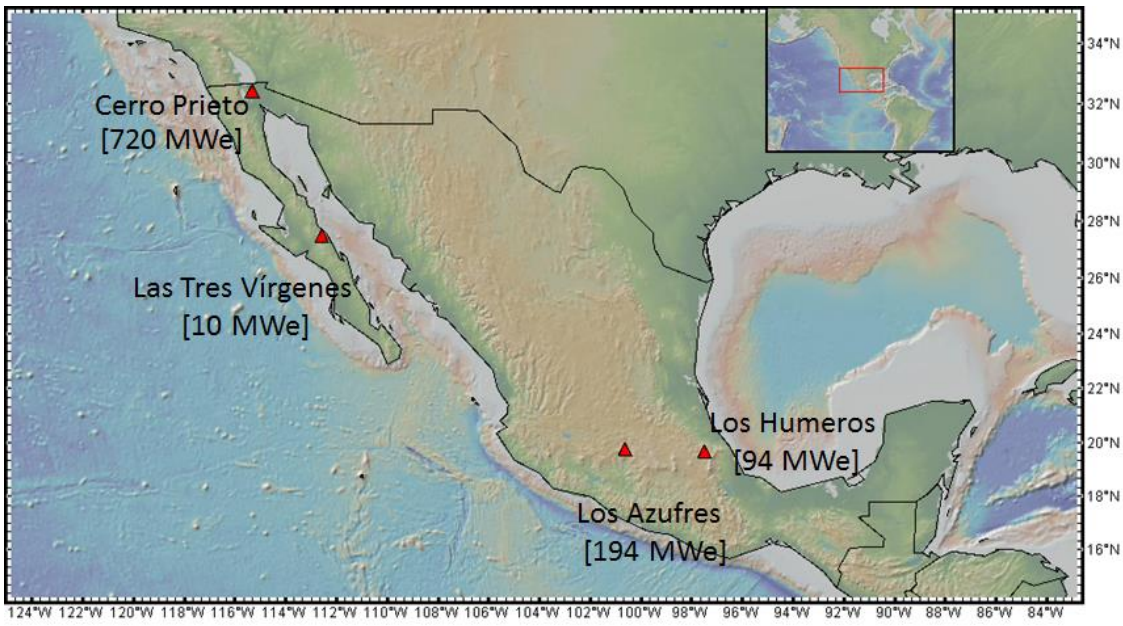


**Figure 2. Geothermal Installed capacity 1,017 MWe (839 MWe running) in Mexico. ( ▲ ) Location of the Geothermal fields.**

Los Azufres is the second geothermal field operating in Mexico. It is located in the central part of the country; 250 km away from Mexico City is a volcanic field type. The total installed capacity is 194 MWe. The geothermal field of Los Humeros is also a volcanic type and is located in the eastern-central part of México, at the eastern end of the Mexican Volcanic Belt, with a total installed capacity of 94 MWe. Lastly, Las Tres Vírgenes, the most recent field in operation in México, is located in the middle of the Baja California peninsula, at the north of the state of Baja California Sur has an installed capacity of 10 MWe (Bertani, 2015; Gutiérrez-Negrín *et al.,* 2015). Nevertheless, given that a fair amount of geothermal potential zones are found offshore, it is worth of consideration to assess them taking into account that the appropriate technology has to be developed to harness it.

Recently, the national geothermal innovation center CeMIE-Geo, which is an academic-industry alliance funded by Mexico's Ministry of Energy (SENER) and the National Science and Technology Council (CONACYT), was created to potentiate the geothermal resources of the country. Thus, one of the projects supported by the center, directed by Dr. Antonio González from CICESE, is an Intensive survey of geothermal exploration in Wagner, Consag, Delfín, Guaymas and Alarcón basins in the Gulf of California rift system. Therefore, thanks to the

support given by Dr. Antonio González, the present project is focused on the exploration over the Wagner and Consag basins.

## 1.2 Study Area

The Gulf of California (GC) is located between the peninsula of Baja California and the states of Sonora and Sinaloa on the northwest part of Mexico. Considered an extension of the Pacific Ocean, is an oblique extensional rift system, where Earth's tectonic plates are being pulled apart and upwelling mantle creates new crust, along the Pacific and North America plate boundary (González-Escobar *et al.,* 2009). The study area is located at the Wagner and Consag basins in the Northern Gulf of California (NGC) as shown in Figure 3.

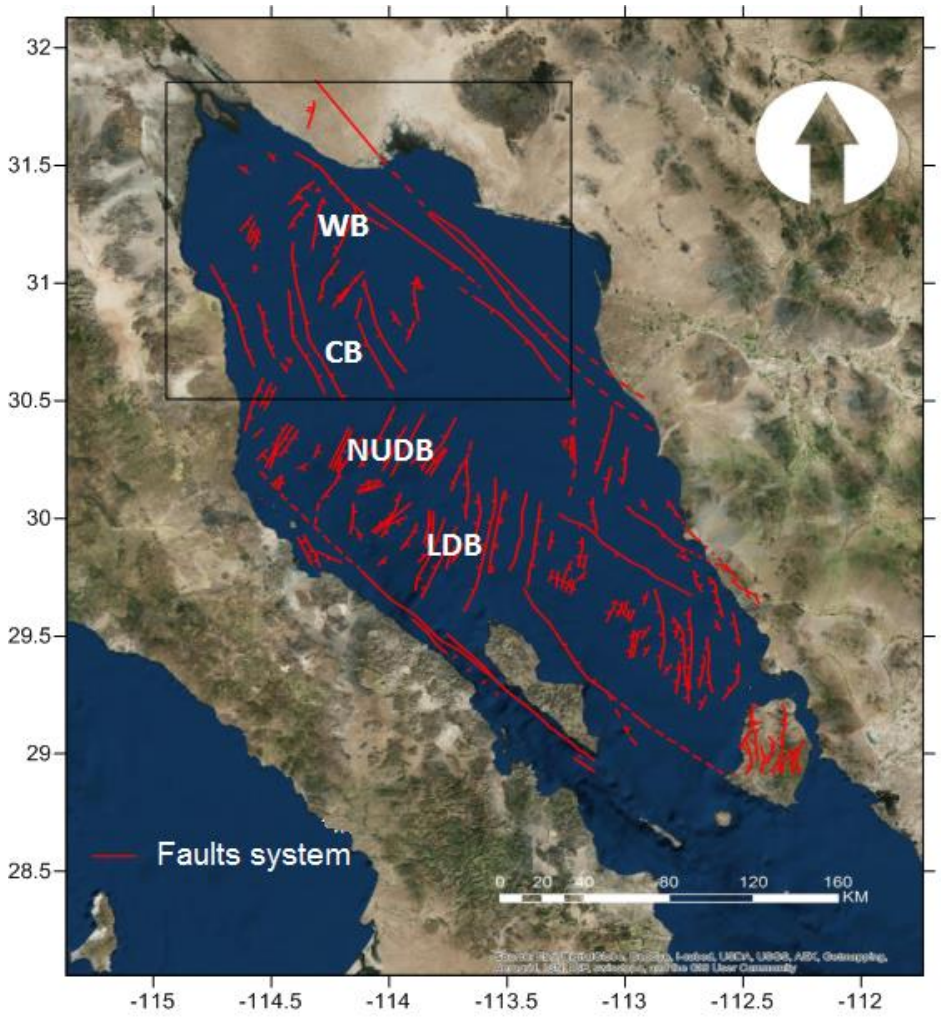


**Figure 3. Study Area located in the Northern Gulf of California (NGC). Faults system reported by Martín-Barajas, *et al.,* (2013). WB: Wagner Basin, CG: Consag Basin, NUDB: Northern Upper Delfín Basin and LDB: Lower Delfin Basin.**

## 1.3 Geological Background

Previous geologic studies done on Baja California show that the starting point of the creation of the GC began around 12 million years ago with the formation of a proto-Gulf during the Neogene (Martín-Barajas, 2000). At that time, what corresponds to the peninsula block started to separate off the continent with relative movement westward. This continental break was consequently a process of extension and a series of related tectonic movements led to the development of major transform faults at the boundary between the Pacific and North America plates during the Pliocene, creating what is now known as the San Andreas Fault system (Stock and Hodges, 1989). By the end of the proto-Gulf (6 million years ago), the Pacific and North America plate motion became localized after the Baja California microplate was transferred completely to the Pacific plate and marine sediments were deposited in the northern region of the Gulf (Oskin *et al.,* 2001, González-Escobar, 2014). Consequently, due to the thinning and rupturing of the crust and lithospheric mantle, *small pull-apart* basins formed along the GC, characterized for being subsiding sedimentary basins formed by the oblique extensional system located and connected by transform faults with right lateral direction (Lonsdale, 1989; Martín-Barajas, *et al,*. 2013).

The NGC is defined by the presence of several incipient spreading centers (González-Escobar, 2009), where these spreading centers are produced by active rift basins systems however also inactive basins are found along the GC. Persaud *et al.*, 2003 defined the active basins as the (1) Lower Delfin Basin (LDB) and Salsipuedes Basins, (2) the Northern Upper Delfín Basin (NUDB) and Southern Upper Delfín Basin (SUDB) and (3) the Wagner Basin (WB) and Consag basin (CB) (Figure 3). For the present project, the study area comprehends the WB and CB, and even though they don't show similar structure they have similar orientation and shallow relief.

Before human intervention, the Colorado River deposited a large amount of sediments into the NGC; with an average sediment accumulation rate of 100 cm/thousand years since the latest Miocene time (Nix, 2013). Thus, the Wagner and Consag basins are filled with around 6-7 km of sediments. These basins are the shallowest found in the Gulf of California, with maximum depths ~230 m.

Although historical heat flow studies didn't indicate any high heat flow anomalies on the northern part of the Gulf (Sánchez-Zamora *et al.*, 1991), Prol-Ledesma *et al.,* (2013) carried out heat flow and geochemical studies over the area, providing evidence of hydrothermal activity over the Wagner and Consag basins: mean heat flow values of 1,875 $mWm^{-2}$ which is more than 15 times higher than the mean heat flow value for young oceanic crust (~105 $mWm^{-2}$); where the highest values were measured in the Wagner and Wagner south faults; also they measured values of $CO_2/CH_4$ ratio in equilibrium temperatures of 200 °C that match what has been seen in other sedimentary basins with active hydrothermal systems; furthermore they found a methanogenic bacteria that lives in ecosystems where the temperature ranges are 75 – 105°C, its presence is normally associated with hydrothermal systems and their occurrence correlates to the largest flares located in the northeastern Wagner basin.

The highest density of faults throughout the NGC are found in the WB and CG basins, and despite the great accumulation of sediments some of the faults reach the top of the seafloor, creating a permeable area predisposed to allow outflow within the faults. Based on seismic reflection profiles in the NGC, the acoustic basement is found at depths greater than 7 km, that is the basement is not being identified at greater depths than these because there is no seismic resolution (González-Escobar *et al.,* 2009; Martín-Barajas *et al.,* 2013).

This research aims to identify hydrothermal areas associated with sources of heat, by the acquisition, processing and inversion of marine Controlled Source Electromagnetic Method developed in Scripps Institution of Oceanography, UCSD. Its application allows characterizing the electrical conductivity hence to associate it with the temperature in the shallow oceanic crust.

## 1.4 Controlled Source Electromagnetic Method (CSEM)

Geophysical exploration methods to describe the subsurface of the Earth have been employed to detect and study geological structures either for academic or industry purposes. In particular,

electromagnetic (EM) methods have been developed over the last few decades using electrical conductivity as a proxy for porosity and rock type (Constable, 2013). Geophysical EM methods are based on the measurement of electromagnetic fields associated with alternating currents induced in the Earth's subsurface by a primary source. The primary source can be originated from a natural source such as the plane waves produced by the interaction of solar wind with the main geomagnetic field of the Earth or lightning, or it can be produced artificially by injecting an alternating current through a coil or along a wire placed over the ground; these two different approaches are known as the Magnetotelluric (MT) and Controlled-Source Electromagnetic (CSEM) methods respectively. The principle is the same in both cases, a primary field spreads out in space until it reaches a surface where induces currents in conductors beneath it. These currents generate secondary EM fields which alter the primary field giving a resultant field which can be measured by a receptor coil providing information such as intensity, phase, and direction of the field. By knowing this information, the subsurface can be quantified into a physical parameter, known as the electrical conductivity (Weitemeyer, 2008; Sharma, 1985).

Although MT and CSEM methods help to quantify the electrical conductivity of the earth in land and marine environments; their application was initially restricted only to terrestrial environments since it was believed that the electrical conductivity of the seawater was very high and it would prevent EM field propagation into the seabed. However, in the 1960's Charles Cox and Jean Filloux from Scripps Institution of Oceanography developed the first equipment suitable for deep seafloor MT and CSEM experiments (Maza-Vázquez, 2015; Constable, 2010). This and subsequent studies demonstrated that EM methods can be applied effectively in marine environments (e.g. Chave and Cox, 1982; Constable and Cox, 1996).

On the other hand, the first development of the marine CSEM method had the objective of using the lost high frequencies signals due to attenuation by the seawater in MT to study the electrical structure of the upper oceanic lithosphere (Cox *et al.*, 1986). After being applied in academia for many years mostly to study ocean basins and active spreading centers, Ellingsrud *et al.,* (2002) successfully targeted a hydrocarbon reservoir beneath the seafloor. Subsequently, the method has been incorporated in offshore hydrocarbon and gas exploration (Eidesmo *et al.*,

2002; Constable, 2010), and more recently have been demonstrated to be effective for mapping gas hydrates (Weitemeyer*et al.*, 2006).

Nowadays, in the marine environment MT uses EM energy in the frequency band of 0.0001 – 10 *Hz* whereas in CSEM, the typical frequency operation is from 0.1 – 10 *Hz*. Consequently, the CSEM method is capable of mapping shallower structures and is sensitive to resistive bodies present in the subsurface, whereas MT has greater depths of penetration and is more sensitive to conductive bodies. Depending on the target of interest the CSEM method requires modifications to increase its capacities, for example for mapping gas hydrates, which occur in the shallow areas of the seafloor (hundreds of meters in depth) and is characterized by having just a few *Ωm* of resistivity changes, higher frequencies, and short ranges are needed to distinguish the top of hydrate, and low frequencies and long ranges will discriminate the bottom of hydrate (Weitemeyer *et al.*, 2006; Weitemeyer, 2008).

The conventional CSEM survey (Figure 4) consists of a frequency domain technique where receivers are deployed on the bottom of the seafloor and an electric dipole transmitter is towed on or close to the seafloor in order to maximize the amount of electromagnetic energy transmitted into the subsurface. This method penetrates less but offers a better lateral coverage because the measurements are taken continuously over long lines as the ship moves.

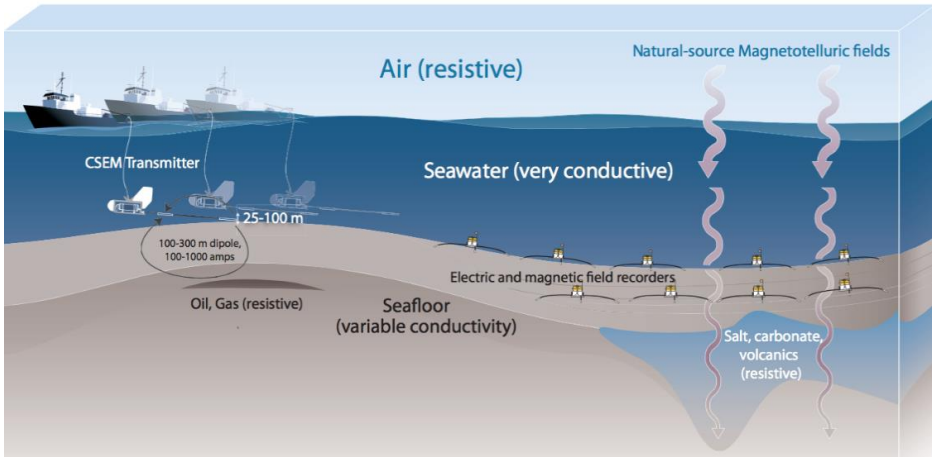


**Figure 4: Conventional CSEM system. An electric dipole transmitter is towed above the seafloor and an alternating electromagnetic field is transmitted along the antenna, which can be 50 m to 200 m long. Seafloor receivers record the electric and magnetic fields from the transmitter (extracted from Constable, 2013).**

As mentioned before, depending on the frequency, CSEM can be used for shallow subsurface investigation and since the electrical conductivity depends on temperature and phase state, a possible definition of fluid distribution can be a pursuit to locate hydrothermal sources or even describe faults. Given that the maximum water depths found over the study area are less than 250 *m*, an alternative setup that consists on towing the transmitter and receivers below the sea surface can be applied (Shantsev, 2012; Anderson, 2010; Linfoot *et al.*, 2011). Yet, few experiments using surface towed systems have been employed; the present project described in this thesis is based on the acquired data over the North Gulf of California using a towed setup developed by Scripps Institution of Oceanography.

## 1.5 Objectives

### General Objective

a) Identify hydrothermal flow zones associated to possible high heat flow sources.

### Specific Objectives

b) Employ the methodology provided by SIO/UCSD to carry out the processing and inversion of the acquired CSEM data during the survey over the Wagner basin.

c) Characterize the electrical resistivity of the shallow oceanic crust.

d) Interpret the marine electromagnetic electrical resistivity profiles obtained through the inversion modelling.

# Chapter 2. Basics of electromagnetism

Maxwell's equations govern the behavior of electromagnetic fields in the air, in the ocean and below the seafloor (e.g. Griffiths, 1999). This discovery led to what we have known as Maxwell's equations, and their role is crucial in describing the propagation of electromagnetic waves:

$$\nabla \cdot \mathbf{D} = q \qquad \text{Gauss Law (Electric field)} \qquad (1)$$

$$\nabla \cdot \mathbf{B} = 0 \qquad \text{Gauss Law (magnetic field)} \qquad (2)$$

$$\nabla \times \mathbf{H} = \mathbf{J} + \frac{\partial \mathbf{D}}{\partial t} \qquad \text{Ampere-Maxwell Law} \qquad (3)$$

$$\nabla \times \mathbf{E} = -\frac{\partial \mathbf{B}}{\partial t} \qquad \text{Faraday-Lenz's Law} \qquad (4)$$

In these equations the electric field, **E** (V/m), magnetic induction, **B** (Tesla), the dielectric displacement, **D** (C/m$^2$), the intensity of magnetic field **H** (A/m), current density **J** (A/m$^2$), charge density, q (C/m$^3$) and time, t (s).

Equation (1) is Gauss's Law, it tells us that an electric charge of any shape produces an electric field and it states that the flux through any surface enclosing a given charge will equal the total charge inside. Equation (2) corresponds to the Gauss's formula for magnetism. It states that the magnetic field lines have no beginning and no end. In other words, magnetic lines are continuous and the divergence of the magnetic field is zero, which proves the non-existence of magnetic monopoles. Equation (3) is Ampere-Maxwell equation, it states that the current enclosed by an Amperian loop will generate a magnetic field, and a moving charge induces a magnetic field. In other words, it tells us that a magnetic field can be produced by a current or by a changing electric field. Equation (4) describes the phenomenon of electromagnetic induction. A magnetic field varying in time is able to generate an electric field and as a result an electromotive force (voltage) appears.

Displacement currents are not significant at the frequencies and conductivities relevant in marine electromagnetic methods. The quasi-static approximation for Maxwell's equations is applicable in this case. Using Equation (3) and the identity equation $\nabla \cdot \nabla \times \mathbf{A} = 0$ it is shown that:

$$\nabla \cdot \mathbf{J} = 0 \tag{5}$$

In matter, the behavior of the electromagnetic fields is defined by three primary properties of the medium: electrical conductivity σ, electrical permittivity ε and magnetic permeability μ, where **B** and **H** are related by magnetic permeability μ, **J** and **E** by conductivity σ and **D** and **E** by permittivity ε:

$$\mathbf{B} = \mu \mathbf{H} \tag{6}$$

$$\mathbf{J} = \sigma \mathbf{E} \tag{7}$$

$$\mathbf{D} = \varepsilon \mathbf{E} \tag{8}$$

Where Equation (7) is the known Ohm's law. It describes the linear relation between the voltage and current in a conductor. The electrical conductivity represents the material's ability to allow the transport of an electric charge with units of Siemens per meter (S/m) with values between $10^0$ and $10^{-6}$S/m in typical rocks. The inverse of the conductivity is the resistivity ρ, with units of$\Omega$m. The electrical permittivity is equal to approximately 8.85 x $10^{-12}$ farad per meter (F/m) in free space (a vacuum), between $10^{-9}$ and $10^{-11}$ (F/m) depending on water content. If no materials or rocks with large magnetite content are present, $\mu_0 = 4\pi \times 10^{-7}$ (N/A$^2$), so Equation (6) becomes (Constable, 2010; Maza-Vázquez, 2015):

$$\mathbf{B} = \mu_0 \mathbf{H} \tag{9}$$

Consequently, Equations (3) and (4) are rewritten as:

$$\nabla \times \mathbf{H} = \sigma \mathbf{E} \tag{10}$$

$$\nabla \times \mathbf{E} = -\mu \frac{\partial \mathbf{H}}{\partial t} \tag{11}$$

Considering σ and μ constant, and taking the curl of Equations (10) and (11):

$$\nabla^2 \mathbf{E} = \mu \frac{\partial}{\partial t}\left(\nabla \times \mathbf{H}\right) = \mu\sigma \frac{\partial \mathbf{E}}{\partial t} \tag{12}$$

$$\nabla^2 \mathbf{H} = \sigma\left(\nabla \times \mathbf{E}\right) = \mu\sigma \frac{\partial \mathbf{H}}{\partial t} \tag{13}$$

These equations represent diffusive phenomena. From Fourier transform we know that a signal can be seen as the sum of sines and cosines, therefore if we consider sinusoidal varying fields of angular frequency ω, recalling that $\frac{\partial}{\partial t} e^{i\omega t} = i\omega e^{i\omega t}$:

$$\mathbf{E}(t) = \mathbf{E_0} e^{i\omega t} \tag{14}$$

$$\mathbf{H}(t) = \mathbf{H_0} e^{i\omega t} \tag{15}$$

Therefore:

$$\nabla^2 \mathbf{E} = i\omega\mu\sigma \mathbf{E} \tag{16}$$

$$\nabla^2 \mathbf{H} = i\omega\mu\sigma \mathbf{H} \tag{17}$$

If we consider horizontal polarization with a vertical propagation (*z*), the previous equations reduce to:

$$\frac{\partial \mathbf{E}}{\partial z^2} + k^2 \mathbf{E} = 0 \tag{18}$$

$$\frac{\partial \mathbf{H}}{\partial z^2} + k^2 \mathbf{H} = 0 \tag{19}$$

The solutions:

$$\mathbf{E}(t) = \mathbf{E_0} e^{ikz} = \mathbf{E_0} e^{-i\alpha z} e^{i\beta z} \tag{20}$$

$$\mathbf{H}(t) = \mathbf{H_0} e^{ikz} = \mathbf{H_0} e^{-i\alpha z} e^{i\beta z} \tag{21}$$

Where:

$$k = \sqrt{i\omega\mu\sigma} = \alpha - i\beta \tag{22}$$

The “skin depth” is defined as

$$\delta = 1/\alpha = 1/\beta = \sqrt{\frac{2}{\sigma \mu_0 \omega}} \tag{23}$$

This depth depends on the resistivity of the medium and the frequency of the source field. It represents the distance over which the field amplitude in the medium is reduced to *1/e*, or about 37% (given by $\alpha$), and the phase progresses one radian, or about 57% (given by $\beta$). In meters for a given period T in seconds, it’s approximately

$$\delta \approx 503\sqrt{\rho T} \tag{24}$$

“The skin depth concept underlies all of inductive electromagnetism in geophysics. Substituting a few numbers into the equation shows that skin depths cover all geophysically useful length scales from less than a meter for conductive rocks and kilohertz frequencies to thousands of kilometers in mantle rocks and periods of days (Table 1)” (Constable, 2007).

**Table 1. Skin depth approximations varying the source field frequency for different media**

| *Material* | *σ (S/m)* | *1 year* | *1 month* | *1 day* | *1 h* | *1 s* |
|---|---|---|---|---|---|---|
| *Core* | $5 \times 10^5$ | 4 km | 1 km | 209 m | 43 m | 71 cm |
| *Lower mantle* | 10 | 883 km | 255 km | 47 km | 9 km | 160 m |
| *Seawater* | 3 | 1600 km | 470 km | 85 km | 17 km | 290 m |
| *Sediments* | 0.1 | 9000 km | 2500 km | 460 km | 95 km | 1.6 km |
| *Upper mantle* | 0.001 | $3 \times 10^4$ km | $10^4$ km | 1500 km | 300 km | 5 km |
| *Igneous rock* | $1 \times 10^{-5}$ | $10^6$ km | $2 \times 10^5$ km | $5 \times 10^4$ km | 9500 km | 160 km |

# Chapter 3. Data and Methodology

The research survey was carried out over the Wagner and Consag basins at the NGC during May 2015. It consisted of two parts (or legs) where CSEM data were collected using a transmitter – receivers towing system. The first leg was from 5 to 8 of May, and the second leg was from 20 to 24 of May. The research instrumentation and equipment was provided by Scripps Institution of Oceanography from the University of California San Diego (SIO, UCSD), mounted on "Buque Oceanográfico Alpha Helix", the research vessel of CICESE, as part of the Intensive survey of geothermal exploration in Wagner, Consag, Delfín, Guaymas and Alarcón basins in the Gulf of California rift system, led by Dr. Antonio González from CICESE.

## 3.1. CSEM towing system

There are different ways to employ the CSEM method to study the electrical conductivity of the sea-floor. In industry and in academic research different models have been developed to map a target area; in particular, for this survey SIO used a Controlled-Source Electromagnetic system that is different from what has been used in previous years (e.g. Ellingsrud *et al.*, 2002; Myer *et al.*, 2010; Weitemeyer *et al.*, 2011). Although this CSEM system was firstly designed to study permafrost located in a 0-10 *m* of water depth in the Arctic, it can be used in deeper scenarios with high probability of having positive results (e.g. Shantsev *et al.*, 2012; Engerlmark *et al.*, 2014).

The new CSEM system consists of a transmitter and four receivers that are towed along the sea surface as seen in Figure 5. Four receivers are separated by a distance of approximately 250 *m* from each other; and the transmitter injects electrical current into a floating antenna placed behind the vessel along a floating rope. Since in this case, the study area has known water depths up to 200 m, the transmitter unit was modified to inject currents up to 100 *A*. Continuous measurements are taken according to the path followed by the ship; Figure 6 displays the followed ship track divided into two legs.

The decision to use this transmitter–receivers towing system was due to two main reasons: first, the water depths found in the study area are less than 250 meters, therefore, the sensitivity and inversion results may be as good as the ones using the deep towed transmitter system as reported in Shantsev *et al.,* (2012); and second, the hydrothermal manifestations, which are the main target, have been found in the shallow subsurface as reported by Prol-Ledesma *et al.,* (2013), thus the 1 km maximum depth, determined by the source-receiver spacing at which we have sensitivity, will provide enough information about the area.

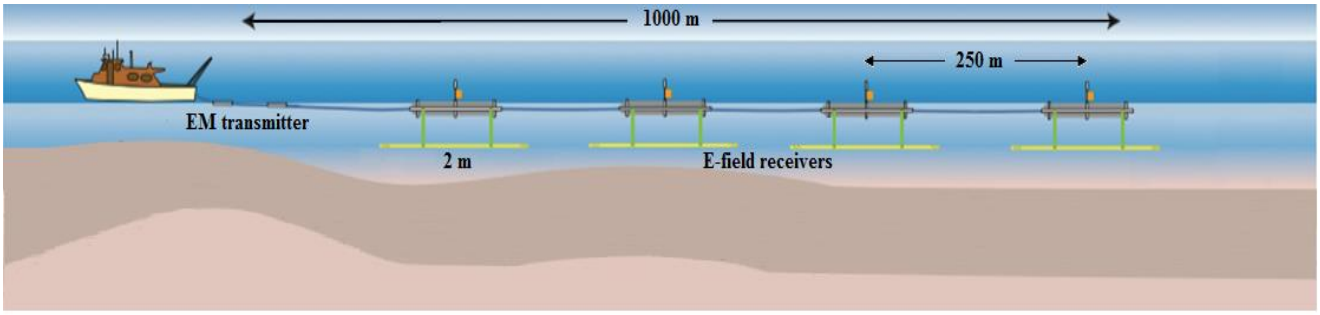


**Figure 5: CSEM Transmitter - Receivers system used during the survey. Separation distance between the closest and farthest receiver of about 1 *km*. The array is towed below the sea surface taking continuous measurements in accordance to the ship track.**

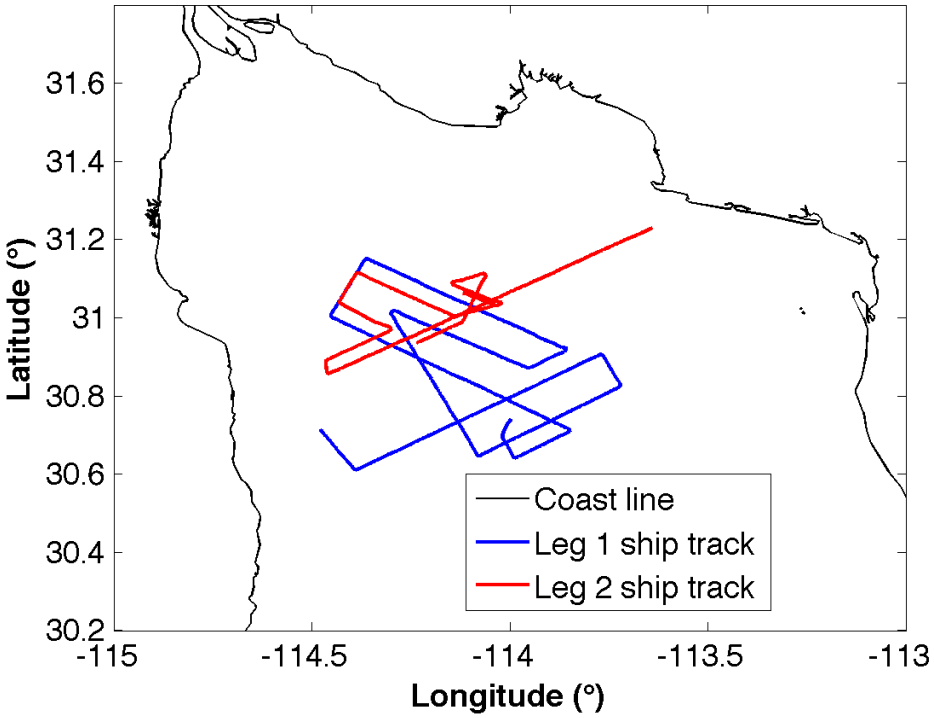


**Figure 6: Ship track followed during the two legs of the survey. Blue color represents the path followed during the first leg and red color for the second leg.**

### 3.1.1. Transmitter

The function of the transmitter is to emit the electrical current as needed through the seawater to produce an electromagnetic (EM) field that will propagate and diffuse through the air, ocean and seafloor in accordance to the earth's response described by Maxwell's laws. The variations of the EM field are directly related to the conductivity of the media and these are measured by the receivers.

The current, known as the source signal, is a time series typically transmitted as a complex binary waveform (varies between a positive and a negative signal level) with a fundamental frequency between 0.1 to 0.25 *Hz* (Key, 2012; Constable, 2010). Since the exploration target frequency at which is sensitive is not known, simultaneous multiple frequencies are broadcast; for this experiment, the transmitted binary signal was based on the

"D" waveform, described in Myer *et al.,* (2011) with modifications on the amplitude and phase values to be discussed later in more detail.

On the other hand, unlike the conventional system where the transmitter is deep towed above the sea-floor (see Figure 4), in our experiment, the process consists of transmitting the waveform signal from the ship using a coaxial cable down to the transmitter antenna which was towed behind the vessel. The antenna is made using two copper pipes (electrodes) to form the Horizontal Electric Dipole (HED); for the first leg it was 50 *m* long with an output current of about 65 A zero to peak, whereas for the second leg, it was 43 *m* long with an output current of about 90 A zero to peak. The difference between the desired 100 A value for the output current and the measured one was due to a complication with the circuit breaker which was tripping during the supply of 240 VAC power to the transmitter antenna.

The length, current and waveform of the transmitter will define its electric Source Dipole Moment (SDM), which is given by the length of the electric dipole antenna l times the zero to peak amplitude of the electrical current $I$, with units of *Am* (Constable and Weiss, 2006). The SDM is proportional to the electric field strength, therefore if the SDM increases, then the measured electric field signal will also increase. The SDM for the first leg was 3.5 *kAm*, and for the second leg, it was 3.87 *kAm*.

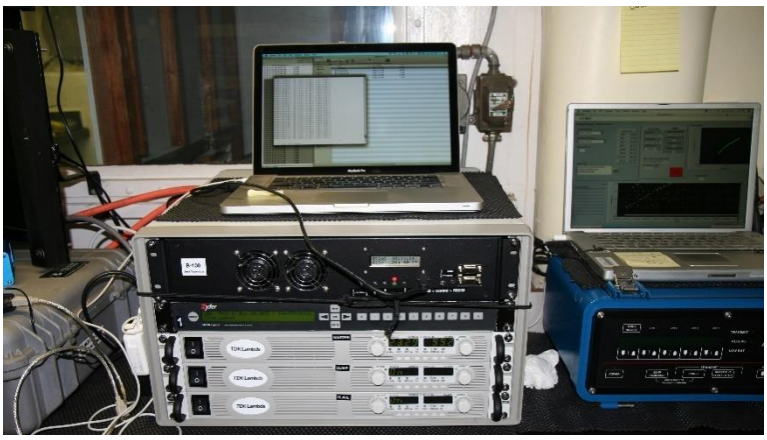

**Figure 7: Transmitter power supply (left) and Benthos Acoustic Navigation (right) system installed inside the ship.**

### 3.1.2. Receivers – Porpoises

Four receivers, named Porpoises, were used to measure the amplitude attenuation and phase shift of the transmitted horizontal electric field. The above was accomplished using electric field sensors made from Ag-AgCl (silver-silver chloride) material. See Webb *et al.,* (1985); Filloux (1987) and Constable (2013) for more detail explanation of its conceptual construction.

When the electrical field propagates through the media, the signal couples with the sea-floor rocks traveling afterward to the receivers. The coupled responses of the electric field, acceleration on x, y and z components and the GPS timing were recorded as time series by an EM logger system (Figure 9). Additionally, compasses to measure pitch, roll and heading were placed on the head of each porpoise to infer the relative orientation of the receiver; their exact locations were registered by a GPS antenna mounted on top of each porpoise as shown in Figure 8. Nevertheless, due to gaps of the recorded data, it was assumed the receivers were in line to the transmitter antenna, despite the surface ocean currents and wind that would drift the whole array a certain angle.

The GPS logger allows synchronizing the instrument's clocks before deployment in order to record the timing continuously in all of the receivers and transmitter as accurate as possible. Their accuracy was about 20 microseconds clock drift (Constable, 2013).

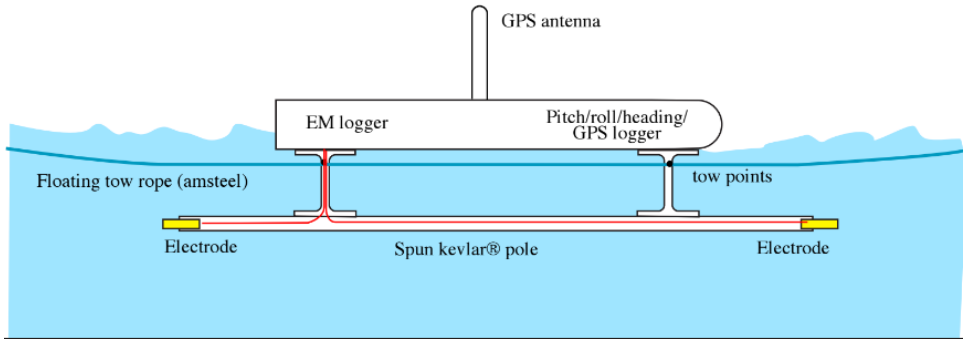


**Figure 8: Receiver – Porpoise system.**

### 3.2. Data processing

As mentioned before, the data are recorded as time series, but since it's difficult to quantify the raw data from the Earth's response, it is necessary to use processing techniques in order to recognize it. (Pankratov and Geraskin, 2010). The channel 1 in Fig. 9 shows the raw time series of the measured E-field amplitude signal for the closest porpoise to the transmitter.

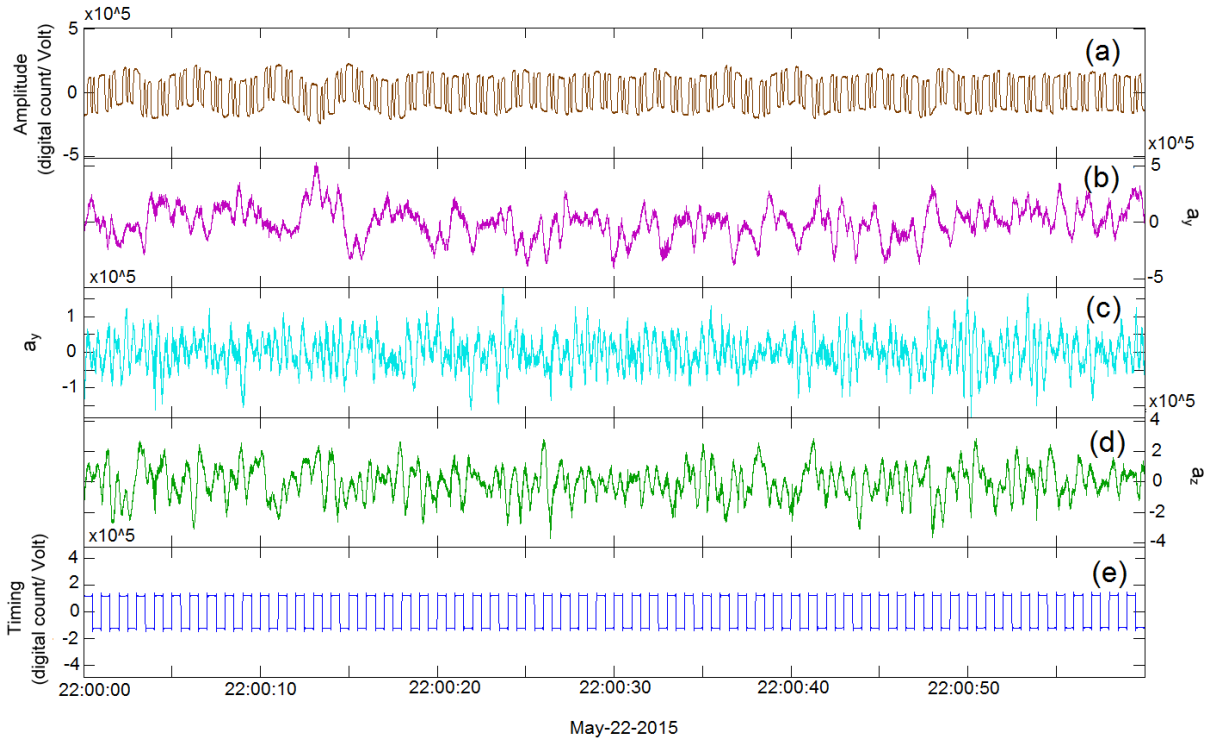


**Figure 9: Raw time series recorded by the EM logger for the closest receiver to the transmitter. (a) Amplitude of $E_y$, (digital count/V) (b) acceleration on x, (c) acceleration on y , (d) acceleration on z, (e) timing (digital count/V) vs. Time (hh:mm:ss).**

Thus, the raw time series recorded in channel 1 by the receivers (Figure 9) were processed into the frequency domain based on the algorithm detailed in Myer *et al.,* (2011): The objective is to extract the Earth's coupled response from the raw time series, namely the Transfer Function (TF) into the frequency domain. To do so, first using the Fast Fourier Transform (FFT) the data is transformed into the frequency domain to extract the amplitude and

phase of the signal using a 2 *s* time window frame at the fundamental frequency 0.5 *Hz* and the three biggest harmonics: 1.5, 3.5 and 6.5 *Hz*. Then, since the entire electromagnetic spectrum is measured, some MT signal noise can occur on the red length wave causing contamination, so the data are pre-whitened using the first difference, hence be post-darkened to remove the amplitude and phase effects produced by the first difference. Afterward the data are corrected for the amplifier response and then normalized by the SDM to obtain the TF at each frequency for the 2 s windows. Finally, the obtained TF estimates were stacked using an arithmetic mean to obtain the TF for every 2 min to yield final units of $V/Am^2$.

During the towing, the complex binary waveform was continuously recorded into a data logger in order to store the exact output current injected through the transmitter antenna (Figure 10). This new modality is different from what has been used before; one example is the research study done over the Scarborough gas field off the northwest coast of Australia (Myer *et al.*, 2012), they used a current clamp to measure the output current of the transmitter and periodically recorded snapshots of the waveform. Therefore, as long as the output currents don't change over time the SDM can be calculated and applied to the data processing.

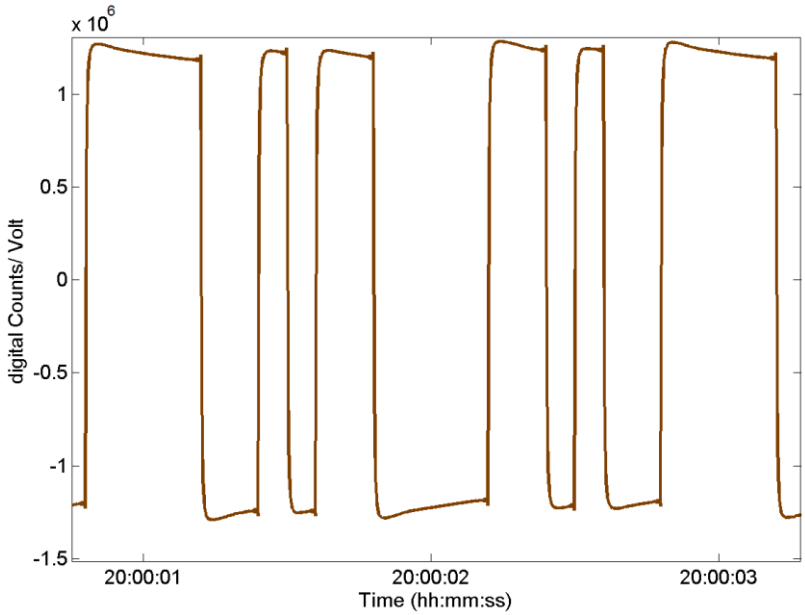


**Figure 10: Recorded binary complex waveform during the first leg of the cruise with units of Digital Counts/ Volt. The fundamental frequency is 0.5 *Hz* which corresponds to the 2 seconds period peak to peak waveform, as for three biggest harmonics 1.5, 3.5 and 6.5 *Hz* are identified as the shorter period's cycles within the signal.**

During the towing the current values displayed on the transmitter didn't match the values recorded by the transmitter's data logger, we don't know exactly why this difference existed in the first place, and therefore it was necessary to calculate the value of the current and the waveform coefficients that define the binary complex waveform. The amplitude waveform results are shown in Table 2. The currents for the first leg fluctuated between 55 and 70 *A*, for the second leg they were between 85 and 92 *A*.

**Table 2: Calculated new waveform coefficients**

| Harmonic number | Amplitude | Phase |
|---|---|---|
| 1 | 0.35 | 0 |
| 3 | 0.9001 | 180 |
| 5 | 0.7583 | 0 |
| 7 | 0.4055 | 180 |

The waveform amplitude results were used to process the collected data. It's very important to know the exact value of the current since the TF are normalized by the SDM; namely, if either the current or the dipole antenna length are incorrect this will lead to a misinterpretation since the resistivity values will be determined in correspondence to the E-field amplitude signal for every ship position.

Figure 11 shows the 3.5 Hz processed response for the 4 receivers, the closest one is on the top left corner, and the farthest one is on the bottom right; the darker points correspond to the $E_y$ field transfer function amplitude estimates whereas the lighter points are the variance estimates. As described in (Myer *et al.*, 2011) performing an average of 2 min stacked TF allows the calculation of the variance.

The variance $s^2$ is a measure of how spread out is a data set about the mean. If the variance is small, it means that the values are quite grouped set. If the variance is large, it

means that the numbers are more dispersed and it is the square of the standard deviation. Instead of using standard deviation, statisticians prefer to use variance for a couple of reasons. One is that its covariance is a squared measure and the other is that the variance of a sum of random variables equals the sum of the variances. Myer *et al.*, (2011) processing code, estimates the variance during stacking, and later takes the square root to get an error estimate. If the error estimate is correct, then it should be the same as the "noise floor" when there is no CSEM signal.

The above gives us the value of Noise Floor (NF), which can be understood as the magnitude of the measurement when no current is injected through the media. In these case, the NF is around $10^{-11}$ $V/Am^2$ and it depends on the instrument calibration, ocean currents, navigation, output current, and other environmental variables.

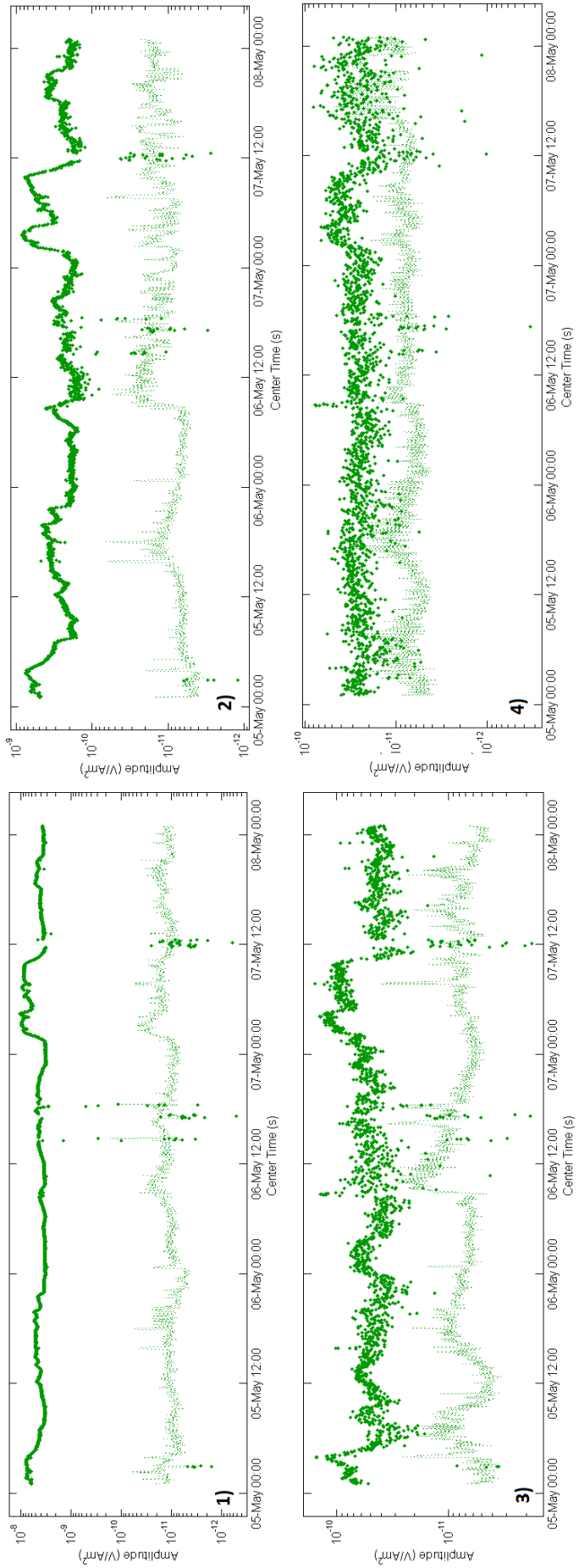


**Figure 11. Processed amplitude responses for the frequency 3.5 Hz for the 4 receivers. In all the plots, the darker points correspond to the $E_y$ field transfer function amplitude estimates whereas the lighter points are the standard deviation estimates. In ascending order 1) represents the closest receiver and 4) the farthest one to the transmitter.**

On the other hand, the Signal-to-Noise Ratio (SNR) is the ratio between our data and the noise floor; namely, it describes how different is the signal from the noise floor. The SNR allows us to get rid of bad data, if the SNR is close to 1, it means we would be working with noise instead of the real measurement. For instance, in Figure 12 are shown some sections where the SNR < 10 and those values have to be eliminated. Overall, SNR values are excellent for the first two receivers, adequate for the third receiver, and borderline for the fourth receiver. For that reason, the data from the fourth receiver was omitted in our work.

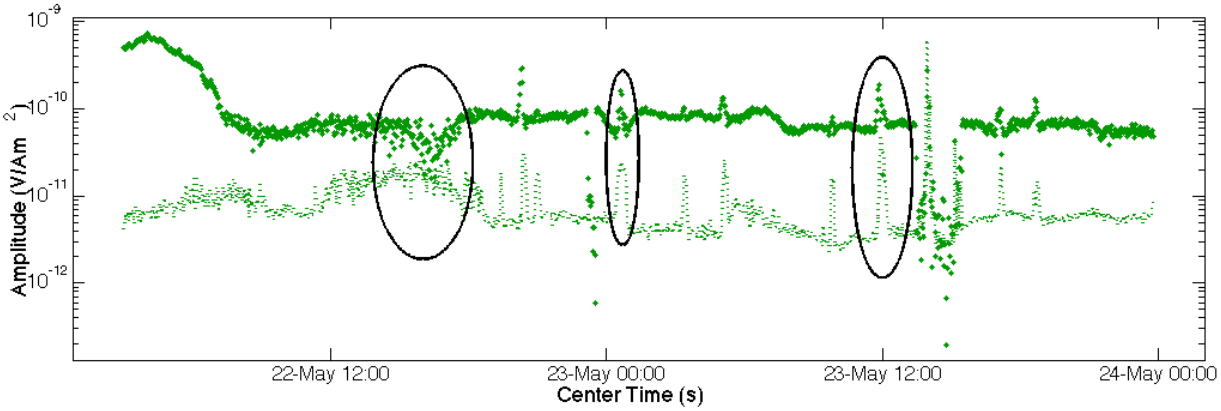


**Figure 12: Example of the sections in the third instrument where the SNR < 10, those measurements have to be discarded.**

### 3.3. Operational challenges

Since the system is towed along the sea surface, the characteristics of the ocean will determine the accuracy of the data; and factors such as the ocean currents, wind, navigation, sea water conductivity and bathymetry have to be carefully measured in order to model and invert the processed EM data.

### 3.3.1. Navigation

While the ship is crossing over the target area, continuous measurements of the amplitude and phase of the electric field are being recorded by the receivers. Simultaneously, the ship is mapping the bathymetry necessary to quantify the electrical conductivity of the seafloor, hence to validate the navigation information.

Having a surface towing system allows an easier way to estimate the ship position using a GPS system in comparison to the conventional CSEM setup (Shantsev, 2012). For this survey, the ship position and water depth were measured every second using the Benthos BS-7000 acoustic navigation system.

Timing has to be synchronized between the Benthos system and the one recorded by the instruments because this parameter allows us to establish the exact position of the ship when the E-field measurement is made, hence to associate the corresponding water depth. However, the water depth calculated with the Benthos system was inaccurate so we had to estimate it with Echo-sounder measurements taken during the survey campaign separately; this was done by matching the ship positions measured by both the Benthos system and the Echo-sounder to assign the correct water depth. Consequently, the bathymetry employed for the following work is the one calculated with the Echo-sounder data provided by Dr. Guillermo Díaz (personal communication). It's very important to guarantee all timings are correct since having the wrong water depth will compromise the accuracy of the data modelling and inversion (see Figure 13).

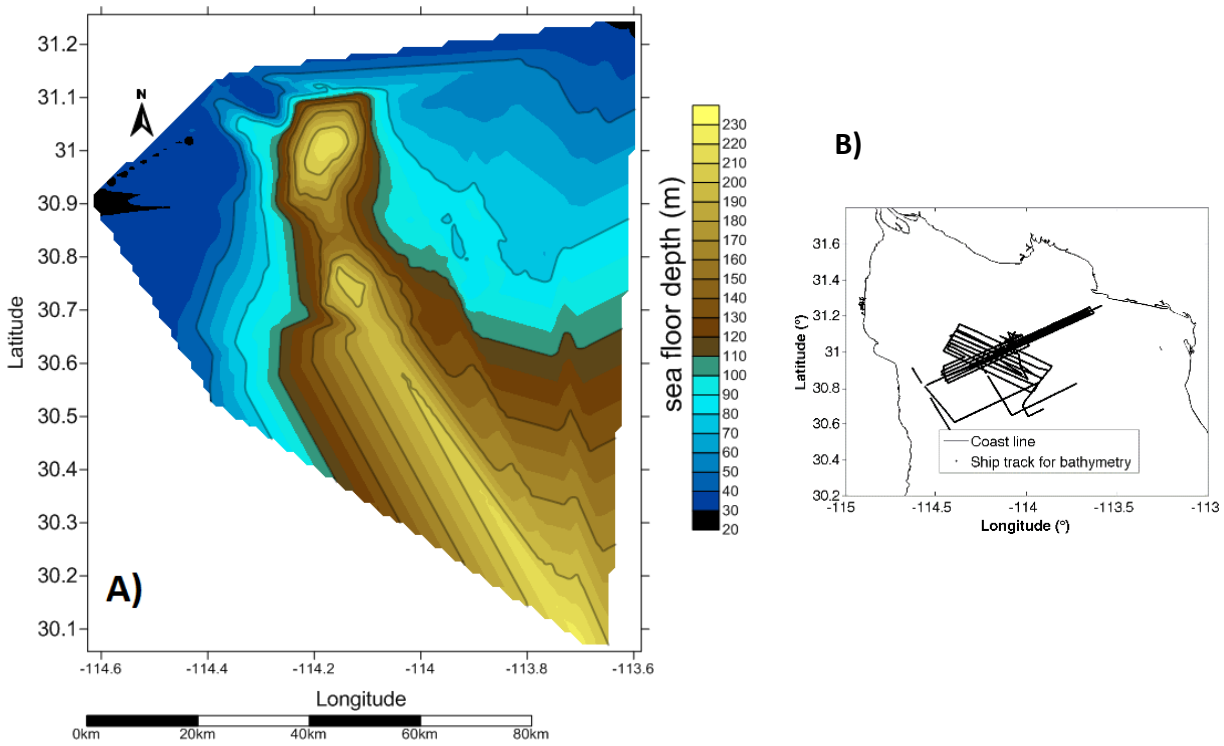


**Figure 13: A) Bathymetry of the Wagner and Consag basins. B) Followed ship track to obtain the bathymetry measurements using the Echo-sound; the processed data was provided by Dr. Guillermo Díaz Mendez.**

### 3.3.2. Seawater conductivity

Electromagnetic propagation through water has a very different behavior than propagating through the air or the seafloor due to the water's electrical conductivity and high permittivity (defined as how much the molecules of water oppose to the external propagation E-field). Since CSEM method involves the propagation of E-field signals firstly through the water, the amplitude of the measured signal will depend on how conductive is the seawater as the signal loss will be largely due to the effect of conduction of the electric field through the water (Rhodes, 2008). Moreover, recent work has shown that the electrical conductivity structure of the seawater layer must be included to obtain accurate modelling results.

Typical seawater conductivity (σ) values at normal seafloor temperatures (in Celsius) ranges are from 3.2–5 *S/m* depending on salinity, temperature and pressure. Becker *et al.,* (1982) proposed a linear relationship to estimate seawater conductivity, which is accurate to 3-5% in a temperature range from 0–200 *°C*.

$$\sigma = 3.0 + 0.1T \; S/m \tag{25}$$

However, Constable *et al.,* (2009) made an improvement to the previous equation by taking the cubic relationship of Perkin y Walker (1972), which is more accurate over the0-25°C and improved the high temperature (100-200 °*C*) extrapolation:

$$\sigma = 2.903916\,(1 + 0.0297175\,T + 0.00015551\,T^2 - 0.00000067\,T^3)\; S/m \tag{26}$$

In order to model and invert the data it is necessary to precisely estimate the seawater conductivity. Modelling the data requires to set the first layer with the seawater conductivity and it has been observed that in the ocean the water column has its largest conductivity variation between a thin surface layer of warm water separated from a thick cold water mass by the main thermocline (Chave and Cox, 1982). In shallow water depths, such as the ones found in the Northern Gulf of California, the seawater conductivity can be estimated with a direct CTD (Conductivity-Temperature-Depth) measurement. In this survey only three CTD's were taken over the area down to 16 m depth estimating seawater conductivities around 5 S/m (Figure 14), nevertheless, these results don't provide enough information to model the seawater layer of the study area.

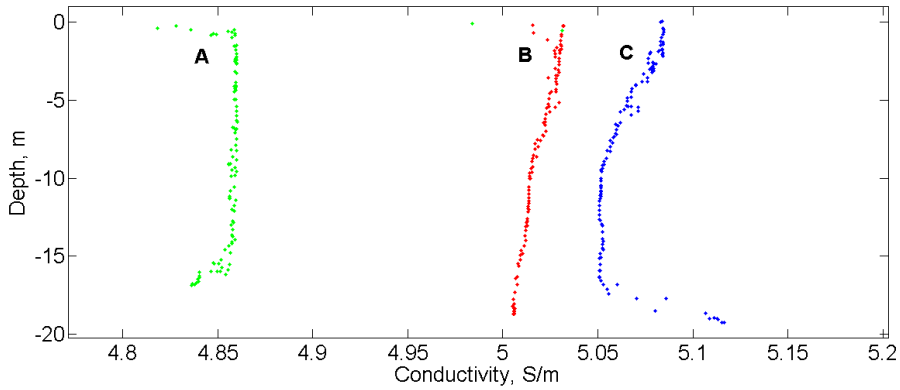


**Figure 14: Seawater conductivity measurements taken during the survey at three different locations. The conductivity (*S/m*) is between 4.85 and 5.1 for the first 16 meters of the water column.**

Previous studies to estimate the seawater conductivity have been carried out over the Gulf of California (Alvarez-Borrego *et al.*, 1975, 1999; Vázquez-Figueroa *et al.*, 2009), since the reported values are salinity and temperature, according to the algorithms given by Fofonoff (1985); they represent conductivity values between 3 and 5 S/m in the Northern Gulf of California (NGC). The water column in the NGC is characterized for being stratified mainly due to the bathymetry of the Wagner basin and other physical processes such as tides and evaporation-precipitation balance (Vázquez-Figueroa *et al.*, 2009). There is fair documented seawater conductivity information over the study area, yet estimating the seawater conductivity for all the water columns is challenging. Due to some complications during the forward modeling, the seawater conductivity had to be set as another variable to be estimated during the inversion.

### 3.3.3. Anisotropy

Earth's geological formations can exhibit different patterns of electrical conductivity depending on the direction of propagation of the E-field. Hence, using isotropic theory to represent such models sometimes can be misleading. The anisotropy found on the formations normally can be solved using geological mapping, however the electrical field propagated through the media

depends on the macroscopic features and it can be described using the EM method by making assumptions of the electrical conductivity tensor that represents the media.

Considering a media with its vertical coordinate axis z measured positive downwards the anisotropic electrical conductivity of the lower half-space (z>0) is given by the diagonal

$$\sigma = \begin{pmatrix} \sigma_x & & \\ & \sigma_y & \\ & & \sigma_z \end{pmatrix} \tag{27}$$

In the isotropic case, $\sigma_x = \sigma_y = \sigma_z$, nonetheless if we consider the uniaxial anisotropic conductivity tensor - that is, one of the directions differs from the other two, - the electrical properties of the media can be described with six different physical cases as shown in Figure 15 (Constable, 2007). For example, considering the bottom case, the model is vertically anisotropic material, the conductivity $\sigma_x$ and $\sigma_y$ are equal and if the $\sigma_z$ is higher, it represents an uncommon model but it might be related to diapiric (geological structure consisting of mobile material that was forced into more brittle surrounding rocks, usually by the upward flow of material) upwelling of melt in a volcanic system. The other case $\sigma_{\parallel} > \sigma_{\perp}$ represents horizontally stratified layers; and ideally this would correspond to interbedded geological strata.

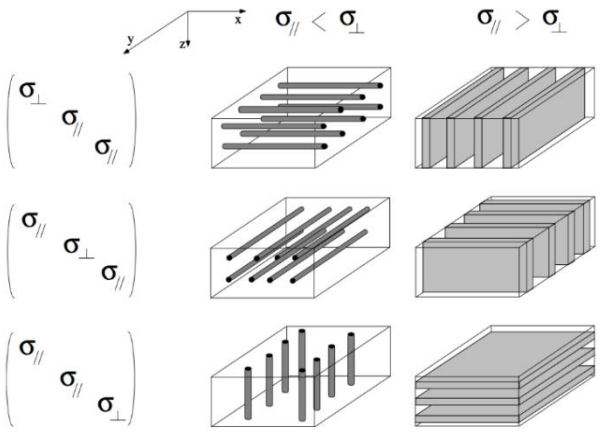


**Figure 15: Different physical cases of a medium with uniaxial anisotropic conductivity tensor. The shaded regions represent a conductor material and the white regions an insulator. Depending on the case, the shape and orientation of the conductors is defined by the relation between $\sigma_{\parallel}$ and $\sigma_{\perp}$, (Reproduced from: Constable, 2007).**

### 3.4. Forward Model

In geophysics, we seek to transform observed data into a physical parameter, namely to generate a model of the earth, in order to determine the geological structure of the subsurface. There are mathematical techniques that allow us to infer these physical parameters, and they are reduced into two known methods: Forward and Inverse modeling. A response, produced by natural or artificial perturbations in the earth, is measured and we will refer as the observed data. The forward modeling consists on solving analytically or numerically a set of theoretical equations for different geophysical problems (electric, gravitational, magnetic, electromagnetic, etc.) to generate, for given model parameters, a synthetic response that suits the observed data. Instead, roughly speaking, the inversion modeling is the reverse problem; it starts with the observed data and it determines estimates of the model parameters (Gadallah and Fisher, 2008). The inverse modelling will be discussed in Chapter 4.

Key (2009) DIPOLE1D forward modeling code was used to calculate 1D CSEM forward responses; this is the E-field amplitude responses considering two layers of isotropic resistive $\sigma_i$ media. In order to compute the forward responses, we first need to set up all the physical parameters that define our data, which in this case are the water depth and the seawater and seafloor resistivities. Thanks to the bathymetry data provided by Dr. Guillermo Díaz, we estimated the water depth for every transmitter position and defined the first layer as the seawater and the second one as the seafloor.

When we do the forward modeling, as mentioned before, we generate a synthetic response while changing the model parameters, therefore here the model parameters are the electrical resistivity of both seawater and seafloor mediums. Based on the CTD measurements taken over the area, the seawater was considered a stratified layer with its minimum electrical resistivity value on the surface $\sigma_1$ = 0.2 $\Omega m$ and maximum value $\sigma_1$ = 0.3 $\Omega m$ at the bottom. Once the seawater layer was defined, the modeling was executed for five different resistivity values of the seafloor: $\sigma_2$ = [0.3, 1, 3, 10, 30] $\Omega m$ in order to find the best fitting synthetic response against the actual E-field response for every frequency. For example, if we consider one receiver, according to this method, we will have an E-field response for every frequency

employed, where f = [0.5, 1.5, 3.5, 6.5] *Hz* with 0.5 *Hz* as the fundamental frequency. Therefore when we apply the forward modeling, we calculate 5 different responses for every transmitted frequency, depending on the resistivity assigned to the sea-floor. Figure 16 shows the forward modeling estimates for the closest receiver for f = 1.5 Hz.

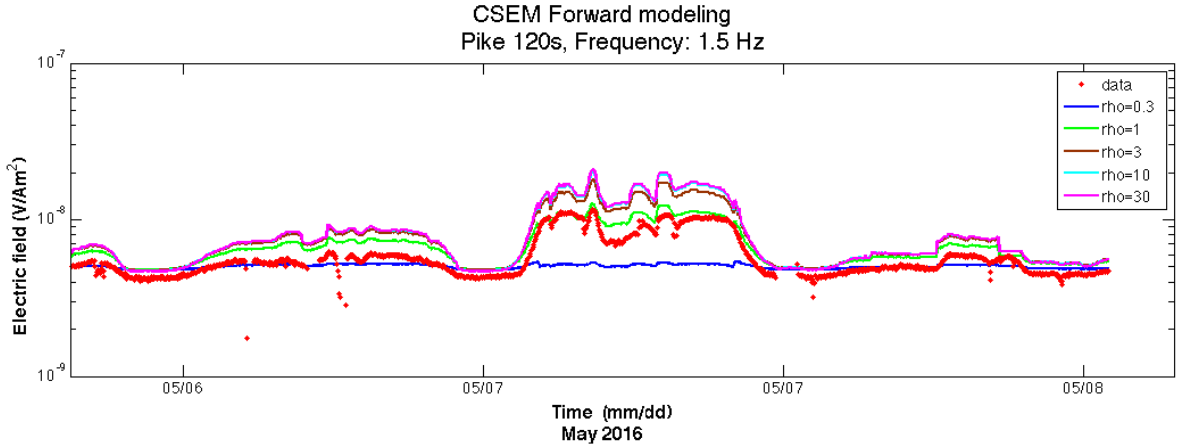


**Figure 16: Forward modeling for the closest instrument at 1.5 Hz. Electrical field (V/Am$^2$) vs. Time (mm/dd), 12 hours between tick marks.**

Moreover, seawater resistivity plays an important role in the forward model, this is because the towing system is in the surface of the ocean, and since the electrical current travels beneath it, its resistance will define if the E-field travels easier or not through it. The higher the resistivity the less damping the signal will suffer, therefore for more resistive bodies the amplitude values of the E-field will be higher. Although we computed many trials, we observed that changing the seawater resistivity value made the forward model responses differed substantially from the observed data; therefore the seawater layer was defined as another parameter to estimate through the inverse modeling.

### 3.4.1. Pseudo sections Results

With the forward responses we calculated the best fitting seafloor value by computing an interpolation between all the synthetic responses, and if the observed response was between the interpolated ranges, the corresponding resistivity values of the seafloor were extracted to

form apparent resistivity profiles called pseudo-sections. To better understand the technique, let's remember the measurements are continuously recorded while the ship moves, and the data were stacked into two minute windows, therefore the forward modeling has to be computed for every data point (i.e. every two minutes measurement); thus, in Figure 17 is displayed, for one measurement, the computed forward responses using five 5 different seafloor layers, for the frequencies f = [0.5, 1.5, 3.5 6.5] *Hz* for the 4 employed receivers. Inspecting (a) Figure 17 we observe that the data measurements for all the frequencies locate between the 0.3 and 1 $\Omega m$, therefore the interpolation will assign a resistivity value between that ranges in the seafloor.

However, during the modeling we observed that for the highest frequency (6.5 *Hz*) estimated responses were equal using different model parameters. This phenomenon was probably due to the fact that the skin depth in sea water for the highest frequency is around ~100 m, therefore, independently of the seafloor resistivity value; those frequencies are not seeing this layer.

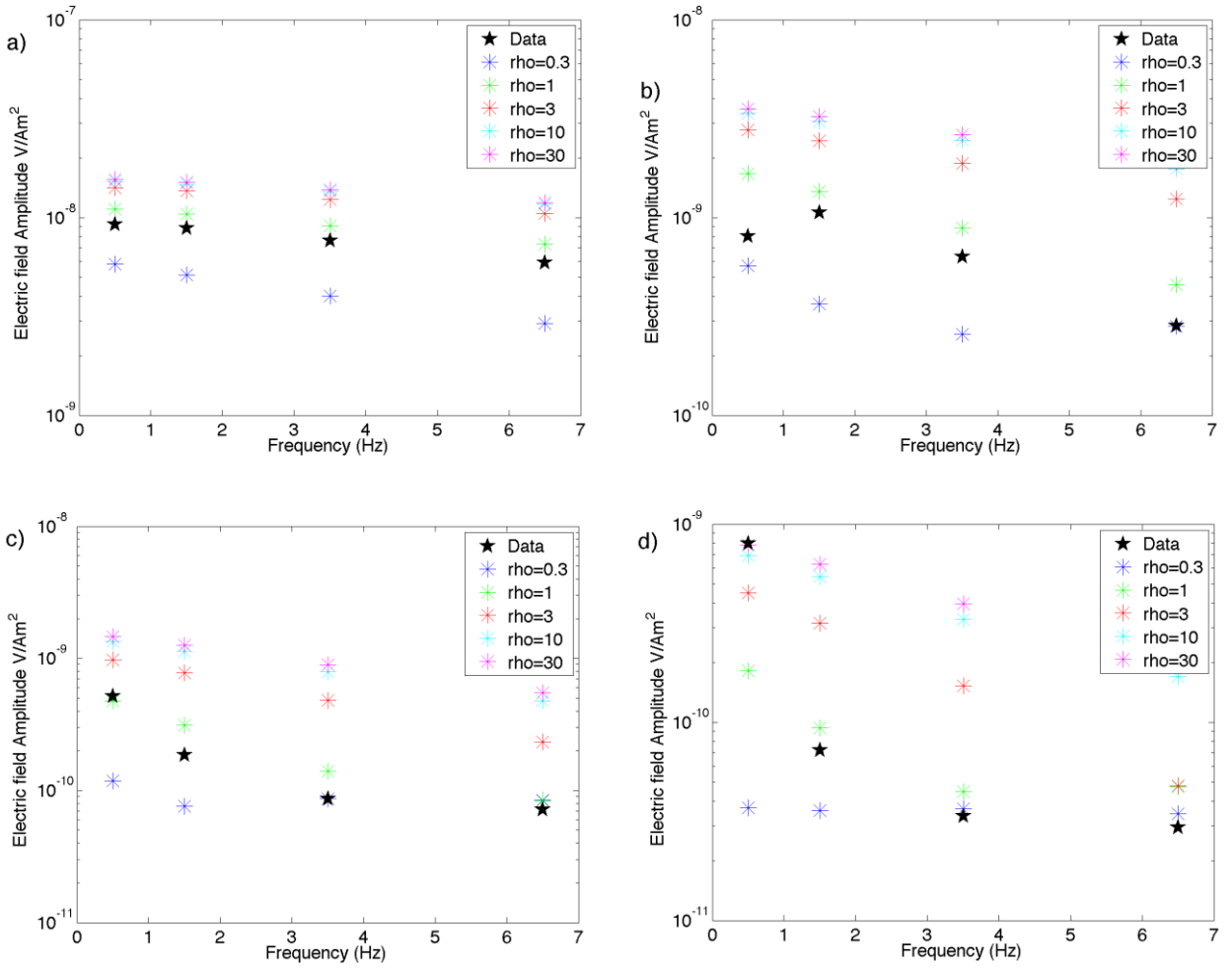


**Figure 17. Computed forward responses using five 5 different resistivity seafloor layers, for the frequencies f = [0.5, 1.5, 3.5 6.5] *Hz* for the 4 employed receivers. The interpolation locates the range at where the seafloor layer might measure for each employed frequency.**

Figures 18 and 19 display the calculated pseudo sections, we will refer as the closest receiver instrument as the first one and the third as the farthest one from the transmitter. The obtained pseudo-sections for the first and second receivers display a conductive body over the Wagner and Consag basins, which correlates resistively with the presence of active faults over the area, however this result can also be associated to the depth of the water columns found in the basins that will impact on the decrease of the measured E-field signals. These results indicate low resistivity areas, which match the high density of faults found over the area, however these are preliminary results and the inversion modelling will find the best fitting model.

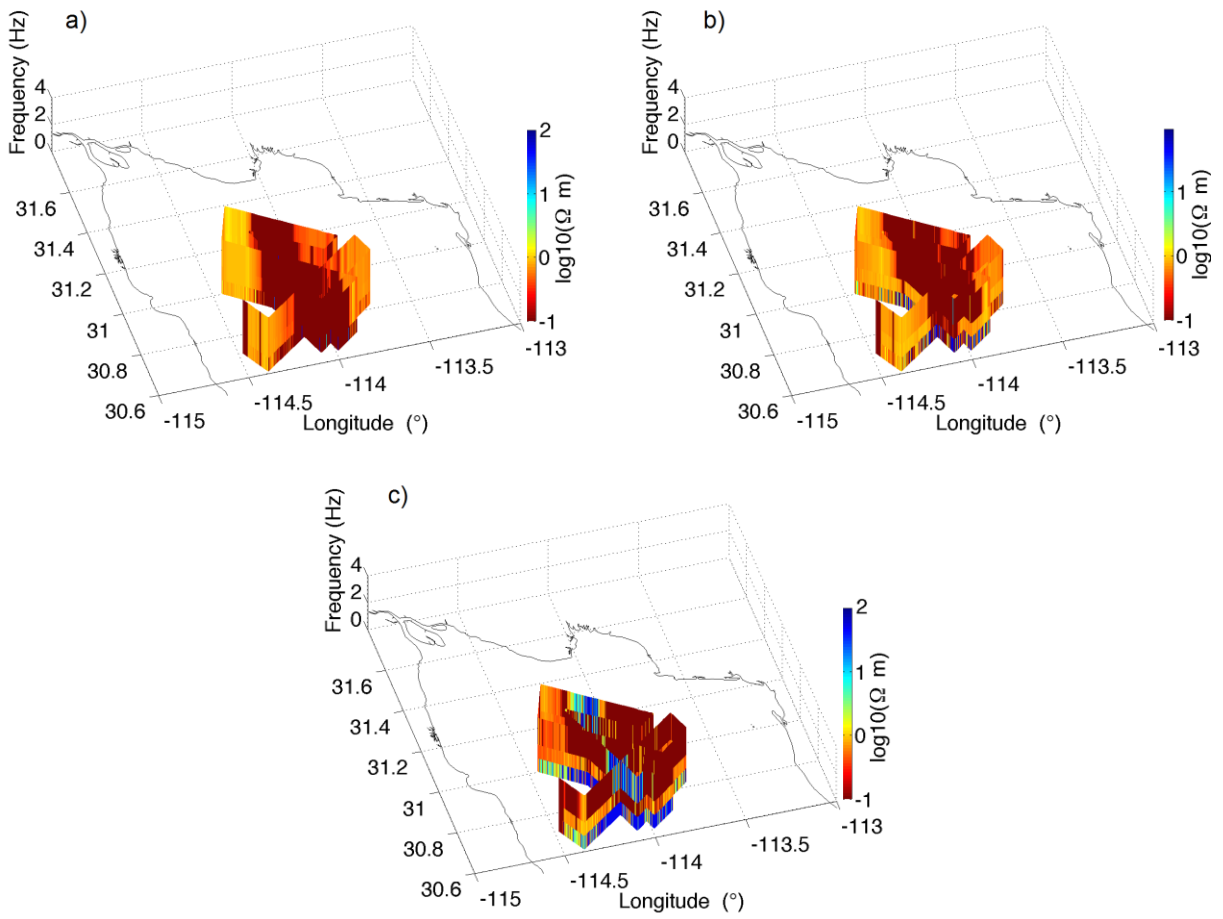


**Figure 18: Calculated Pseudo sections using frequencies of [0.5, 1.5, 3.5] Hz for the first leg of the survey. Results for the (a) first (b) second (c) third closest receiver. Due to the transmitter-receiver separation distance the closest receiver (a) has the lowest penetration depth. Highest frequencies are plotted first, in the vertical scale since penetrate the less too.**

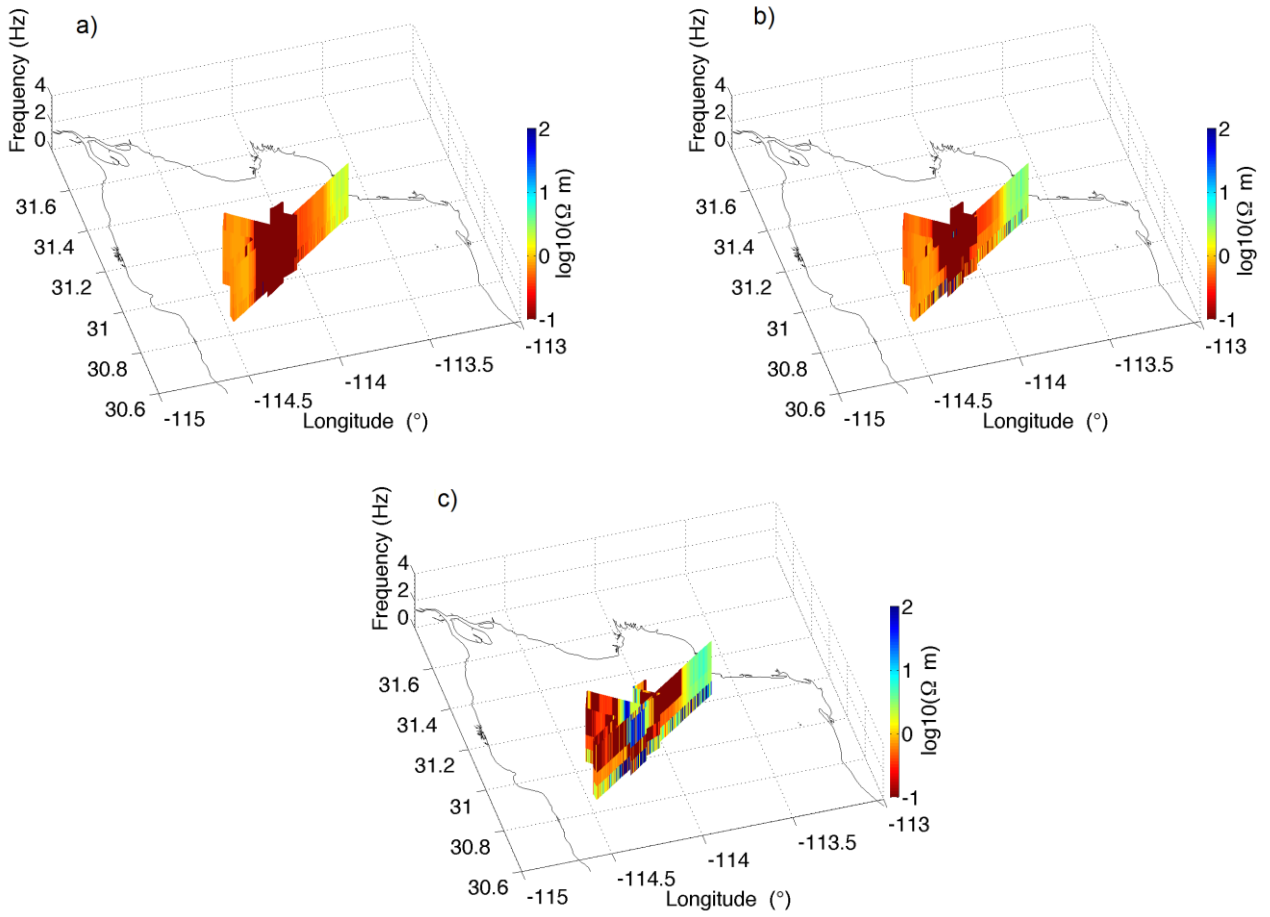


**Figure 19: Calculated Pseudo sections using frequencies of [0.5, 1.5, 3.5] Hz for the second leg of the survey. Results for the (a) first (b) second (c) third closest receiver. Due to the transmitter-receiver separation distance the closest receiver (a) has the lowest penetration depth. Highest frequencies are plotted first, in the vertical scale since penetrate the less too.**

# Chapter 4. Inversion of CSEM data

Pseudo-section as the ones presented in the last chapter are a meaningful representation of the data. However, the best way to obtain information from a given set of geophysical data is through inverse modelling; inversion is the process of finding a model that is compatible with all the observed data. In our experiment, this will help us find a subsurface's conductivity model that satisfies the measured E-field responses; however, since the data set is finite and imprecise, an infinite number of solutions may fit the observed data (Key, 2009). Moreover, although the inverse problem can be seen as the opposite of the forward modelling, in order to implement it, an iterative process has to start using the forward calculation, then the inversion algorithm can be applied so the misfit between the synthetic response and the measured data is reduced.

Different inversion algorithms have been developed over the years; theory and explanation of inversion methods can be found in Zhdanov (2015). In our case, we used the electromagnetic MARE2DEM software developed by Key and Ovall (2011) which implements the Occam's inversion algorithm published by Constable *et al.*, (1987). In the following section a brief overview of Occam's inversion theory is presented.

## 4.1. Occam's Inversion general theory

Constable *et al.,* (1987) presented an inversion algorithm to find the smoothest model that fits the MT and 1D resistivity sounding data, known as the OCCAM's algorithm. Ever since its development, the algorithm has been applied in solving nonlinear electromagnetic geophysical problems and it is based on the regularization of nonlinear inversion problems (Key, 2009; deGroot Hedlin and Constable, 1990). When dealing with geophysical problems there is an infinite number of solutions that will fit the data, depending on the degree of freedom allowed in the inversion. Moreover, the minimum misfit doesn't guarantee finding the best earth model because there could still be non-physical features in the model.

As mentioned before, an important feature in Occam's inversion is the regularization concept. Regularization pursues to reduce any nonphysical features that may arise during the inversion by finding the model that fits the data and at the same time is the smoothest possible. Let us consider first the issue of fitting the data.

When applying modeling inversion, we seek to find the best model that fits the measured data; in other words, find how well a model **m** fits the data we use the misfit calculation:

$$\chi^2 = \sum_{i=1}^{M} \frac{1}{\sigma_i^2} \left[ d_i - f(x_i, \mathbf{m}) \right]^2 \tag{28}$$

where

$$\mathbf{d} = (d_1, d_2, ...., d_M) \tag{29}$$

represent the **M** observed data values, and the independent data variables such as frequency, position, electrode spacing, etc) are given by,

$$\mathbf{x} = (x_1, x_2, ...., x_M) \tag{30}$$

and the model parameters such as layers conductivities, block sizes, etc. are,

$$\mathbf{m} = (m_1, m_2, ...., m_M) \tag{31}$$

Geophysical inverse problems, just like most physical inverse problems, are nonlinear, they have to be linearized expanding $f$ around a starting model $\mathbf{m_0}$.

$$\hat{\mathbf{d}} = f(\mathbf{m_1}) = f(\mathbf{m_0} + \Delta\mathbf{m}) \approx f(\mathbf{m_0}) + \mathbf{J}\Delta\mathbf{m} + O(\Delta\mathbf{m}^2) \tag{32}$$

where $\mathbf{J}$ is a matrix of partial derivatives of data with respect to the model parameters, known as the Jacobian matrix, and its elements represent the best linear approximation of the function $f$ near the point $x_i$,

$$J_{ij} = \frac{\partial f(x_i, \mathbf{m_0})}{\partial m_j} \tag{33}$$

and a model parameter perturbation about $\mathbf{m_0}$

$$\Delta\mathbf{m} = \mathbf{m_1} - \mathbf{m_0} = (\delta m_1, \delta m_2, ..., \delta m_N) \tag{34}$$

the misfit from Equation (28) then can also be written as

$$\chi^2 = \| \mathbf{Wd} - \mathbf{W}f(\mathbf{m_0}) + \mathbf{WJ}\Delta\mathbf{m} \|^2 \tag{35}$$

where $\mathbf{W}$ is a diagonal matrix of reciprocal data errors.

To minimize the misfit $\chi^2$, the derivatives of $\chi^2$ with respect to $\Delta\mathbf{m}$ equal to zero to get N simultaneous equations:

$$\boldsymbol{\beta} = \boldsymbol{\alpha}\Delta\mathbf{m} \tag{36}$$

where

$$\boldsymbol{\beta} = (\mathbf{WJ})^{\mathbf{T}}\mathbf{W}(\mathbf{d} - f(\mathbf{m_0})) \tag{37}$$

and

$$\boldsymbol{\alpha} = (\mathbf{WJ})^{\mathbf{T}}\mathbf{WJ} \tag{38}$$

The system of equation can be solved numerically by the inversion of the matrix $\alpha$, sometimes called the curvature matrix, to find a second model $\mathbf{m_1} = \mathbf{m_0} + \Delta\mathbf{m}$. One approach is to use the least-squares solution. Another approach is the known Occam's inversion algorithm, which adds regularization to the least squares solution, particularly by penalizing the roughness of the model.

Regarding Occam's inversion, the following brief overview of the method has been extracted from Key (2009) work. For a detailed description of the algorithm, please refer to Constable *et al.,* (1987). Occam's inversion, instead of minimizing $\chi^2$, it seeks to minimize the unconstrained functional:

$$U = \| \mathbf{Rm} \|^2 + \mu^{-1} ( \| \mathbf{W(d} - F(\mathbf{m}) \|^2 - \chi_*^2 ) \tag{39}$$

The first term is a norm of the model roughness and is computed by applying a differencing operator to the elements of the model vector **m**, where $\mathbf{R}$ is taken as a matrix of first-differences consisting of (-1,1) entries on the diagonal so that $\mathbf{Rm}$ approximates the vertical derivative of $\log_{10} \rho$. For the models considered in our project, **m** is a vector of $\log_{10} \rho$, $\rho$ = electrical resistivity) for each given layer, that is, having logarithm scales makes sure that the resistivity remains positive during the inversion. Minimizing *U* has the effect of minimizing model roughness depending on how far is the data misfit from being acceptable. We substitute our linearization around the starting model $\mathbf{m_0}$:

$$U = \|\mathbf{Rm}\|^2 + \|\mathbf{P(m - m}_*)\|^2 + \mu^{-1} ( \| \mathbf{W(d} - F(\mathbf{m}) \|^2 - \chi_*^2 ) \tag{40}$$

If jumps in resistivity are desired at certain depths, the corresponding elements of $\mathbf{R}$ can be set to zero and we refer to this as roughness penalty cut, where this option was taken into account in our computed inversions. The second term is a measure of the difference of **m** from an a priori preference model $\mathbf{m}_*$. The diagonal matrix **P** contains scaling parameters that determine the relative weighting between the preference and the model roughness. Preference model values, if used at all, are typically desired for an only few model layers and the

corresponding diagonal elements of **P** will be nonzero. The roughness and preference terms in the above equation are regularizes that serve to stabilize the inversion and keep it from producing wildly oscillating resistivity artifacts.

The third term is a measure of the misfit of the model's forward response $F(\mathbf{m})$ (in our case, the electric field for model m) to the data d. $\mathbf{W}$ is a data covariance weighting function and is here selected to be a diagonal matrix with elements corresponding to inverse data standard errors. In other words, $\mathbf{W}$ weights the relative contribution of each datum to the misfit based on its uncertainty. Thus, data with large errors are scaled to limit their influence, while data with small errors will have a bigger impact on the misfit budget.

$\chi_*^2$ is the target misfit which is not necessarily the minimum misfit, conversely it is greater than minimum possible but statistically acceptable; therefore minimizing U does not necessarily find the best fitting model, instead finds the smoothest model for a given target misfit. The target misfit $\chi_*^2$ is usually chosen so that the root mean square (RMS) misfit $x_{rms}$ is equal to unity:

$$x_{rms} = \sqrt{\frac{\chi^2}{n}} = \sqrt{\frac{1}{n}\sum_{i=1}^{n}\frac{\left[d_i - f(x_i, \mathbf{m})\right]^2}{s_i^2}} \tag{41}$$

where n is the number of data and $s_i$ is the standard error of the $i$ th datum.

The Lagrange multiplier $\mu$ serves to balance the trade-off between the data fit and the model roughness and model preference. One of the main innovations of the Occam method is the automatic selection of $\mu$.

## 4.2. Model parameterization, MARE2DEM Software

Modeling CSEM data involves solving Maxwell's equations presented in Chapter 2. Analytical solutions on scenarios where the surface structure is described as horizontal stratified layers are not enough to model realistic scenarios. Consequently, numerical methods are used to solve 2D or 3D subsurface models that represent many of the studied geological situations.

One of the numerical approaches for solving boundary value problems of differential equations is the Finite Element (FE) method. In a general way, the method consists on the discretization of the subsurface into a finite number of elements; approximate the governing differential equations for an element; set all elements in the solution region; and solve the obtained system of equations (Tveit, 2014). Therefore, in order to apply Occam's inversion over a region it is necessary the use of domain discretization, that is, discretize the target region into a finite number of sub regions or elements (Weitemeyer, 2008).

MARE2DEM modelling code developed by Key and Ovall (2011) uses a parallel adaptive finite element algorithm to calculate rapid and accurate simulations of 2D EM problems; it implements unstructured triangular meshes that allow more complex structures to conform the subsurface region and generate reliable EM responses of CSEM data.

The following figure displays the workflow using MARE2DEM software. This software can be freely downloaded from: http://mare2dem.ucsd.edu/.

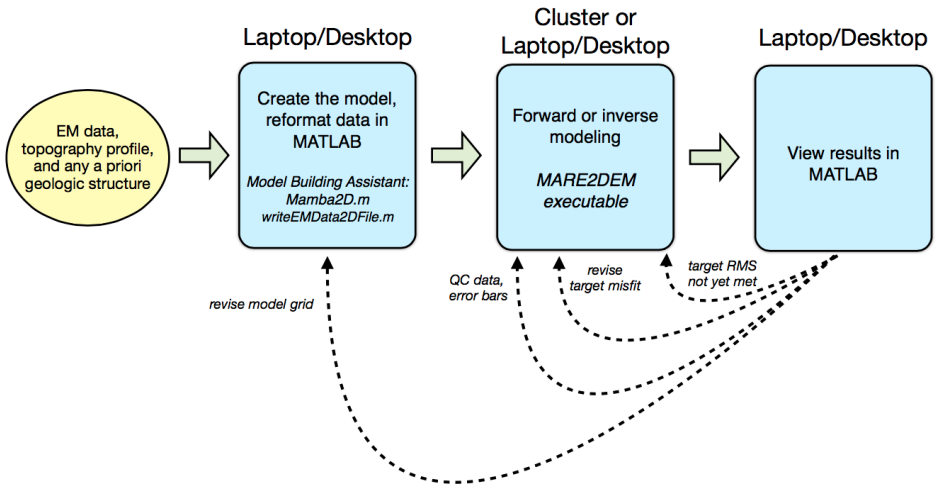


**Figure 20.Overview of MARE2DEM workflow for forward and inverse modelling. Reproduced from: *http://mare2dem.ucsd.edu/?tag=workflow*.**

1. Prepare the EM data, topography or bathymetry profile and any *a priori* geologic information of your model.

2. Create the model domain using the MATLAB code Mamba2D and create the data file with the format required by MARE2DEM.

3. Run MARE2DEM on your laptop, desktop or cluster.

4. View the results on your laptop or desktop using the tools found on the mentioned source. Model responses (as well as data) can be viewed to compare the model responses vs. the acquired data. After comparing the results you can modify the starting model and recomputed results, or you may want to eliminate some noisy data.

### 4.2.1. Inversion Model

Prior running MARE2DEM software, MAMBA2D Model Building Assistant is an interface used to create the 2D models to forward and inverse modelling; it uses unstructured polygons and

allows the integration of complicated structures such as topography and as indicated in the workflow diagram, the first step is to create the model using MAMBA2D.

MARE2DEM has lots of options (anisotropy, roughness penalty cut, prejudices, size of elements, etc.) to modify the starting model, however it is recommended that the starting model be as simple as possible so the inversion finds the smoothest model that fits the data under these circumstances. Then the features of the model can be modified in accordance to any a priori geologic information known of the area of study.

To illustrate the procedure the following exemplifies the steps used to invert the survey line LAH-1. First, we need to create the model grid using MAMBA2D; some of the special features of the program are that it allows importing topography, or in this case, the bathymetry profile for the line of interest. Therefore, the bathymetry was included into the model grid as seen in Figure 20. Also, the layers of seawater and seafloor were meshed and set as free parameters. Regarding the discretization of the model, we parameterized using large triangles for deep depths and small triangles for CSEM near and below the surface (Figure 21). The limit between the seawater and seafloor layers is defined by the bathymetry and in terms of inverting the subsurface, we allowed the presence of large gradients across the bathymetry boundary; this can be done by removing the inversion roughness penalty which will allow sharper features to develop across the line segments.

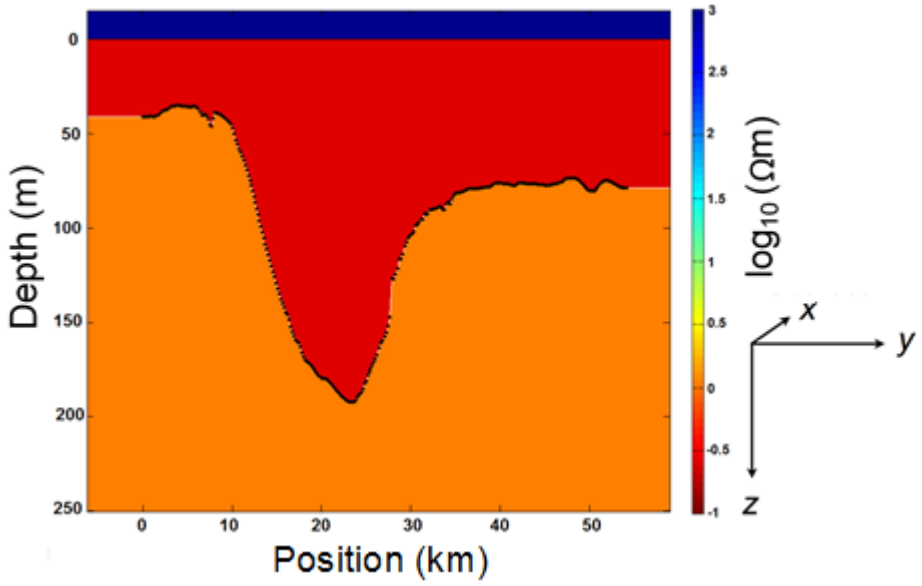


**Figure 21: Preliminary Inversion model using MAMBA2D for CSEM line LAH-1 which includes the bathymetry profile. Note the white limit between the seawater and seafloor layers represent where the inversion roughness penalty was removed, this allows sharper features to develop across the line segments.**

Another important characteristic is that MARE2DEM handles isotropic or anisotropy conductivity. For this section we considered a vertically anisotropic model, which means that $\sigma_x$ and $\sigma_y$ are equal and different from $\sigma_z$, with the axis z measured positive downwards.

Since all the finite element meshing and adaptive refinements are executed on MARE2DEM code, once the grid of parameters are ready, the next step is to run MARE2DEM. After computing two iterations the minimum misfit was reached and the results are displayed in Figure 22. Additionally, Figure 23 shows the data and the solution model responses; further details of the results are covered in Chapter 5.

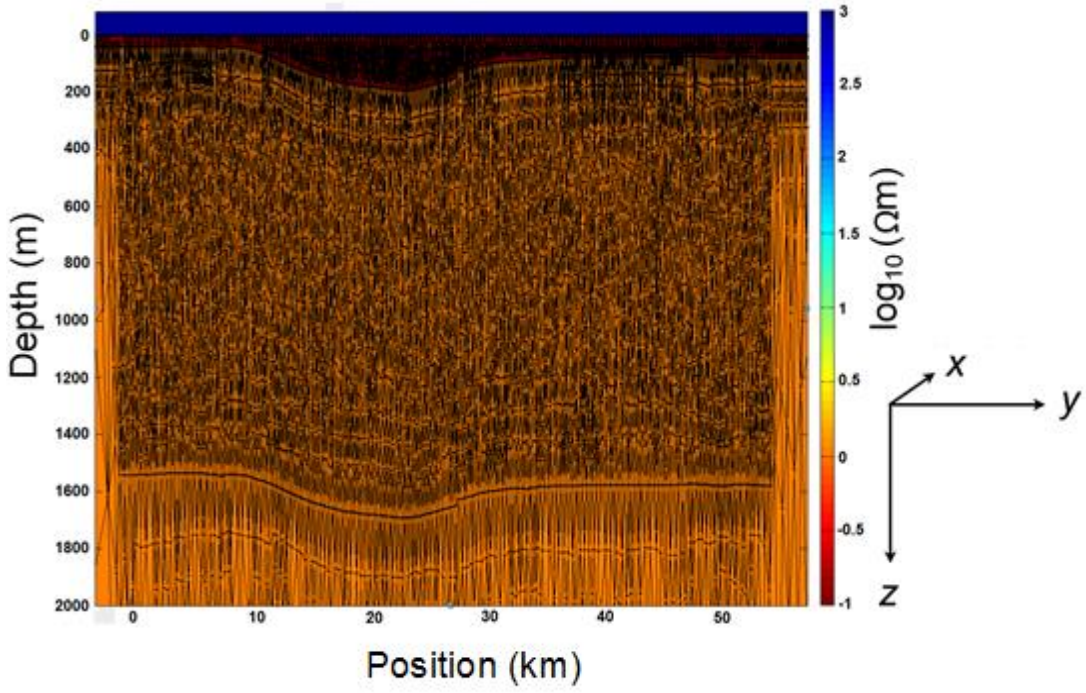


**Figure 22: Inversion model grid created using MAMBA2D for CSEM line LAH-1. Seawater and seafloor layers are meshed into triangles for the inversion, where the parameterization consists on using large triangles for deep depths and small triangles for near and below surface imaging. To carry the inversion, in the first model the seawater conductivity was set to $\sigma_1 = 0.25\Omega m$ and the seafloor $\sigma_2 = 1\Omega m$.**

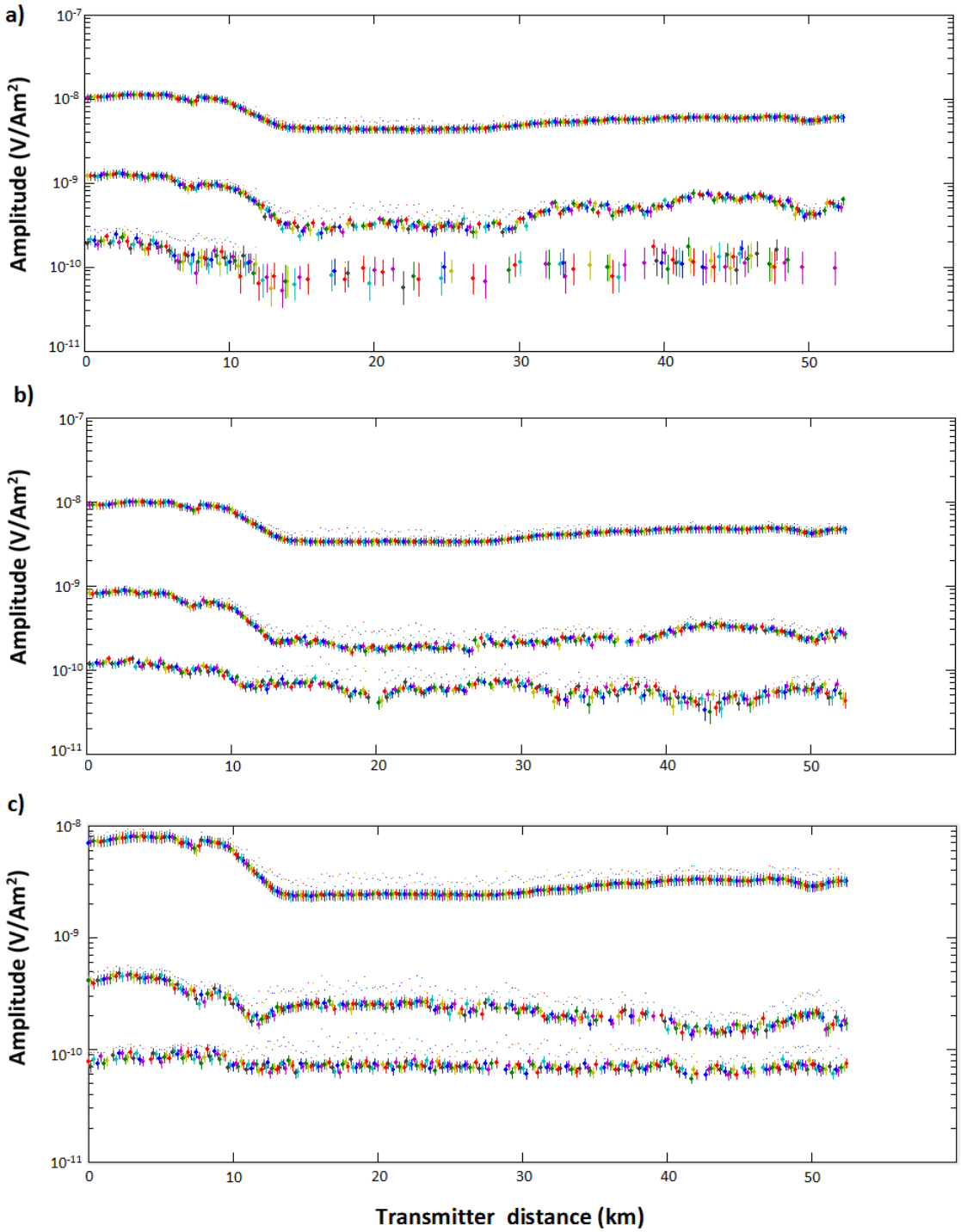


**Figure 23: Model responses (dots) and measured data (dots with error bars) for the three closest instruments for the frequencies 1.5, 3.5 and 6.5 Hz. (a) plot of the model responses and measured data by the three closest receivers for the frequency of 1.5 Hz, (b) 3.5 Hz and (c) 6.5 Hz. The higher amplitudes are measured by the closest instrument, while the smallest ones by the farthest one.**

Applying the inversion modeling as mentioned before, seeks to find the best fitting model, so different trials changing the features of the model may have to be undertaken in order to produce a more geologically satisfying model, so the above may be repeated making the necessary considerations.

### 4.2.2. Data uncertainty

Although the acquired CSEM data may not reach the threshold of quality, based on practical estimates of the statistical noise limit, we set our minimum error floor as 10% of the amplitude responses. Since the data is in logarithm scale, the following calculation is employed to determine the error floors as percentages given that CSEM amplitudes can vary many orders of magnitude (Key, 2009).

Simple uncertainty analysis based on Taylor series, assumes that the uncertainty of a function $\Delta f(x)$ by a given uncertainty$\Delta x$, when $\Delta x \ll x$, is approximately

$$\Delta f(x) \approx \frac{d f(x)}{d x} \Delta x \tag{43}$$

To represent the uncertainty correctly in a logarithm scale, $f(x) = \ln(x)$, and since

$$\frac{d \ln(x)}{dx} = \frac{1}{x} \tag{44}$$

The uncertainty would be

$$\Delta \ln(x) \approx \frac{\Delta x}{x} \tag{45}$$

For arbitrary logarithms we can use the change of the logarithm base

$$\log_b(x) = \frac{\ln x}{\ln b} \tag{46}$$

Substituting Equation (45) on Equation (46),

$$\Delta \log_b(x) \approx \frac{\Delta x}{x \ln b}$$

$$\Delta \log_{10}(x) \approx \frac{\Delta x}{x \ln(10)} \approx 0.4343 \frac{\Delta x}{x} \tag{47}$$

The values of uncertainty in CSEM data are typically associated with the errors in the position and orientation of receivers and transmitter. However, data are also limited by environmental noise. On the measurements, the noise was greater for the highest frequency (6.5 *Hz*), nevertheless we encountered high fluctuations in the fundamental frequency 0.5 *Hz* amplitude values; hence, this frequency had to be discarded.

If the data uncertainty is well known the model RMS misfit can be close to 1.0, however if the model fits to better than 1.0, this could mean that either the model is fitting noise or the data uncertainty is too large.

And even though we are inverting multiple frequencies, future work can be done incorporating the phase component in the inversions.

# Chapter 5. Results

## 5.1 Resistivity models

Although the CSEM measurements were continuously obtained in relation to the path followed by the ship, nine profile lines were selected for the inversion models avoiding turns and bad quality data. The lines LAH-1, LAH-2, LAH-3, LAH-4 and LAH-5 were measured during the first leg whereas the rest were measured during the second leg of the survey (Figure 24).

In Figure 25 we show the obtained resistivity distribution over the study area. Isotropic electrical conductivity was assumed in the profiles: LAH-3, LAH-4, LAH-5, LAH-8 and LAH-9, whereas anisotropy was assumed in the profiles LAH-1, LAH-2, LAH-6 and LAH-7. The fact that on some models we consider anisotropy is because the isotropic model didn't adjust the data response properly, and after implementing the anisotropy this was accomplished with better results.

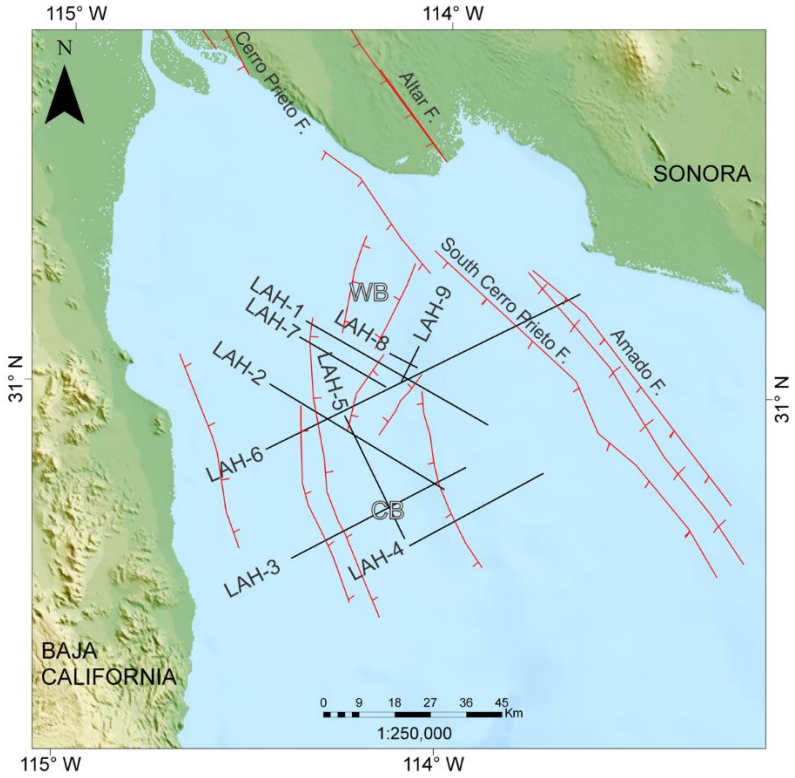


**Figure 24. CSEM inverted profiles (LAH=Line Alpha Helix), WB: Wagner Basin, CB: Consag Basin. Faults system reported in Martín-Barajas, *et al.,* (2013).**

Having a transverse anisotropic model in the z direction means the electrical conductivity tensor has $\sigma_x = \sigma_y$ and different from $\sigma_z$, however the results show resistivity $\rho_i$ (reciprocal of conductivity) instead of conductivity. Therefore, the inversion will create two variables: $\rho_{\parallel}$ and $\rho_{\perp}$ which are the horizontal ($\rho_y$) and vertical ($\rho_z$) resistivities respectively. As explained in Constable, *et al.,* (2015), if the data can't constrain the amount of anisotropy, two independent models will be created to fit the data with minimal regularization cost. Nevertheless, one way to constrain the anisotropy is by implementing an additional parameter in Equation 40 that adds a regularization penalty between the two calculated resistivities. Based on their results, using a relatively weak penalty of 0.1 produced largely independent vertical and horizontal resistivities, whereas for a relative weight of 10 the inversion retrieved the isotropic model leaving the anisotropy feature unused. As for a relative penalty of 1.0 the results were suitable giving a more reliable geological approach. It is important to understand that these three cases fit the data equally, and choosing a model involves carefully reviewing any a priori known geologic information, examining the quality of the data and applying any data constrains known of the study area. Hence, for this project the anisotropic inversion modelling was calculated using 0.1 and 1.0 of penalty weight.

The presented results are based on the comparison between the results obtained with two cases: (a) resistivity results considering relative penalty of 0.1 and results using a penalty of 1.0 described in this section and their correlation with other geophysical results: (b) Heat flow measurements discussed in section 5.2 and (c) 2D seismic reflection profiles discussed in section 5.3.

The obtained inversion results of the electrical resistivity distribution for both directions (-*y*- and -*z*-) using the two different penalty weights (0.1 and 1.0) are plotted in Figures 25 and 26 in order to visualize and compare how the results differ from each other. As shown by Persaud *et al.,* (2003), there is a thick pile of sediments accumulated from the Colorado River over the Wagner and Consag basins; furthermore, the electrical resistivity for marine sediments is between 1-10 $\Omega m$. The plots in Figure 25 and 26 indicate the presence of marine sediments (as expected) with resistivities around 1$\Omega m$ in the SE section; but in some areas lower resistivity

values (around 0.3 $\Omega m$) are found. However there are differences between the model responses using the 0.1 and 1.0 anisotropy penalty weight. By inspecting the resistivity in the $-y-$ direction in Figure 25, a resistive body is found in the eastern side of the Wagner basin. Conversely, in Figure 26 (using anisotropy penalty weight of 1.0) the same section shows resistivity values around 3-10 $\Omega m$, unlike the ~30 $\Omega m$ found in Figure 25. Moreover, in Figure 26 we note the anisotropy feature vanished giving almost the same inversion models for both directions. This arises into the question of which model could be the most accepted, and even though the results using 0.1 penalty weight has RMS misfit are in general lower than misfit obtained in the other models, however is possible using a low penalty produces overfitting giving non-geological model responses due to the independency between them $\rho_y$ and $\rho_z$.

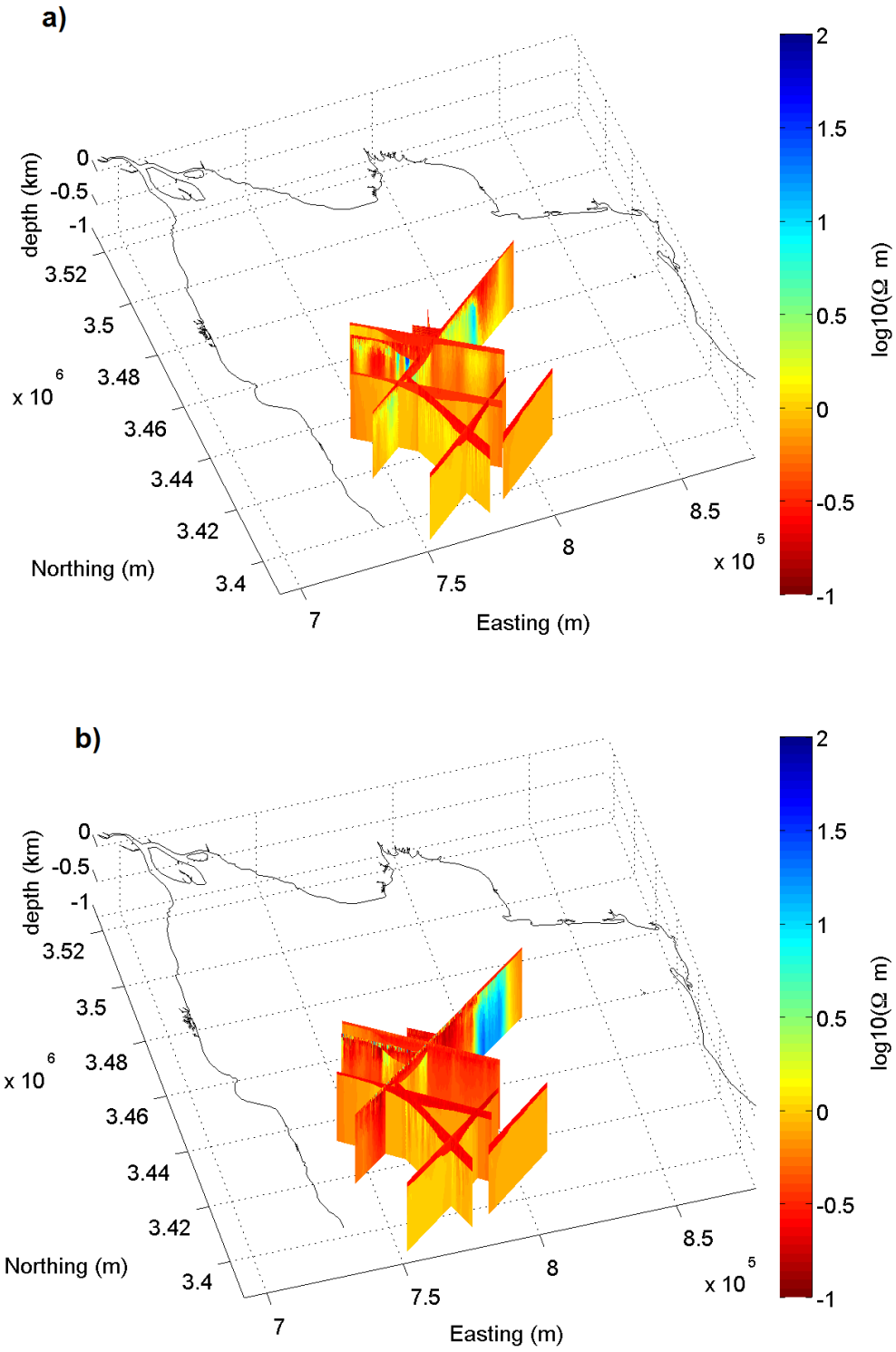


**Figure 25. 2D Inversion models distribution, using anisotropic penalty weight of 0.1, from CSEM collected data at the NGC. LAH-3, LAH-4, LAH-5, LAH-8, LAH-9 are Isotropic models; LAH-1, LAH-2, LAH-6, LAH-7 are anisotropic models. a) Represents the vertical resistivity values $\rho_z$, b) represents the horizontal resistivity values $\rho_y$.**

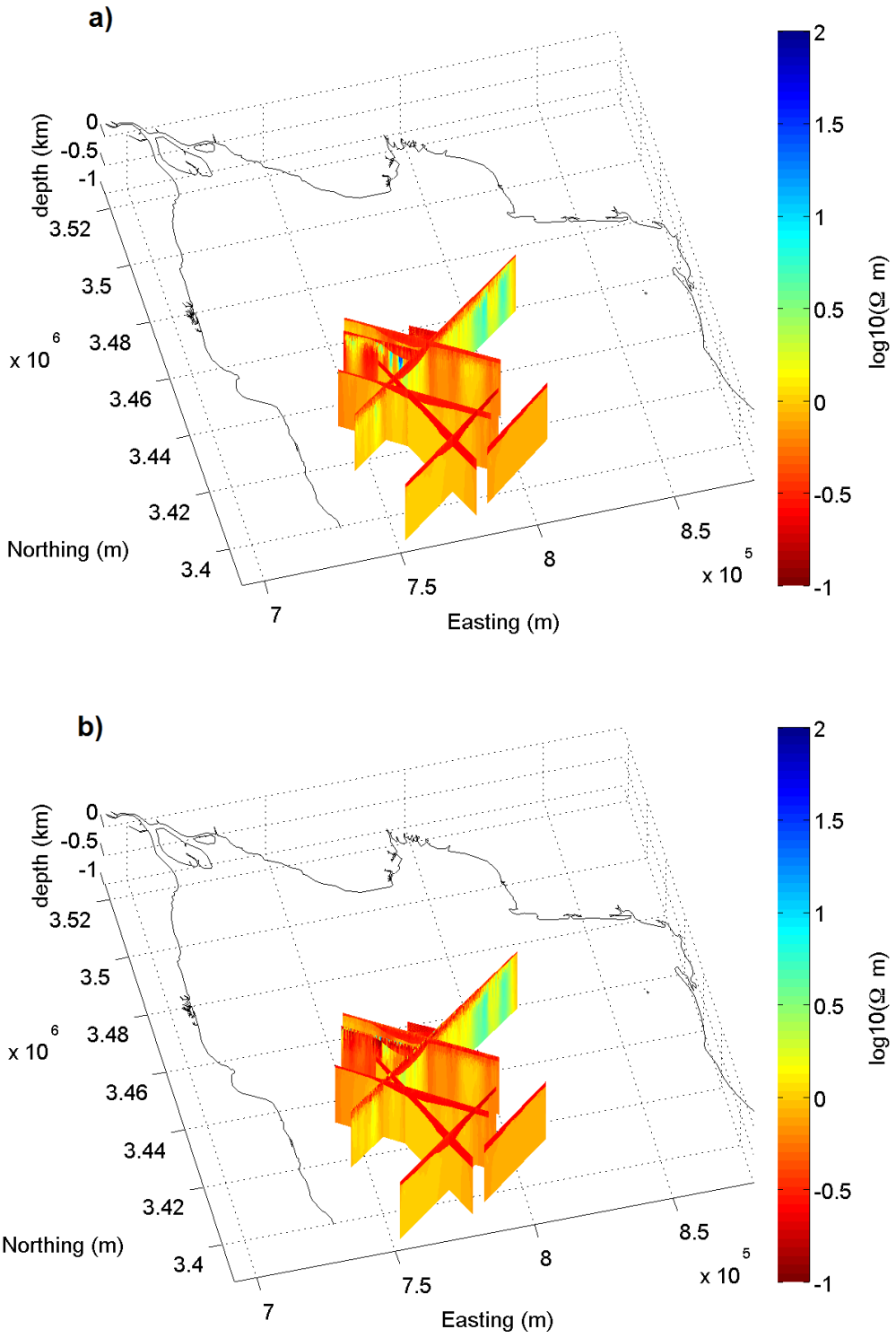


**Figure 26. 2D Inversion models distribution, using anisotropic penalty weight of 1.0, from the CSEM collected data at the NGC. LAH-3, LAH-4, LAH-5, LAH-8, LAH-9 are Isotropic models; LAH-1, LAH-2, LAH-6, LAH-7 are anisotropic models. a) Represents the vertical resistivity values $\rho_z$, b) represents the horizontal resistivity values $\rho_y$.**

## 5.2 Correlation with heat flow anomalies

Prol-Ledesma *et al.,* (2013) reported heat flow measurements taken over the study area and heat flow transport anomalies were found mainly over the Wagner and Wagner Sur faults. To interpret the results from Figure 25 and 26, slices of the resistivity values considering all the CSEM profiles (shown in Figure 24) were extracted in order to produce contour images for three depths: z= [300, 500, 1000] *m*, using the 'natural' interpolation from MATLAB's contour function. Likewise, using the heat flow reported values, a contour map was also plotted in order to visualize and compare the heat flow and electrical resistivity distribution over the area.

Since using 0.1 penalty in the anisotropic model gave almost two independent values for the resistivity in the $y$ and $z$ direction, the contour maps were computed for both of them (Figures 28 and 27), while for the 1.0 penalty inversion results gave almost the same model, only one contour plot was calculated (Figure 29).

Based on the heat flow and resistivity distribution maps plotted in Figures 27 and 28, possible high heat flow values may be present in other sectors of the study area, which are identified as low resistivity data (red color). However, in Figure 29 the low resistivity values are only low resistivity where the highest heat flow magnitudes were found. This fairly close correspondence in both cases is encouraging since this opens the possibility that the surface towed CSEM method applied on depths < 250 *m* can accurately locate lower resistive anomalies which can be associated to higher temperatures values.

Due to the fact that this is the first time the CSEM method has been used to target marine hydrothermal sources, further heat flow studies to complement these results can corroborate the found positive correlation and validate this method as a reliable option on targeting high heat flow anomalies.

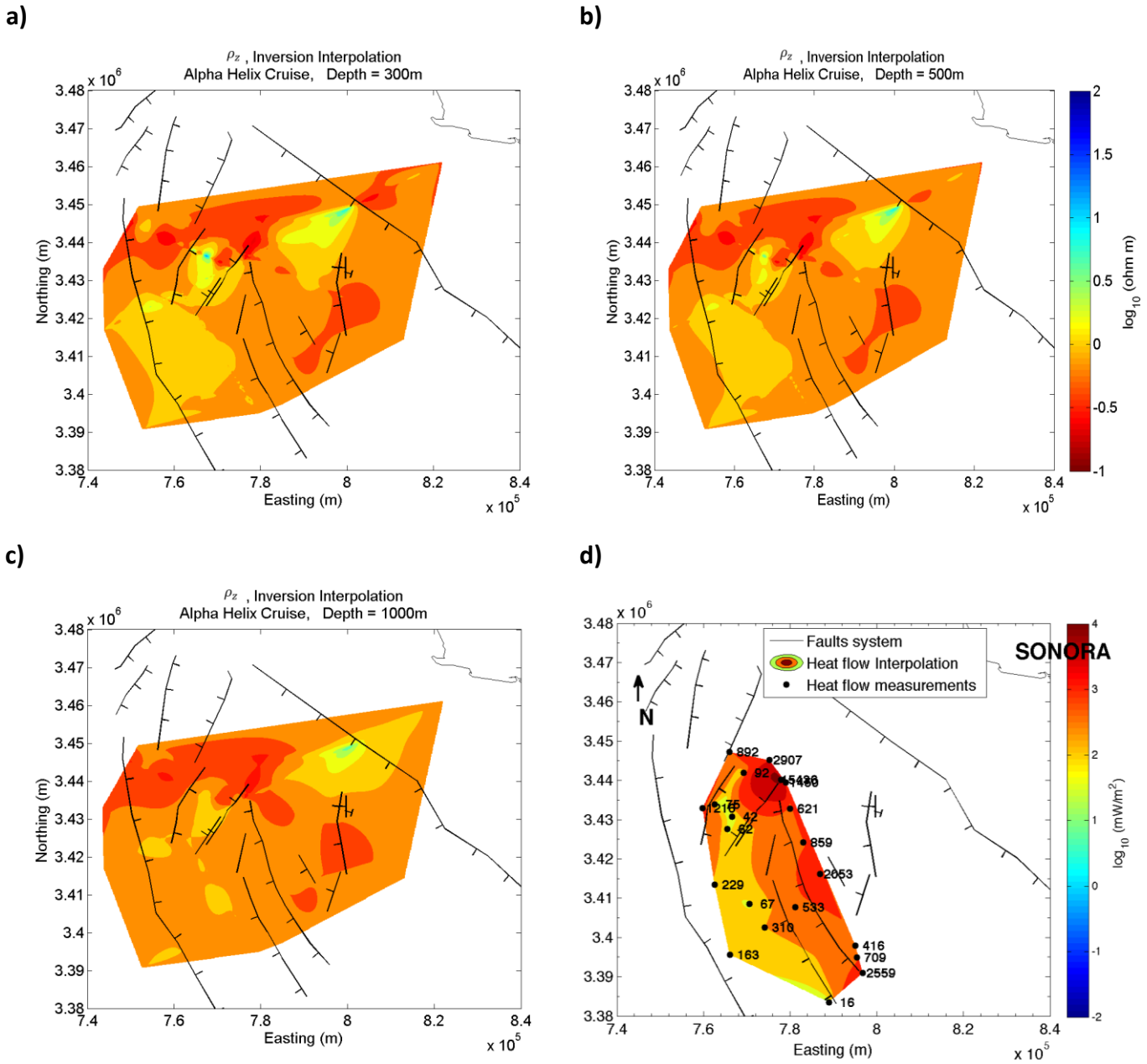


**Figure 27. Vertical resistivity ( $\rho_z$ ) Inversion model interpolation using anisotropic penalty weight of 0.1. Plotted slices for depths of (a) 300, (b) 500 and (c) 1000 m, (d) shows the heat flow measurements interpolated reported by Prol-Ledesma *et al.,* (2013).**

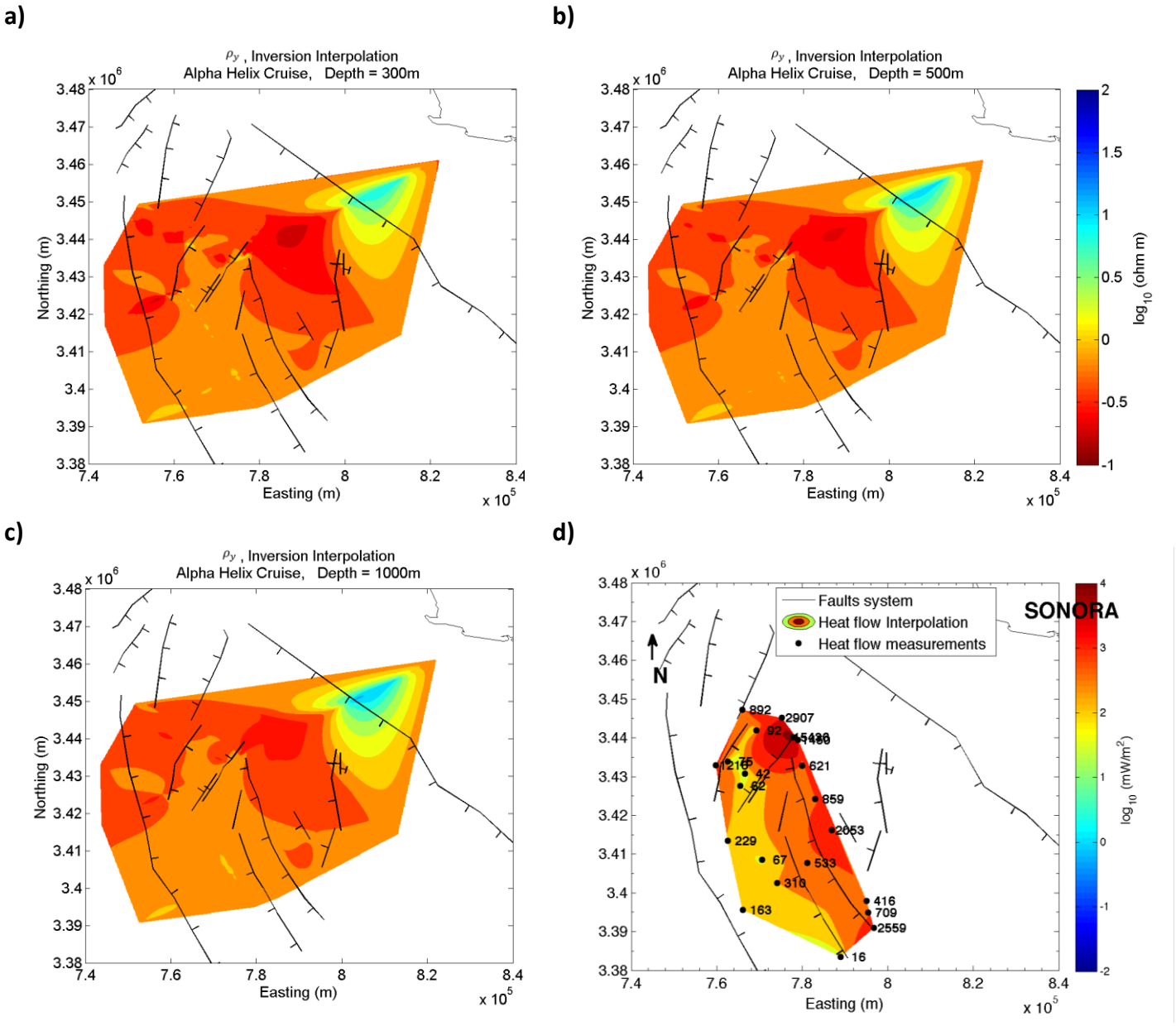


**Figure 28. Horizontal resistivity ( $\rho_y$ ) Inversion model interpolation using anisotropic penalty weight of 0.1. Plotted slices for depths of (a) 300, (b) 500 and (c) 1000 m, (d) shows the heat flow measurements interpolated reported by Prol-Ledesma *et al.,* (2013).**

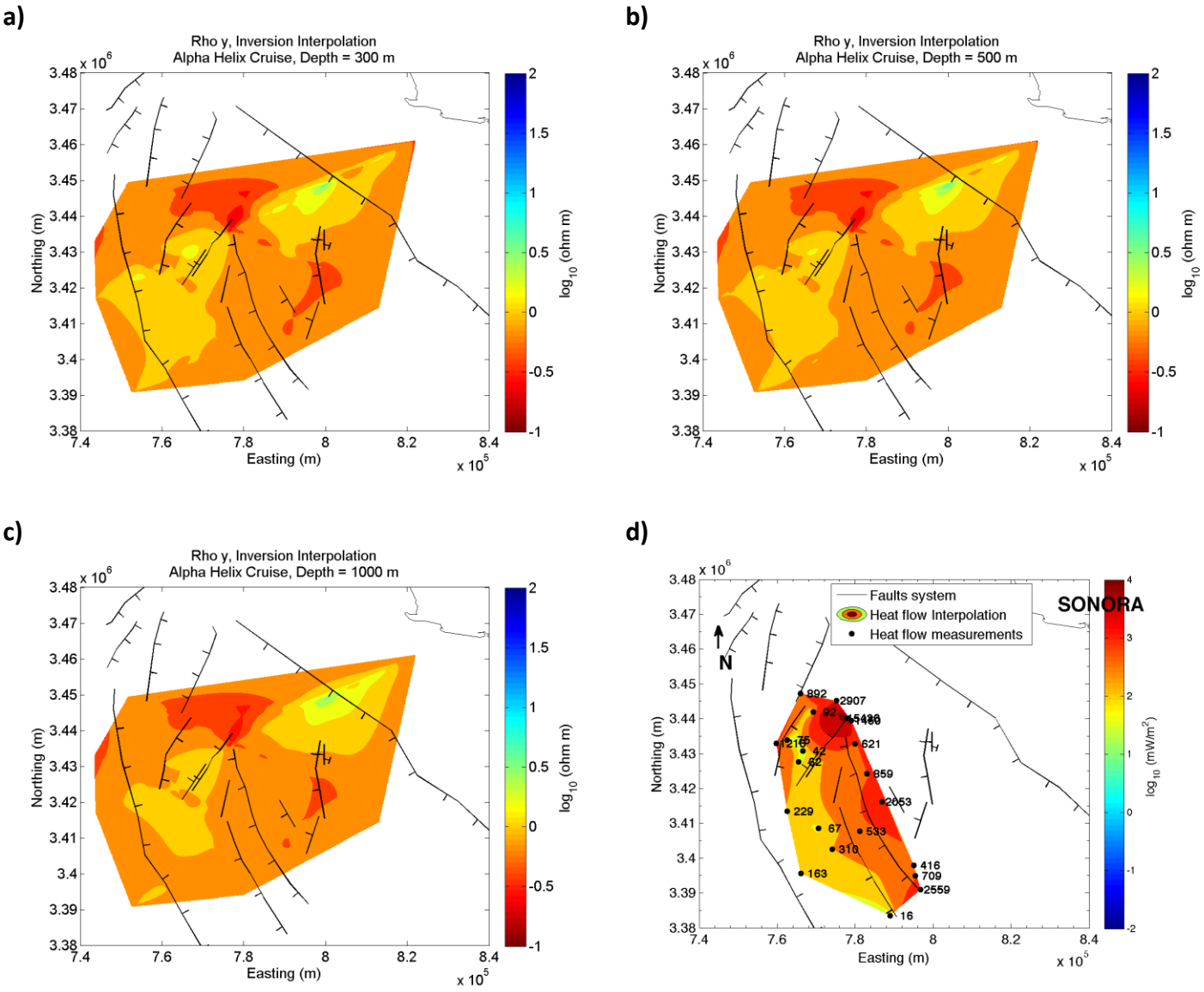


**Figure 29. Horizontal resistivity ( $\rho_y$ ) Inversion model interpolation using anisotropic penalty weight of 1.0. Plotted slices for depths of (a) 300, (b) 500 and (c) 1000 m, (d) shows the heat flow measurements interpolated reported by Prol-Ledesma *et al.,* (2013).**

## 5.3 Correlation with seismic profiles

CSEM results are hard to interpret on their own, and we have to find an adequate geological model when the results are compared with other acquired data; for example here we compare heat flow measurements reported by Prol-Ledesma *et al.,* (2013) and 2D multichannel seismic reflection data from two surveys: Ulloa in 1999 and Petróleos Mexicanos (PEMEX) in 1979-1980, provided by Dr. Arturo Martín Barajas and Dr. Mario Gonzalez and also, with the great help of MCs. Martín Pacheco from CICESE we've compared the CSEM inversion models of 3 profiles that match the locations with the already interpreted seismic sections.

As mentioned before, the CSEM results were also compared with 2D seismic reflection data that match the position of three profiles taken with CSEM. The LAH-6 profile is compared with the seismic profile obtained during the 1970's by PEMEX, and the lines LAH-1 and LAH-2 are compared with seismic profiles from Ulloa 1999 Cruise reported on Persaud *et al.,* (2003).

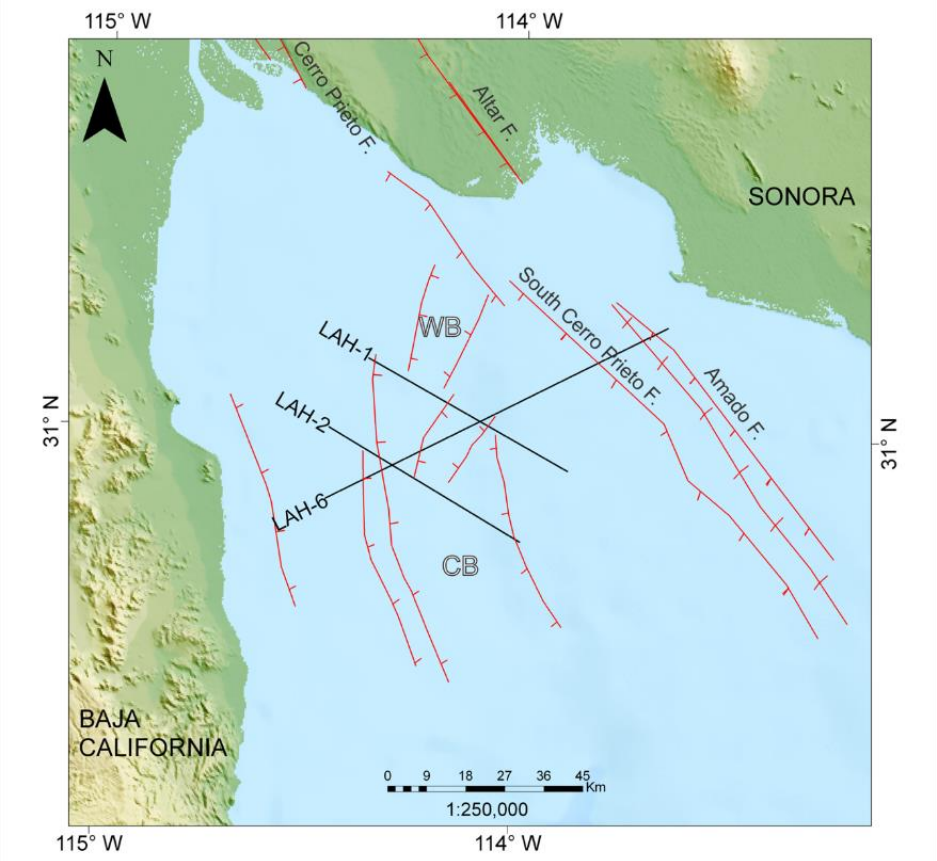


**Figure 30. The CSEM profiles LAH-1, LAH-2 and LAH-6 match with the locations of 2D multi-channel Seismic reflection profiles from Ulloa 1999 data. Only the CSEM profiles are displayed.**

Prol Ledesma *et al.,* (2013) found that the presence of faults on the thick impermeable sediment layer generates permeable zones which allow discharge of fluids where the faults reach the top of the seafloor layer. In the profiles LAH-1 and LAH-2 displayed on Figure 31 and 32 respectively, according to the seismic section from Ulloa 1999, there is a high abundance of faults in both profiles; furthermore most of the faults reach the top of the seafloor layer as seen in Figure 28. However, according to our results, the presence of faults doesn't ensure hydrothermal activity, in despite that the faults generate a permeable ambiance along the sediment layer. This is because even though the lower resistivity areas (associated to a higher temperature values) correlate with the presence of faults in LAH-1 profile (Figure 31), in the profile LAH-2 (Figure 32), the electrical resistivity is approximately homogenous with values around 0.5-1 $\Omega m$ regardless of the number of existing faults.

Additionally, the CSEM is useful on defining lateral resistivity changes. Hence if for example we consider a seafloor conformed by two different resistive bodies positioned horizontally, the CSEM method would identify the resistivity boundary as a decrease or increase of the amplitude of the E-field more abruptly depending which body has lower or higher resistivity. Thus, given the numerous faults in the study area, is possible that the inversion model generates the vertical discontinuities which are defined as lateral resistivity changes. Another important characteristic of the results displayed in Figure 33 is that the vertical exaggeration is really high, and that's another reason why it gives the appearance on being vertical when actually is not.

Having a transversely anisotropic model implies that the achieved result will consist of two electrical conductivities that describe the properties of the media viewed from two different coordinate axis. Depending on the anisotropy penalty weight they can be independent or not. Therefore, recalling Figure 15 from section 4.3.3, after computing the inversion, the model can satisfy two different anisotropy geological structures: either $\rho_{\parallel} > \rho_{\perp}$ or $\rho_{\parallel} < \rho_{\perp}$.

For instance, examining the results on (B) Figure 33, the profile LAH-6 oriented SW-NE display an uncommon set up, that is - in some regions $\rho_{\parallel} > \rho_{\perp}$ and in others is the opposite case. When the inversion was carried out over this profile, the isotropic model didn't adjust the

responses around 60 km offset distance, and after several trials to find the best fitting model, the anisotropic model using a penalty of 0.1 helped on fitting the RMS down to 1.276 and an interesting feature appeared over this part of the section: a resistive body is seen on the $\rho_y$ direction with magnitudes around 30 $\Omega\, m$ at depths of about 500 m. However, in the z direction the body is conductive and it has values of about 0.3 $\Omega m$; this drastic change represents the case where $\rho_{\parallel} < \rho_{\perp}$, where these cases represent horizontally stratified bodies interbedded with higher resistivity bodies. This could mean that the resistive body (i.e. basement) in the y direction is vertically fractured and there is fluid movement that flows through it. Nevertheless, considering that the acoustic basement over that region is found at depths close to 1-1.5 km, and acknowledging that given the Transmitter-Receivers separation distance is less than 1 km, the penetration of the method would be less than that and then resistive body found on the y direction is probably an overfitting artifact.

On the other hand, by inspecting the results on (A) Figure 33 present in the section discussed below, using a penalty 1.0 finds a model that fits the data with RMS=1.8 and locates a body also resistive in comparison with its surroundings (~3-10 $\Omega m$), however the anisotropy feature is not present and the RMS is not as low as the one obtained in (B). Nevertheless, it can be possible the penetration of the method is higher and in fact is sensitive to the acoustic basement found at shallow depths, future work to study with greater detail the sensibility and penetration of the method is advised.

However, a sensitivity study, which is out of the scope for this thesis project, can help to estimate if the method can have sensitivity at depths greater than the 1 km separation distance. If so, this would mean that me method is actually seeing the acoustic basement; however further studies have to be carried on implementing this presented methodology.

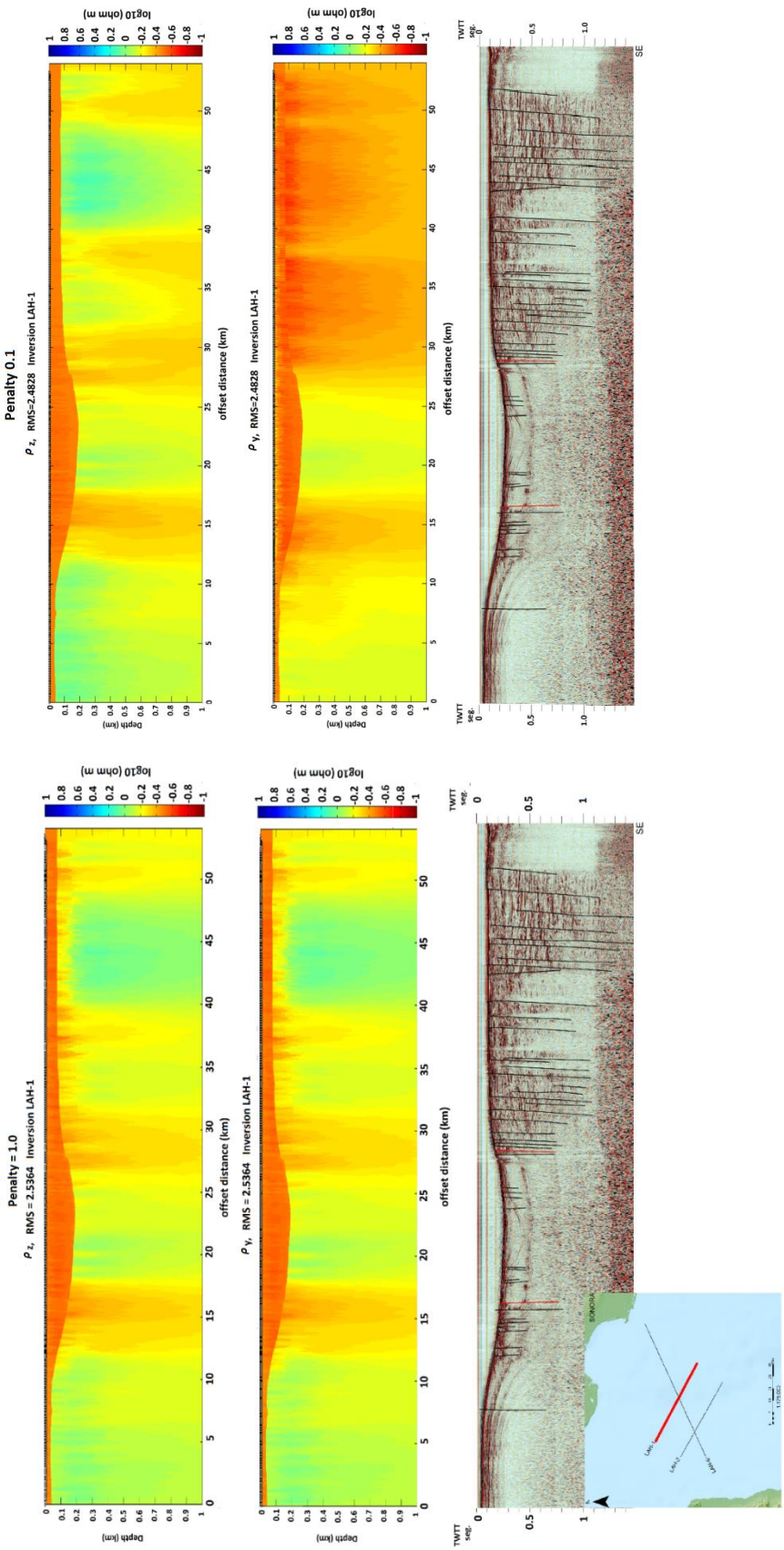


**Figure 31. Comparison between CSEM LAH-1 anisotropic Inversion models using 0.1 and 1.0 anisotropic penalty weight and Ulloa 1999 2D seismic reflection profile. A) Upper and middle images show the vertical ( $\rho_z$ ) and horizontal ( $\rho_y$ ) resistivity vs. offset distance (km) using 0.1 penalty. B) Upper and middle images show the vertical ( $\rho_z$ ) and horizontal ( $\rho_y$ ) resistivity vs. offset distance (km) using 1.0 penalty. Lower image in (A) and (B) shows the 2D seismic profile of Ulloa 99 cruise that matches with the location of LAH-1 profile. NO-SE profile. Red lines represent the main faults, Consag and Wagner faults from left to right.**

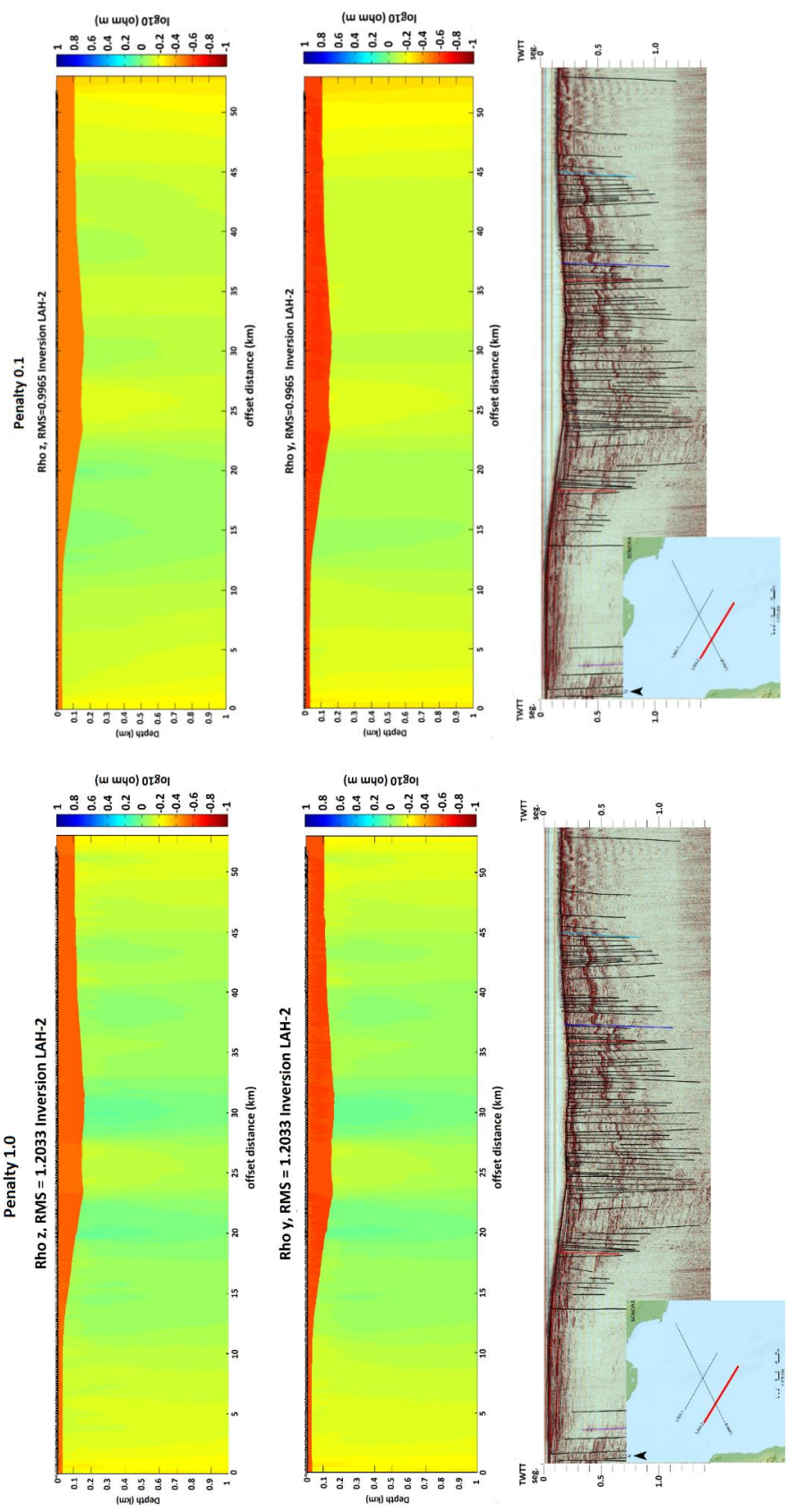


**Figure 32. Comparison between CSEM LAH-2 anisotropic Inversion models using 0.1 and 1.0 anisotropic penalty weight and Ulloa 1999 2D seismic reflection profile. (A) Upper and middle images show the vertical ( $\rho_z$ ) and horizontal ( $\rho_y$ ) resistivity vs. offset distance (km) using 0.1 penalty. (B) Upper and middle images show the vertical ( $\rho_z$ ) and horizontal ( $\rho_y$ ) resistivity vs. offset distance (km) using 1.0 penalty. Lower image in (A) and (B) shows the 2D seismic profile of Ulloa 99 cruise that matches with the location of LAH-2 profile. NO-SE profile. Red lines represent the main faults, Consag and Wagner faults from left to right.**

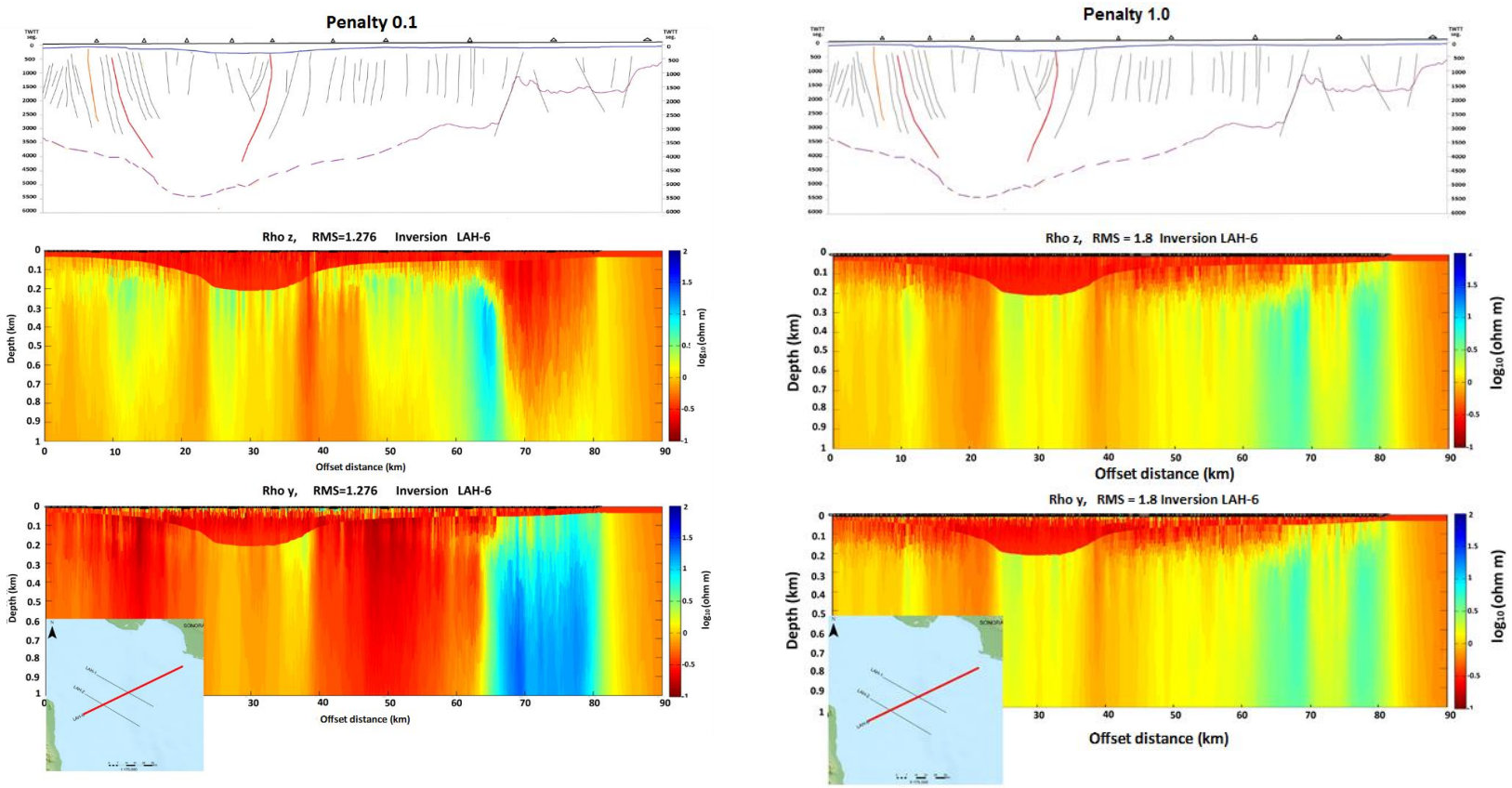


**Figure 33. Comparison between CSEM LAH-6 anisotropic Inversion models using 0.1 and 1.0 anisotropic penalty weight and PEMEX 2D seismic reflection profile. (A) Middle and lower images show the vertical ( $\rho_z$ ) and horizontal ( $\rho_y$ ) resistivity vs. offset distance (km) using 0.1 penalty. (B) Upper and middle images show the vertical ( $\rho_z$ ) and horizontal ( $\rho_y$ ) resistivity vs. offset distance (km) using 1.0 penalty. Upper image in (A) and (B) shows the 2D seismic profile from the PEMEX cruise that matches with the location of LAH-6 profile. SO-NE profile. Red lines represent the main faults, Consag and Wagner faults from left to right. Triangles represent the receivers used for the MT method.**

# Chapter 6. Conclusions

The recently developed surface towing version of the CSEM method was successfully employed over the study area mapping the resistivity contrasts over 1 km of depth. The provided methodology by SIO/UCSD for the processing, forward and inversion modelling was successfully applied in the acquired data, giving encouraging results.

In relation to the general objective, when we compared the results of previous heat flow measurements with the calculated resistivity distributions using the interpolation contours, the high heat flow values, already linked with hydrothermal manifestations, match with low resistivity values, therefore the positive correlation between these variables indicates that the method is effective to find zones of hydrothermal flow.

The method proved to be very effective for mapping shallow areas (< 250 m) identifying low resistivities zones that match with the presence of major faults. Given the structure of the low resistive bodies, it is possible localized hydrothermal manifestations match with the presence of faults identified by previous seismic.

This is the first time the method has been used to locate hydrothermal flow zones in the sea, therefore the fact that results have found at least geologically reasonable models is a good indicator that the method can be adjusted for further studies.

# List of references

Alvarez-Borrego, S., Flores-Báez, B. P., & Galindo-Bect, L. A. (1975). Hidrología del Alto Golfo de California II. Condiciones durante invierno, primavera y verano. Ciencias Marinas, 2(1): 21-36.

Anderson, C. & Mattson, J. (2010). An integrated approach to marine electromagnetic surveying using a towed streamer and source. First Break, 28(5).

Barajas, A. M. (2000). Volcanismo y extensión en la Provincia Extensional del Golfo de California. Boletín de la Sociedad Geológica Mexicana, 53(1): 72-83.

Becker, K., Von Herzen, R. P., Francis, T. J. G., Anderson, R. N., Honnorez, J., Adamson, A. C., ... & Laverne, C. (1982). In situ electrical resistivity and bulk porosity of the oceanic crust Costa Rica Rift. Nature, 300: 594-598.

R. Bertani, Geothermal power generation in the world 2010-2014. Update report, Proceedings World Geothermal Congress 2015, Melbourne, Australia, 19-25 April 2015.

Carrasco-Núñez, G., J. Arzate, J. P. Bernal, J. Carrera, F. Cedillo, P. Dávila-Harris, J. Hernández, S. Hurwitz, J. Lermo, G. Levresse, P. López, V. Manea, G. Norini, E. Santoyo, C. Willcox, (2015). A new geothermal exploration program at Los Humeros volcanic and geothermal field (Eastern Mexican Volcanic Belt). Proceedings World Geothermal Congress 2015, Melbourne, Australia, 19-25 April 2015.

Chave, A. D., & Cox, C. S. (1982). Controlled electromagnetic sources for measuring electrical conductivity beneath the oceans: 1. Forward problem and model study. Journal of Geophysical Research: Solid Earth, 87(B7): 5327-5338.

Constable, S. (2007): Geomagnetic Induction Studies, in Treatise on Geophysics, Volume 5, (2nd. ed.) G. Schubert and M. Kono (ed.) Elsevier: 219-254.

Constable, S. (2010). Ten years of marine CSEM for hydrocarbon exploration. Geophysics, 75(5): 75A67–75A81.

Constable, S. (2013). Review paper: Instrumentation for marine magnetotelluric and controlled source electromagnetic sounding. Geophysical Prospecting, 61(s1): 505-532.

Constable, S. C., Parker, R. L., & Constable, C. G. (1987). Occam's inversion: A practical algorithm for generating smooth models from electromagnetic sounding data. Geophysics, 52(3): 289-300.

Constable, S., & Cox, C. S. (1996). Marine controlled-source electromagnetic sounding 2. The PEGASUS experiment. Journal of Geophysical Research, 101(B3), 5519-5530.

Constable, S. & Weiss, C. J. (2006). Mapping thin resistors and hydrocarbons with marine EM methods: Insights from 1D modeling. Geophysics, 71(2): G43–G51.

Constable, S., Key, K., & Lewis, L. (2009). Mapping offshore sedimentary structure using electromagnetic methods and terrain effects in marine magnetotelluric data. Geophysical Journal International, 176(2): 431-442.

Constable, S., Orange, A., & Key, K. (2015). And the geophysicist replied:"Which model do you want?". Geophysics, 80(3): E197-E212.

Cox, C. S., Constable, S. C., Chave, A. D., & Webb, S. C. (1986). Controlled-source electromagnetic sounding of the oceanic lithosphere.

deGroot Hedlin, C. & Constable, S. (1990). Occam's inversion to generate smooth, two-dimensional models from magnetotelluric data. *Geophysics*, 55(12): 1613–1624.

Eidesmo, T., Ellingsrud, S., MacGregor, L., Constable, S., Sinha, M., Johansen, S., Kong, F., & Westerdahl, H. (2002). Sea bed logging (SBL), a new method for remote and direct identification of hydrocarbon filled layers in deepwater areas. First break, 20(3).

Ellingsrud, S., Eidesmo, T., Johansen, S., Sinha, M., MacGregor, L., & Constable, S. (2002). Remote sensing of hydrocarbon layers by seabed logging (SBL): Results from a cruise offshore Angola. The Leading Edge, 21: 972–982.

Engelmark, F., Mattsson, J., & Farouki, M. T. (2014, September). Reservoir Detection and Delineation Using Towed Streamer Electromagnetics. In Third EAGE International Science and Applications workshop Far East Hydrocarbons 2014.

Filloux, J. H. (1987). Instrumentation and experimental methods for oceanic studies. Geomagnetism, 1: 143-248.

Fofonoff, N. P. (1985). Physical properties of seawater: A new salinity scale and equation of state for seawater. J. geophys. Res, 90(C2): 3332-3342.

Gadallah, M. R., & Fisher, R. (2008). Exploration Geophysics. 150 p. Springer Science & Business Media.

Griffiths, D. J., & Reed College. (1999). Introduction to electrodynamics (Vol. 3). Upper Saddle River, NJ: prentice Hall.

González-Escobar, M., Aguilar-Campos, C., Suárez-Vidal, F., & Martín-Barajas, A. (2009). Geometry of the Wagner basin, upper Gulf of California based on seismic reflections. International Geology Review, 51(2): 133-144.

Gutiérrez-Negrín, L. C., Maya-González, R., & Quijano-León, J. L. (2015). Present situation and perspectives of geothermal in Mexico. In Proceedings, World Geothermal Congress (p. 10).

Key, K. (2009). 1D inversion of multicomponent, multifrequency marine CSEM data: Methodology and synthetic studies for resolving thin resistive layers. Geophysics, 74(2): F9-F20.

Key, K. (2012). Marine electromagnetic studies of seafloor resources and tectonics. Surveys in geophysics, 33(1): 135-167.

Key, K., & Ovall, J. (2011). A parallel goal-oriented adaptive finite element method for 2.5-D electromagnetic modelling. Geophysical Journal International, 186(1): 137-154.

Linfoot, J., Mattsson, J., & Price, D. (2011, January). Case study of a towed streamer EM survey over the Troll field, North Sea. In 2011 SEG Annual Meeting. Society of Exploration Geophysicists.

Lonsdale, P. (1989). Geology and tectonic history of the Gulf of California. The eastern Pacific Ocean and Hawaii: Boulder, Colorado, Geological Society of America, Geology of North America, v. N: 499-521.

Barajas, A. M. (2000). Volcanismo y extensión en la Provincia Extensional del Golfo de California. Boletín de la Sociedad Geológica Mexicana, 53(1): 72-83.

Martín-Barajas, A., González-Escobar, M., Fletcher, J. M., Pacheco, M., Oskin, M., & Dorsey, R. (2013). Thick deltaic sedimentation and detachment faulting delay the onset of continental rupture in the northern Gulf of California: Analysis of seismic reflection profiles. Tectonics, 32(5): 1294-1311.

Maza-Vázquez, A. E. (2015). Estudio de sensibilidad del método electromagnético marino de fuente controlada en el dominio de la frecuencia con datos sintéticos. Tesis de Licenciatura, Universidad Nacional Autónoma de México. 39 p.

Myer, D., Constable, S., & Key, K. (2010). A marine EM survey of the Scarborough gas field, Northwest Shelf of Australia. First Break, 28(5).

Myer, D., Constable, S., & Key, K. (2011). Broad-band waveforms and robust processing for marine CSEM surveys. Geophysical Journal International, 184(2): 689-698.

Myer, D., Constable, S., Key, K., Glinsky, M. E., & Liu, G. (2012). Marine CSEM of the Scarborough gas field, Part 1: Experimental design and data uncertainty. Geophysics, 77(4): E281-E299.

Nix R. K. (2013). The Gulf of California. A physical, geological and biological study. University of Texas, Dallas, 23 p. Available online at: http://www.utdallas.edu/~rnix/MAT-SE_Units/gulf_cal.pdf Downloaded June 30, 2016

Oskin, M., Stock, J., & Martín-Barajas, A. (2001). Rapid localization of Pacific–North America plate motion in the Gulf of California. Geology, 29(5): 459-462.

Pankratov, O. V., & Geraskin, A. I. (2010). On processing of controlled source electromagnetic (CSEM) data. Geologica Acta, 8(1): 31-49.

Perkin, R. G., & Walker, E. R. (1972). Salinity calculations from in situ measurements. Journal of Geophysical Research, 77(33): 6618-6621.

Persaud, P., Stock, J. M., Steckler, M. S., Martín-Barajas, A., Diebold, J. B., González-Fernández, A., & Mountain, G. S. (2003). Active deformation and shallow structure of the Wagner, Consag, and Delfín Basins, northern Gulf of California, Mexico. Journal of Geophysical Research: Solid Earth, 108(B7).

Prol-Ledesma, R. M., Torres-Vera, M. A., Rodolfo-Metalpa, R., Angeles, C., Deveze, C. H. L., Villanueva-Estrada, R. E., ... & Robinson, C. (2013). High heat flow and ocean acidification at a nascent rift in the northern Gulf of California. Nature communications, (4), 1388.

Rhodes, M. (2008). Underwater electromagnetic propagation. Re-evaluating wireless capabilities. Retrieved from http://www.hydro-international.com/content/article/ underwater-electromagnetic-propagation. Accessed: 2016-06-18.

Sanchez-Zamora, O., Doguin, P., Couch, R. W., & Ness, G. E. (1991). Magnetic anomalies of the northern Gulf of California: Structural and thermal interpretations. The Gulf and Peninsular Provinces of the Californias, 47: 377-401.

Shantsev, D. V., Roth, F., & Ramsfjell, H. (2012,). Surface towing versus deep towing in marine CSEM. In 2012 SEG Annual Meeting. Society of Exploration Geophysicists.

Sharma, P. V. (1985). Geophysical methods in geology. (pp. 261-263). Elsevier.

Stock, J. M., & Hodges, K. V. (1989). Pre-Pliocene extension around the Gulf of California and the transfer of Baja California to the Pacific Plate. Tectonics, 8(1): 99-115.

Tveit, S. (2014). Inversion of CSEM Data for Subsurface Structure Identification and Numerical Assessment of the Upstream Mobility Scheme, Doctoral thesis, University of Bergen. 36 p.

Vázquez-Figueroa, V., Canet, C., Prol-Ledesma, R. M., Sánchez, A., Dando, P., Camprubí, A.,... & Hiriart Le Bert, G. (2009). Batimetría y características hidrográficas (Mayo, 2007) en las Cuencas de Consag y Wagner, Norte del Golfo de California, México. Boletín de la Sociedad Geológica Mexicana, 61(1): 119-127.

Webb, S. C., Constable, S. C., Cox, C. S., & Deaton, T. K. (1985). A seafloor electric field instrument. Journal of Geomagnetism and Geoelectricity, 37(12): 1115-1129.

Weitemeyer, K. (2008). Marine Electromagnetic Methods for Gas Hydrate Characteriza- tion. PhD. Thesis, University of California, San Diego: 13-15.

Weitemeyer, K. A., Constable, S. C., Key, K. W., & Behrens, J. P. (2006). First results from a marine controlled-source electromagnetic survey to detect gas hydrates offshore Oregon. Geophysical Research Letters, 33(3).

Weitemeyer, K. A., Constable, S., & Trehu, A. M. (2011). A marine electromagnetic survey to detect gas hydrate at Hydrate Ridge, Oregon. Geophysical Journal International, 187(1): 45-62.

Zhdanov, M. S. (2015). Inverse theory and applications in geophysics (Vol. 36). Elsevier.

# APPENDIX A

# NOMENCLATURE

| PARAMETERS | | UNITS |
|---|---|---|
| σ | electrical conductivity | S/m |
| ρ | electrical resistivity | $\Omega m$ |
| **B** | Magnetic induction | Tesla |
| **D** | Dielectric displacement | $C/m^2$ |
| **H** | Intensity of magnetic field | A/m |
| **J** | current density | $A/m^2$ |
| *q* | charge density | $C/m^3$ |
| ε | electrical permittivity | F/m |
| $\mu$ | magnetic permeability | $N/A^2$ |
| f | frequency | Hz |
| *I* | Current | A |
| SDM | Source Dipole Moment | Am |
| $s^2$ | Variance | $V/Am^2$ |
| l | Length | m |
| T | temperature | °C |
| NF | Noise Floor | $V/Am^2$ |
| V | Voltaje | Volts |
| $E_y$ | amplitude measured electric field | $V/Am^2$ |
| *t* | Time | s |
| | Heat flow | $mWm^{-2}$ |

# APPENDIX B

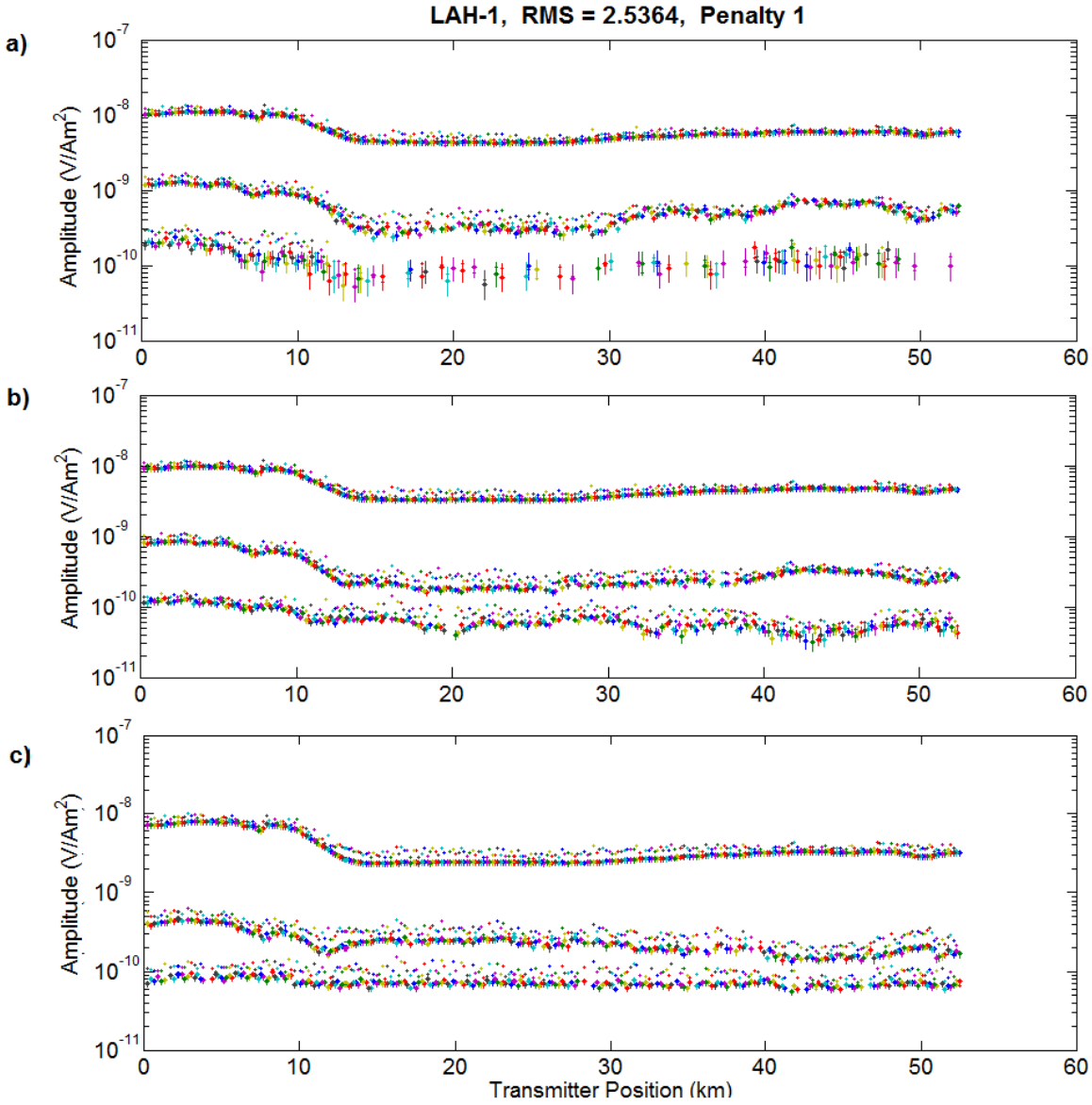


**Figure 34: Model responses (dots) and measured data in the profile LAH-1 (dots with error bars) for the three closest instruments for the frequencies 1.5, 3.5 and 6.5 Hz. (a) plot of the model responses and measured data by the three closest receivers for the frequency of 1.5 Hz, (b) 3.5 Hz and (c) 6.5 Hz. The higher amplitudes are measured by the closest instrument, while the smallest ones by the farthest one. Anisotropic Penalty = 1.0.**

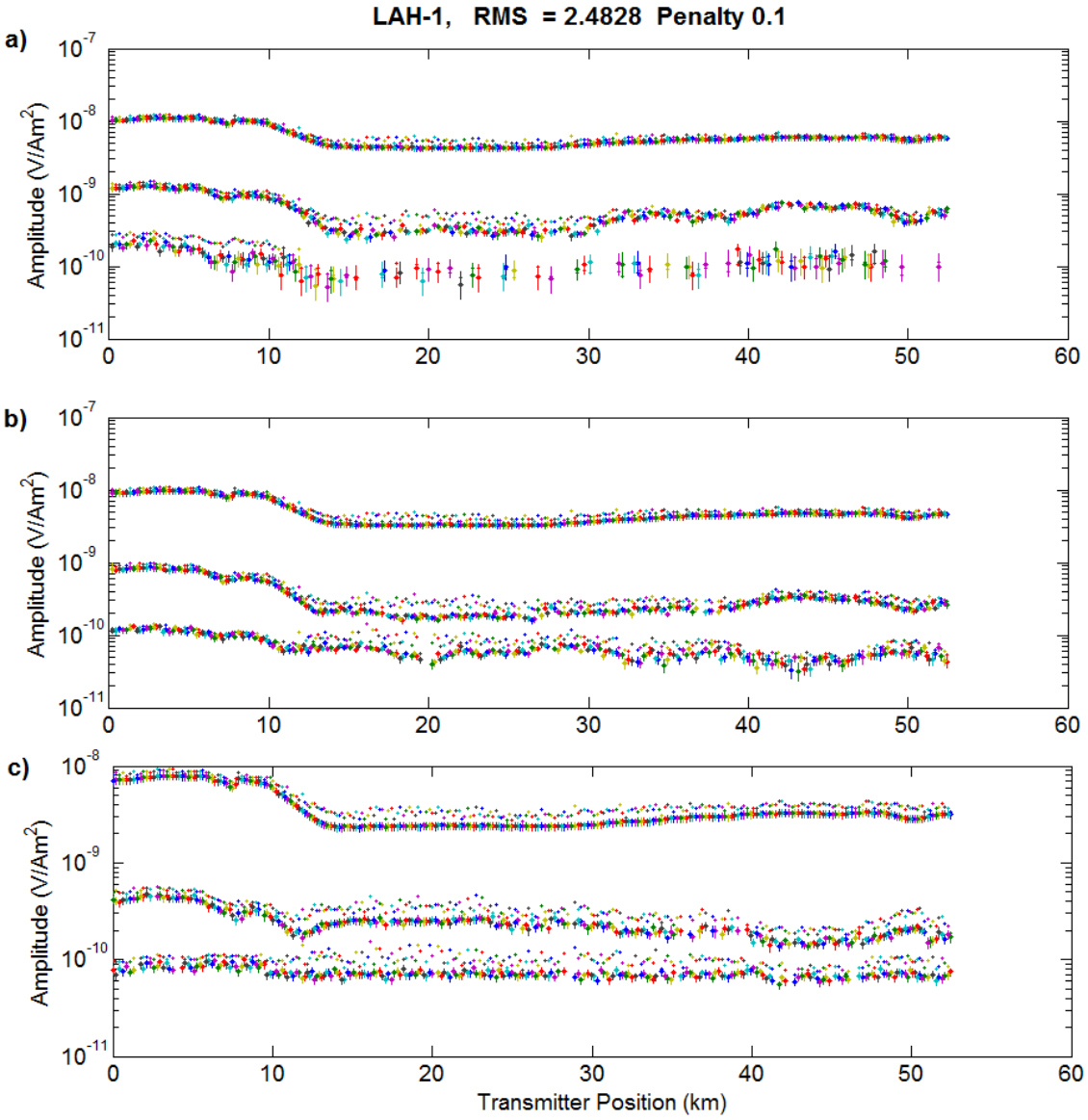


**Figure 35: Model responses (dots) and measured data in the profile LAH-1 (dots with error bars) for the three closest instruments for the frequencies 1.5, 3.5 and 6.5 Hz. (a) plot of the model responses and measured data by the three closest receivers for the frequency of 1.5 Hz, (b) 3.5 Hz and (c) 6.5 Hz. The higher amplitudes are measured by the closest instrument, while the smallest ones by the farthest one. Anisotropic Penalty = 0.1.**

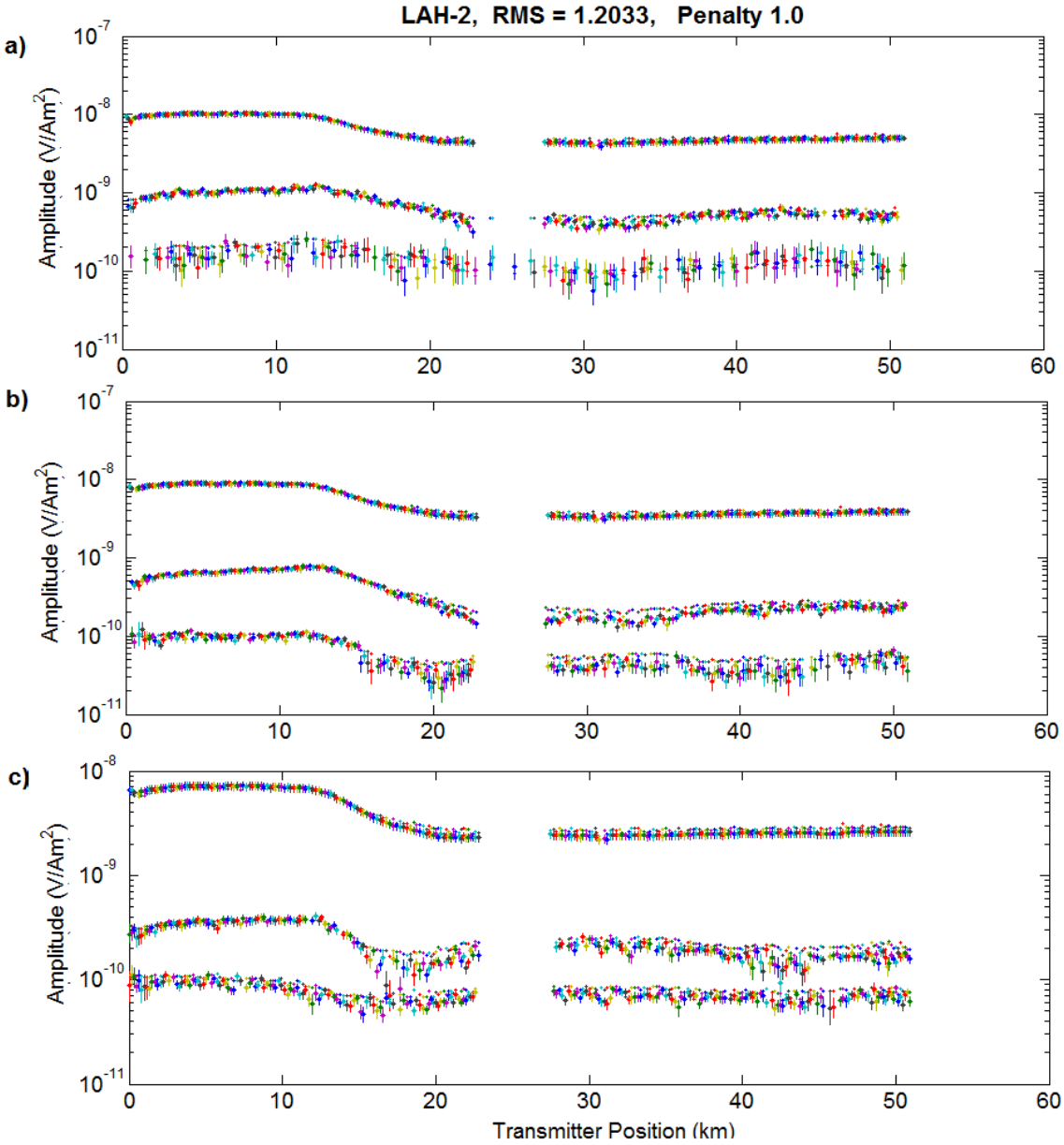


**Figure 36: Model responses (dots) and measured data in the profile LAH-2 (dots with error bars) for the three closest instruments for the frequencies 1.5, 3.5 and 6.5 Hz. (a) plot of the model responses and measured data by the three closest receivers for the frequency of 1.5 Hz, (b) 3.5 Hz and (c) 6.5 Hz. The higher amplitudes are measured by the closest instrument, while the smallest ones by the farthest one. Anisotropic Penalty = 1.0.**

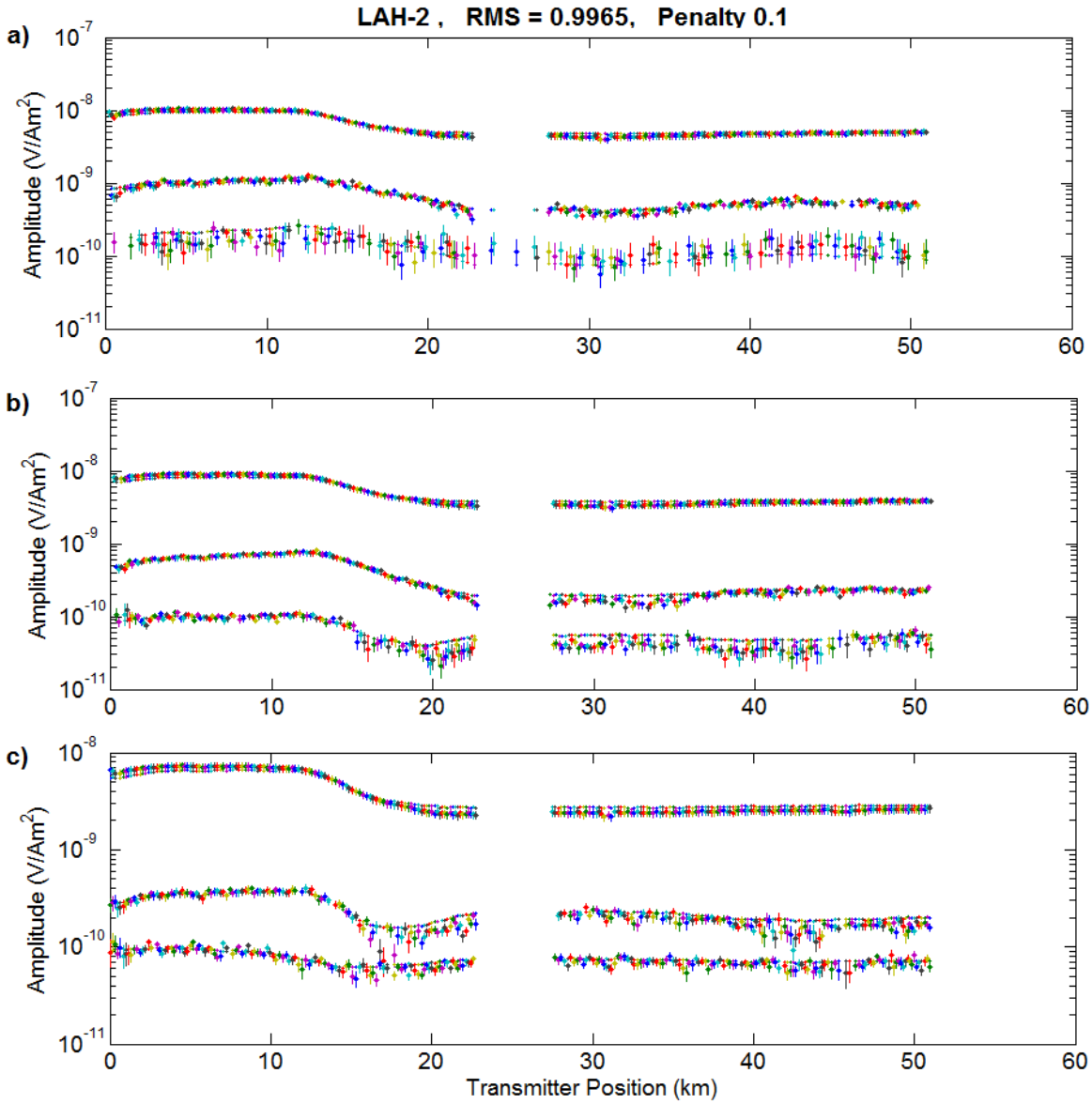


**Figure 37: Model responses (dots) and measured data in the profile LAH-2 (dots with error bars) for the three closest instruments for the frequencies 1.5, 3.5 and 6.5 Hz. (a) plot of the model responses and measured data by the three closest receivers for the frequency of 1.5 Hz, (b) 3.5 Hz and (c) 6.5 Hz. The higher amplitudes are measured by the closest instrument, while the smallest ones by the farthest one. Anisotropic Penalty = 0.1.**

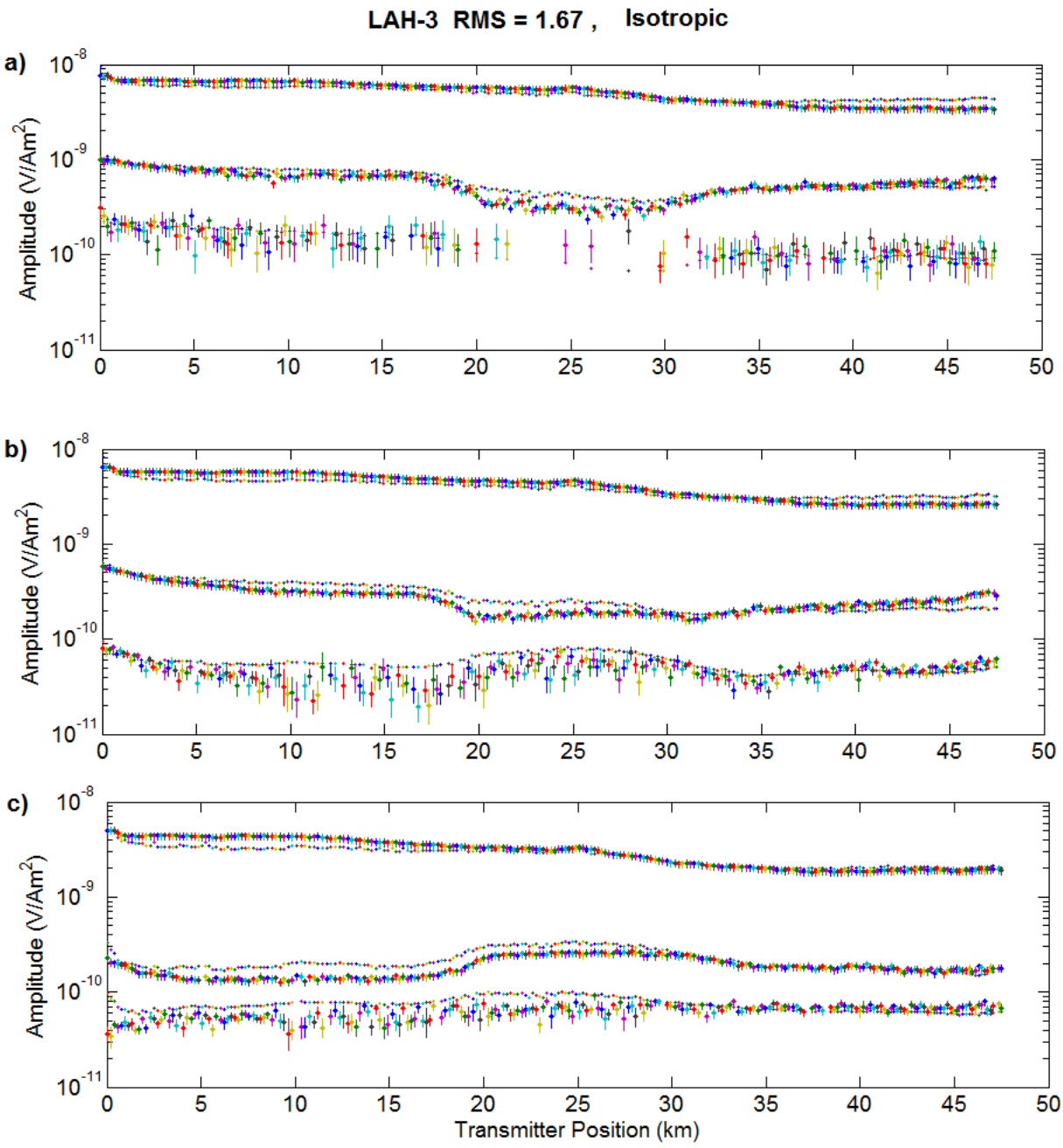


**Figure 38: Model responses (dots) and measured data in the profile LAH-3 (dots with error bars) for the three closest instruments for the frequencies 1.5, 3.5 and 6.5 Hz. (a) plot of the model responses and measured data by the three closest receivers for the frequency of 1.5 Hz, (b) 3.5 Hz and (c) 6.5 Hz. The higher amplitudes are measured by the closest instrument, while the smallest ones by the farthest one. Isotropic model.**

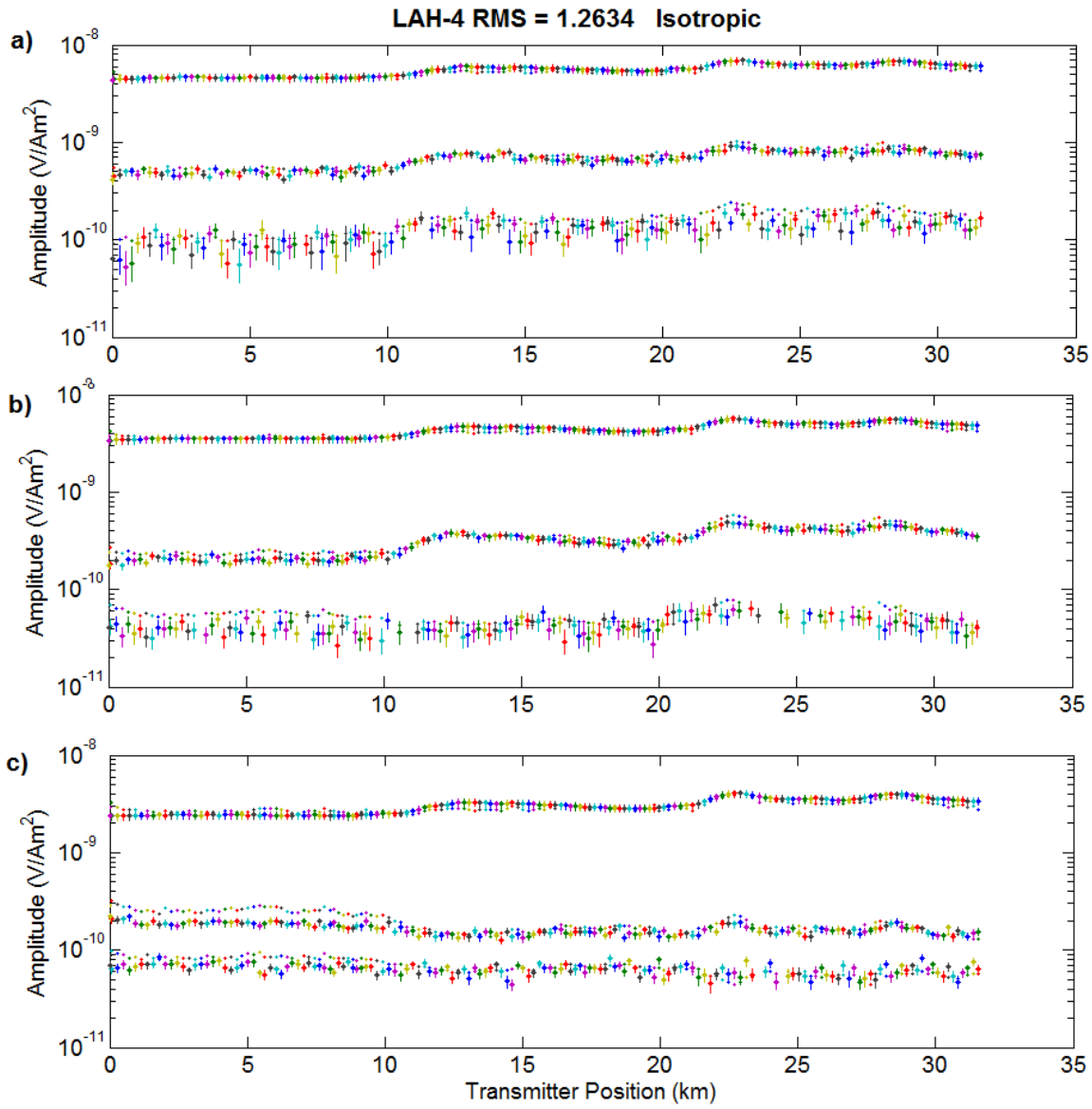


**Figure 39: Model responses (dots) and measured data in the profile LAH-4 (dots with error bars) for the three closest instruments for the frequencies 1.5, 3.5 and 6.5 Hz. (a) plot of the model responses and measured data by the three closest receivers for the frequency of 1.5 Hz, (b) 3.5 Hz and (c) 6.5 Hz. The higher amplitudes are measured by the closest instrument, while the smallest ones by the farthest one. Isotropic model.**

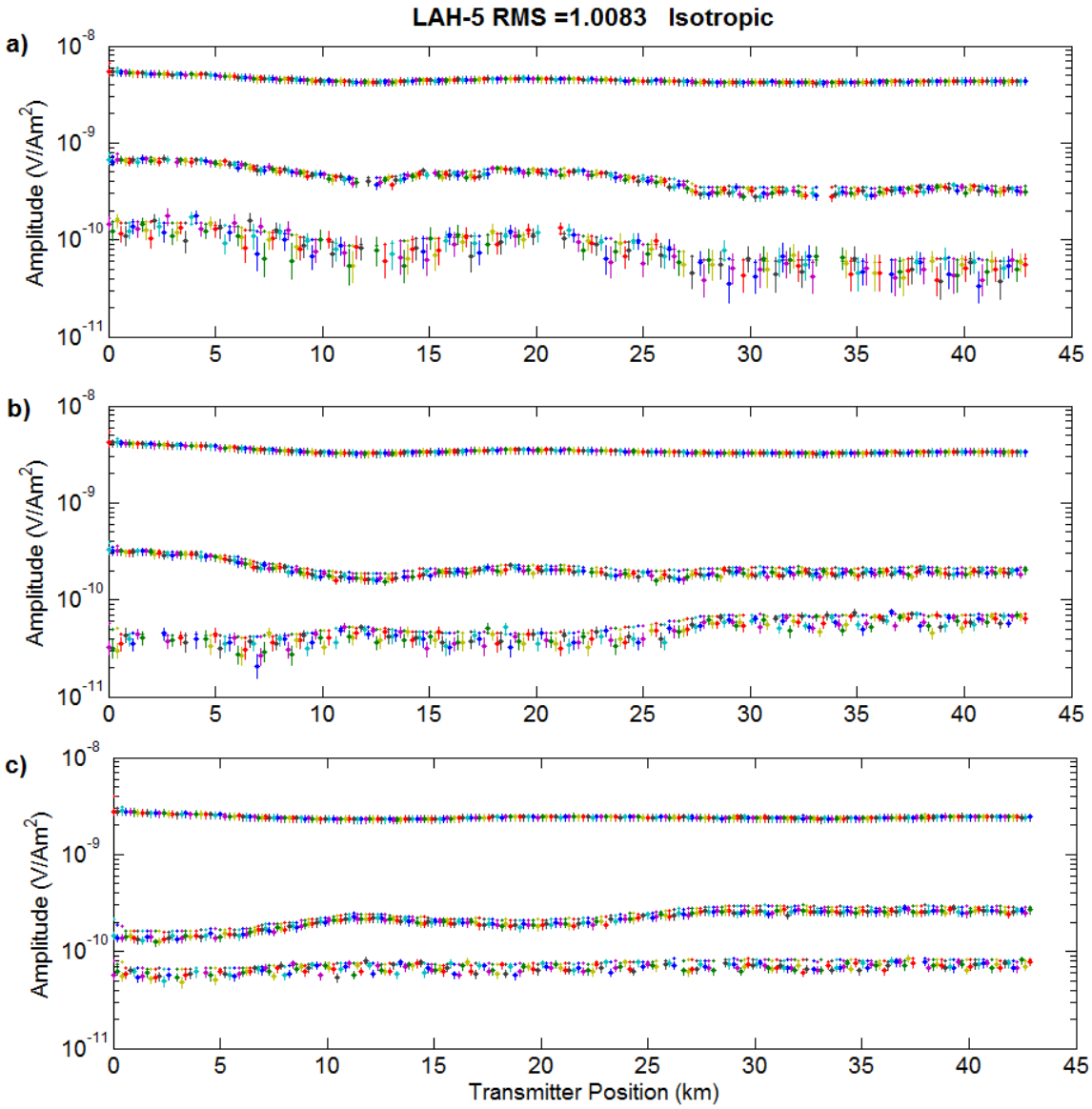


**Figure 40: Model responses (dots) and measured data in the profile LAH-5 (dots with error bars) for the three closest instruments for the frequencies 1.5, 3.5 and 6.5 Hz. (a) plot of the model responses and measured data by the three closest receivers for the frequency of 1.5 Hz, (b) 3.5 Hz and (c) 6.5 Hz. The higher amplitudes are measured by the closest instrument, while the smallest ones by the farthest one. Isotropic model.**

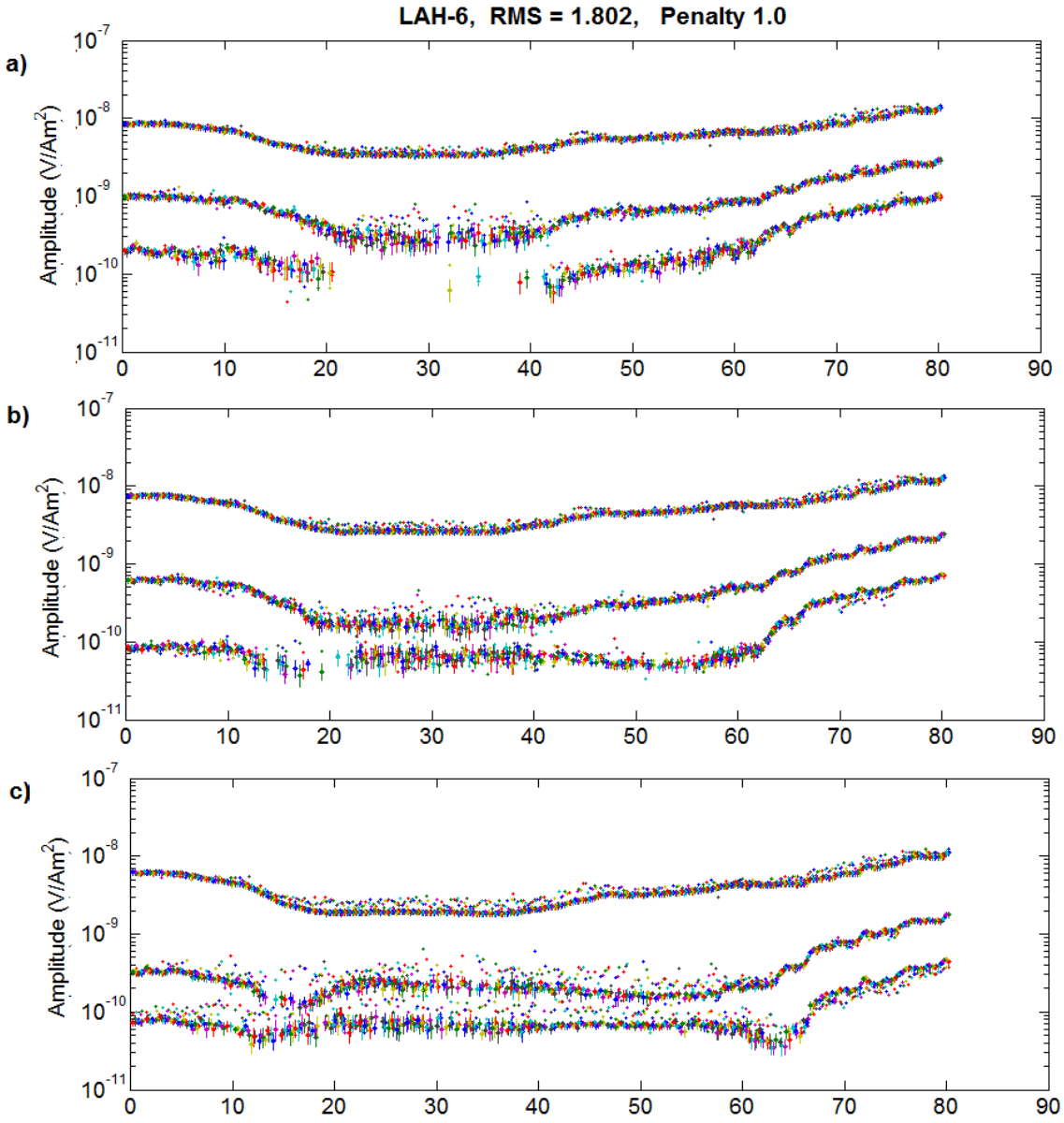


**Figure 41: Model responses (dots) and measured data in the profile LAH-6 (dots with error bars) for the three closest instruments for the frequencies 1.5, 3.5 and 6.5 Hz. (a) plot of the model responses and measured data by the three closest receivers for the frequency of 1.5 Hz, (b) 3.5 Hz and (c) 6.5 Hz. The higher amplitudes are measured by the closest instrument, while the smallest ones by the farthest one. Anisotropic Penalty = 1.0.**

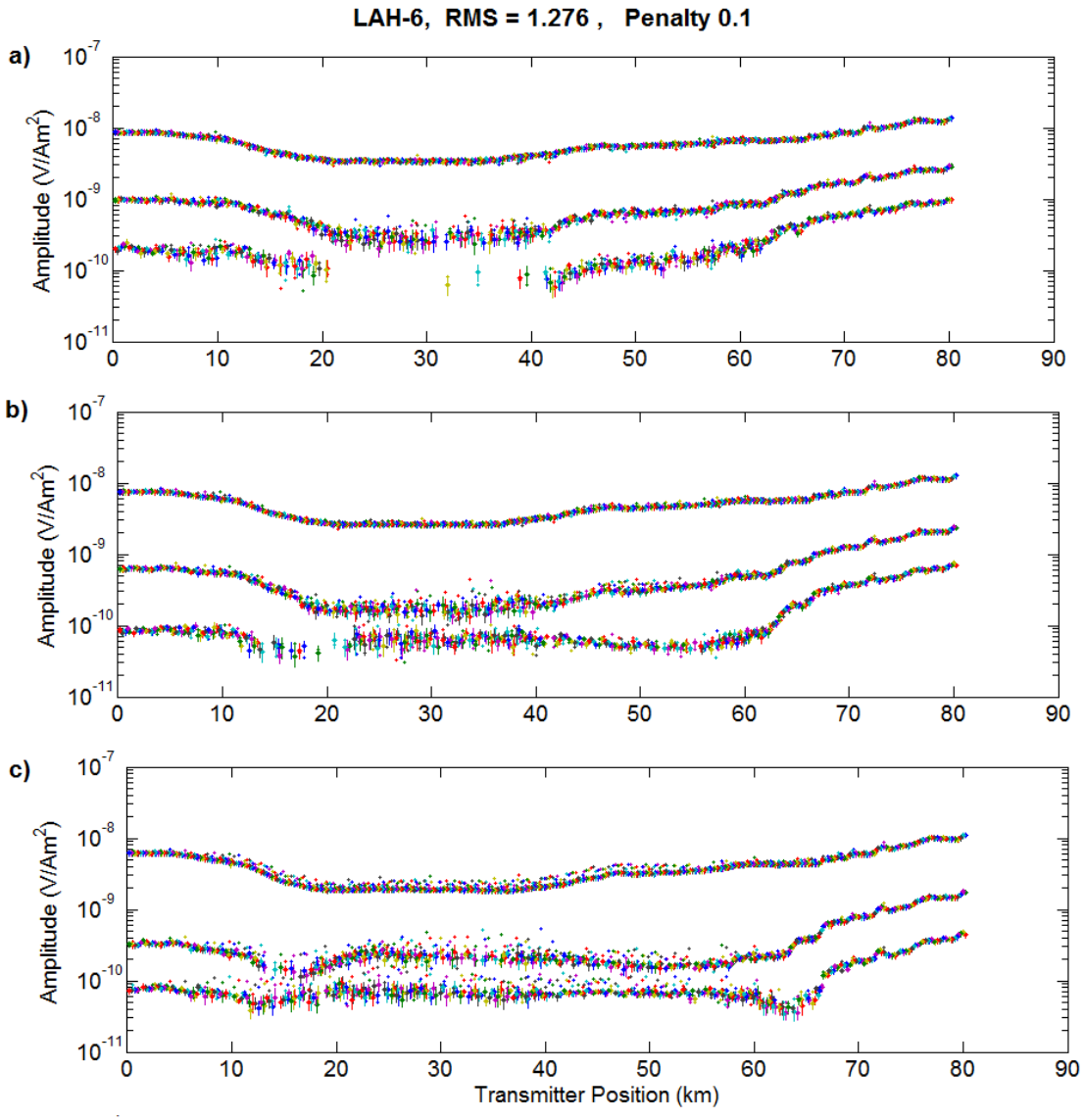


**Figure 42: Model responses (dots) and measured data in the profile LAH-6 (dots with error bars) for the three closest instruments for the frequencies 1.5, 3.5 and 6.5 Hz. (a) plot of the model responses and measured data by the three closest receivers for the frequency of 1.5 Hz, (b) 3.5 Hz and (c) 6.5 Hz. The higher amplitudes are measured by the closest instrument, while the smallest ones by the farthest one. Anisotropic Penalty = 0.1.**

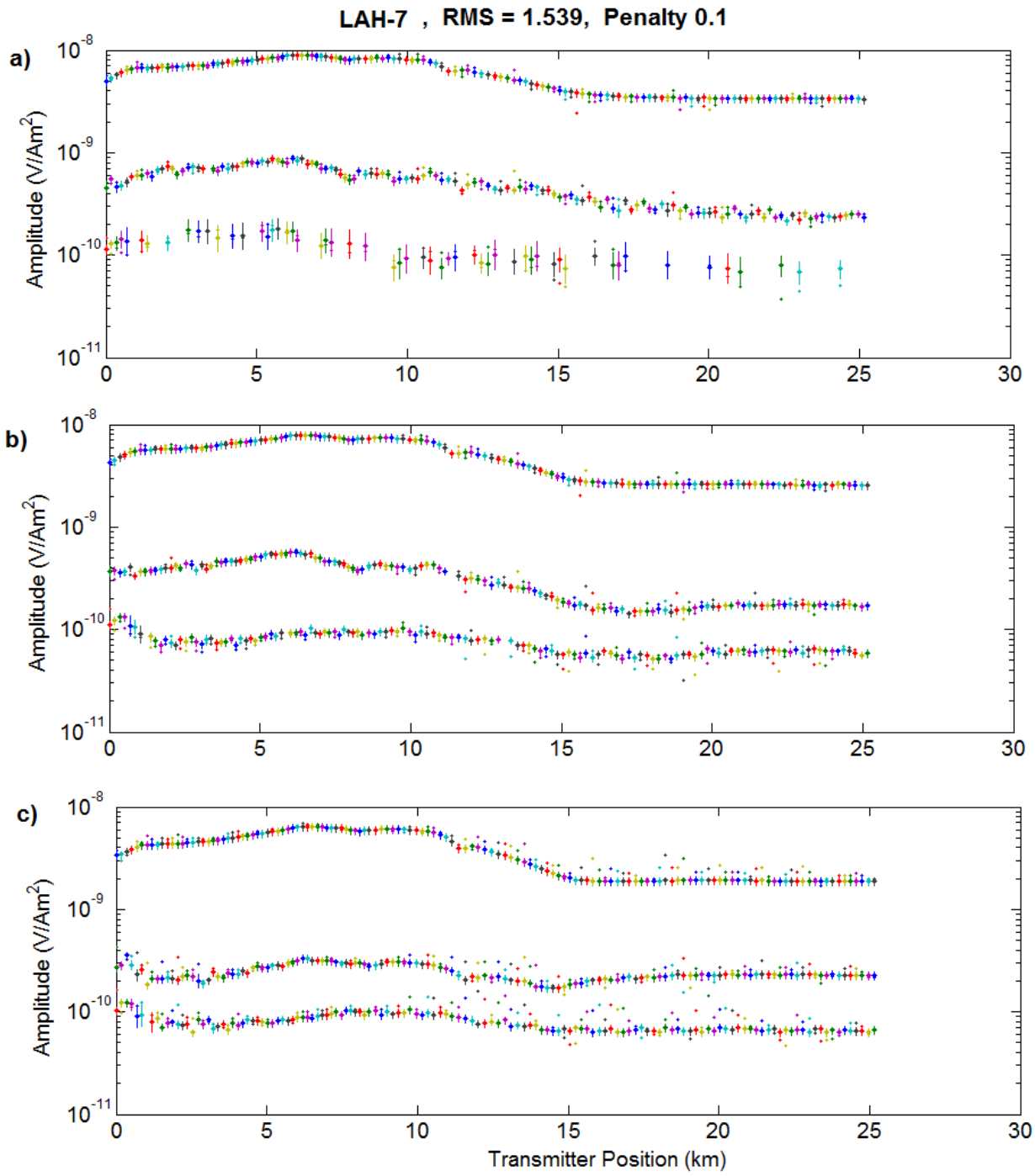


**Figure 43: Model responses (dots) and measured data in the profile LAH-7 (dots with error bars) for the three closest instruments for the frequencies 1.5, 3.5 and 6.5 Hz. (a) plot of the model responses and measured data by the three closest receivers for the frequency of 1.5 Hz, (b) 3.5 Hz and (c) 6.5 Hz. The higher amplitudes are measured by the closest instrument, while the smallest ones by the farthest one. Anisotropic Penalty = 0.1.**

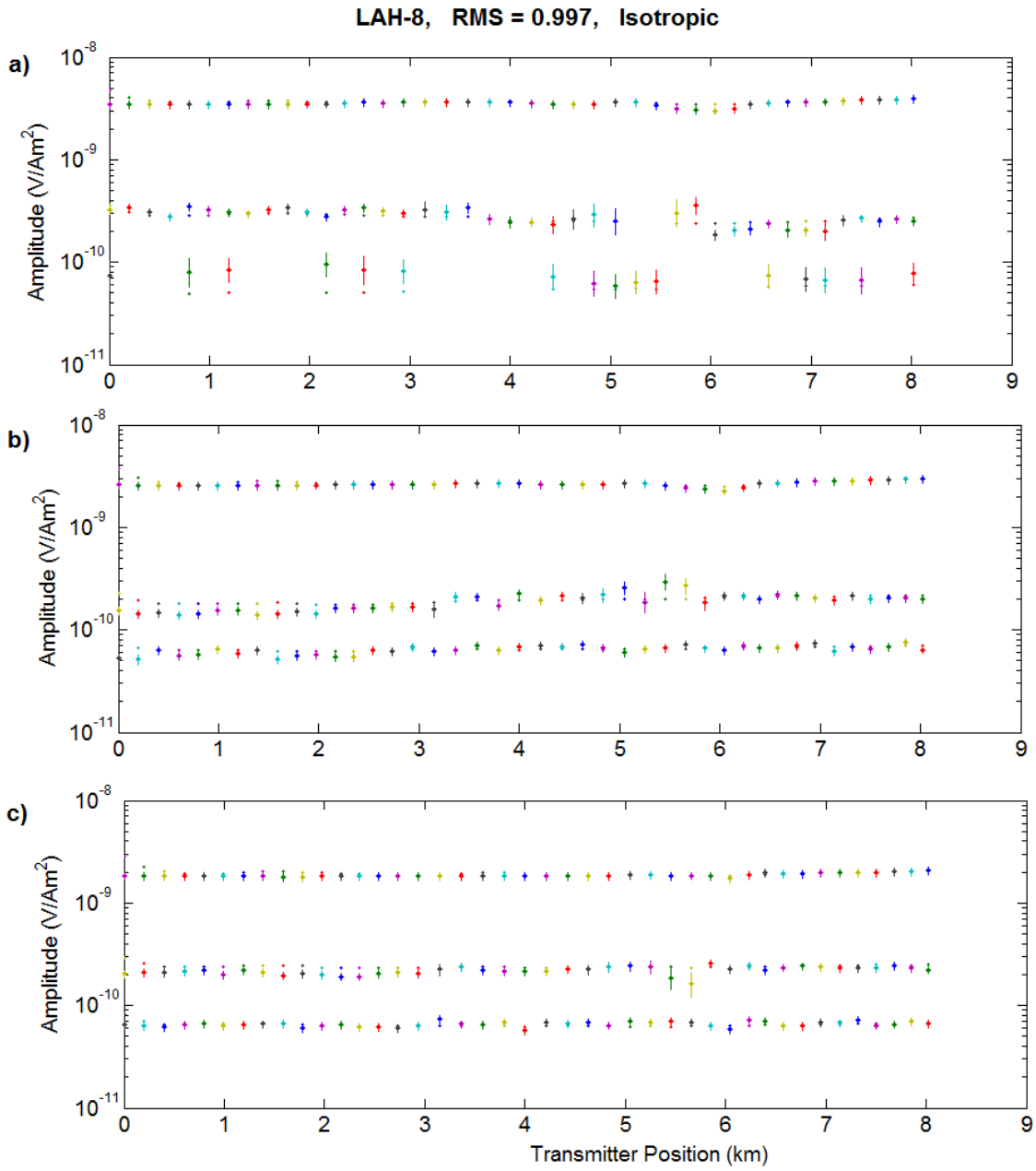


**Figure 44: Model responses (dots) and measured data in the profile LAH-8 (dots with error bars) for the three closest instruments for the frequencies 1.5, 3.5 and 6.5 Hz. (a) plot of the model responses and measured data by the three closest receivers for the frequency of 1.5 Hz, (b) 3.5 Hz and (c) 6.5 Hz. The higher amplitudes are measured by the closest instrument, while the smallest ones by the farthest one. Isotropic model.**

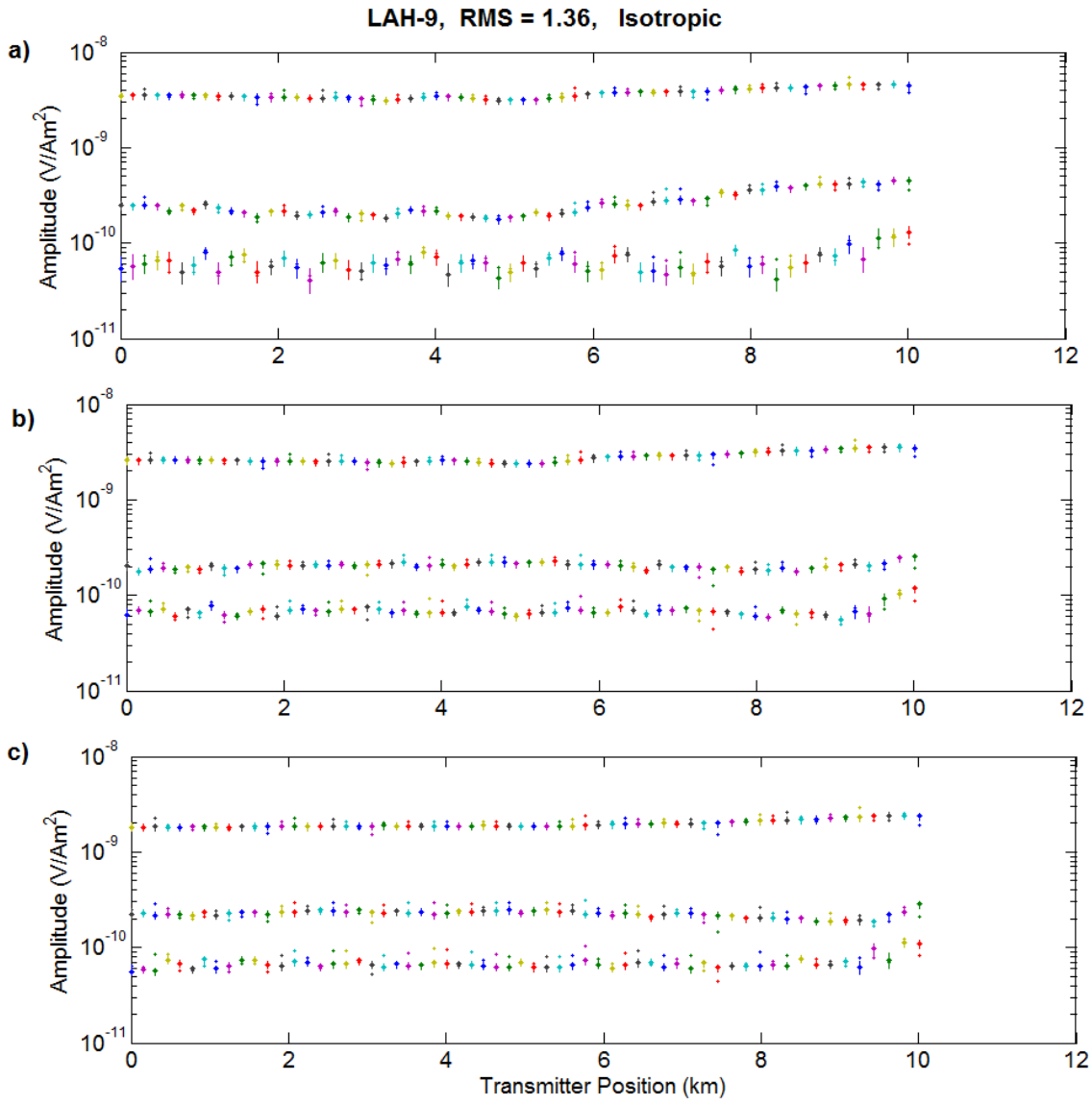


**Figure 45: Model responses (dots) and measured data in the profile LAH-9 (dots with error bars) for the three closest instruments for the frequencies 1.5, 3.5 and 6.5 Hz. (a) plot of the model responses and measured data by the three closest receivers for the frequency of 1.5 Hz, (b) 3.5 Hz and (c) 6.5 Hz. The higher amplitudes are measured by the closest instrument, while the smallest ones by the farthest one. Isotropic model.**